SURFACE AND INTERFACE STUDIES ON MAGNETRON SPUTTERED POLYCRYSTALLINE MOLYBDENUM THIN FILMS

By

Ch. Kishan Singh

Enrolment No: PHYS02200804001

INDIRA GANDHI CENTRE FOR ATOMIC RESEARCH

KALPAKKAM-603102

INDIA

A thesis submitted to the

Board of Studies in Physical Sciences

In partial fulfilment of requirements for the Degree of

DOCTOR OF PHILOSOPHY

of

HOMI BHABHA NATIONAL INSTITUTE

August, 2014

Homi Bhabha National Institute

Recommendations of the Viva Voce Committee

As members of the Viva Voce Board, we certify that we have read the dissertation prepared by **Ch. Kishan Singh** entitled "**Surface and interface studies on magnetron sputtered polycrystalline molybdenum thin films**" and recommend that it may be accepted as fulfilling the dissertation requirement for the Degree of Doctor of Philosophy.

Chairman - Dr. Sitaram Dash **Date:**

Convener – Dr. A.K. Tyagi **Date:**

Member – Dr. Saroja Saibaba **Date:**

Member – Dr. R. Ramaseshan **Date:**

Technical advisor – N. Murali **Date:**

External Examiner – **Date:**

Final approval and acceptance of this dissertation is contingent upon the candidate's submission of the final copies of the dissertation to HBNI.

Date:

Place:

CERTIFICATE

I hereby certify that I have read this dissertation prepared under my direction and recommend that it may be accepted as fulfilling the dissertation requirement.

Date: **(A.K.Tyagi)**

Place:

STATEMENT BY AUTHOR

This dissertation has been submitted in partial fulfilment of requirements for an advanced degree at Homi Bhabha National Institute (HBNI) and is deposited in the Library to be made available to borrowers under the rules of the HBNI.

Brief quotations from this dissertation are allowable without special permission, provided that accurate acknowledgment of source is made. Requests for permission for extended quotation from or reproduction of this manuscript in whole or in part may be granted by the Competent Authority of HBNI when in his or her judgement the proposed use of the material is in the interests of scholarship. In all other instances, however, permission must be obtained from the author.

(Ch. Kishan Singh)

Kalpakkam

August 2014

DECLARATION

I, hereby declare that the investigation presented in the thesis entitled “Surface and interface studies on magnetron sputtered polycrystalline molybdenum thin films” has been carried out by me. The work is original and has not been submitted earlier as a whole or in part for a degree/ diploma at this or any other Institution/ University.

(Ch. Kishan Singh)

Kalpakkam

August 2014

List of Publications arising from the thesis

Journals

Published:

1. “Phase formation and impurity effects in Ar^+ ion irradiated Mo/Si thin film bilayer system”, **Ch. Kishan Singh**,* S. Ilango, S. Dash and A. K. Tyagi, ***Surf. Interface Anal.***, **2013**, *45*, 895-900.
2. “On the evolution of residual stress at different substrate temperatures in sputter deposited polycrystalline Mo thin films by x-ray diffraction”, **Ch. Kishan Singh**,* S. Ilango, S.R. Polaki, S. Dash and A. K. Tyagi, ***Mater. Res. Express,*** **2014,** *1*, 036401.

Communicated:

3. “The effect of micro-structural features on secondary ion mass spectrometry depth profiling of a polycrystalline-Mo (metal)/silicon interface”, **Ch. Kishan Singh**,* S. Ilango, S. Dash and A. K. Tyagi**.**

Conferences Proceedings

1. “Study of local in-homogeneity in ion beam mixing using SIMS ion imaging techniques”, **Ch. Kishan Singh,*** S. Ilango, S. Dash and A.K. Tyagi, ***AIP Conf. Proc.,*** **2012,** *1447*, 681-682.

2. Effect of substrate temperatures on the microstructure of RF magnetron sputtered Mo thin films, **Ch. Kishan Singh,** invited talk, ***3rd International Conference on Laser and Plasma Application in Materials Science, 2015***

Dedicated to my loving daughter

ACKNOWLEDGEMENT

I am glad that I have managed to complete my thesis, and I thank the almighty for bestowing upon me the strength to take the thesis into its logical conclusion. In what follows, I am obliged to acknowledge the encouragement and the tremendous help offer to me by my close associates in their own varying capacities, without which I feel the thesis would not have seen the light of day.

I would like to thank my research supervisor, Dr. A.K. Tyagi for his constant guidance, support and encouragement throughout the period of the thesis. I am also thankful for his critical review of the thesis manuscript and the valuable feedback.

I would also like to thank Dr. Sitaram Dash for his continue association with me in various capacities that both as section head as well as the chairman of my doctoral committee. His guidance, review of drafts and constructive criticism is highly acknowledged.

I thank Dr. S. Ilango for being constantly there in times of need. He has been instrumental in reaching out or should I say bridging to people for experimental facilities that were not available in our section. Further thank him his help in experiments, review of both manuscripts for journal as well as the thesis and for the constructive criticism on the same.

I also thank other members of my doctoral committee Dr. R. Ramaseshan, Dr. Saroja Saibaba and my technical advisor Mr. N. Murali for the constructive criticism and the much needed recommendation for extension of my Ph.D tenure for the period August 2013 to August 2014 that had made all the difference, finally leading to the completion of the present thesis.

I would be guilty if I don't thank those many wonderful people whom I approach for various experiments and who extended their facility or equivalently the instrument time wholeheartedly to the best of their capacities. Though I should be thanking them individually, please accept my apology beforehand for just writing the name, but however, this in no way undermines or belittles the great help your experiment has been to the completion of this thesis.

And so I am sincerely thankful to Dr. P. Magudapathy, Dr. K. Ganesan, Dr. R. Ravindran, Dr. S. Dhara, Dr. S. Kalavathi, Dr. S. Rajagopalan, Mr. Shyamala Rao Polaki, Dr. R. Pandian, Dr. K. Saravana, Dr. M. Kamruddin, Mr. A.K. Balamurugan, Mr. Kishore Kumar Madapu and Mrs. D. T. Sunitha.

I also thank my family members, friends and my better half for being a constant source of inspiration throughout this phase of my life. It is through their motivation and association that I have come to realized that there are no 'perfectionist' in this world, we make dos we pragmatism!

Finally I thank everyone who is reading this.

------- Ch. Kishan Singh

CONTENTS

CHAPTER *3* **PHASE FORMATION IN THIN FILMS: A STUDY ON Ar$^+$ ION BEAM IRRADIATED Mo/Si THIN FILM**

CHAPTER *4* RESIDUAL STRESS IN Mo THIN FILMS USING X-RAY DIFFRACTION

CHAPTER *5* EFFECT OF MICROSTRUCTURE ON SECONDARY ION MASS SPECTROMETRY DEPTH PROFILING OF -Mo/Si INTERFACE

CHAPTER 6 SUMMARY AND SCOPE FOR FUTURE WORK

SYNOPSIS

Polycrystalline Mo thin films have a vast number of technological applications which include gate electrode, back contact layer in solar cell industry and as well as protective coating [1-2]. While the disilicide phase of Mo is technologically important for VLSI and interconnects [3-5], chemically and thermally stable Mo/Si multilayers have technological interest for used in X-ray mirrors and UV lithography [6-8]. So, there is a clear need for studies to improve understanding on interfacial characteristics of Mo/Si system. This thesis investigates certain aspects that influence micro-structural, phase and interfacial characteristics of polycrystalline Mo thin films deposited on Si substrates. Issues related to interfacial characterization and residual stress that affects the film-and-substrate relation is also investigated. The formation of technologically important molybdenum dilisicide phase upon Ar^+ ion irradiation and subsequent flash annealing are investigated. The importance of this study is that while many reports exist on formation of disilicide in Mo/Si system using dopants ions like As, P through a process called Implantation Through Metal (ITM) method [5, 9], understanding and literature on phase formation in Mo/Si system using inert Ar^+ ion is rather sparse. The investigation reveals that as-irradiated specimen exhibits only substantial mixing devoid of formation of any disilicide bearing phase. Disilicide phase forms only upon flash annealing at 800 °C for 60 seconds duration, however, dose dependent polymorphic phases comprising both metastable h-$MoSi_2$ and thermodynamically stable t-$MoSi_2$ were found to nucleate upon annealing. The h-$MoSi_2$ persists for all specimens; however t-$MoSi_2$ phase appears only for specimen irradiated to higher dose indicating phase retardation. This phase retardation was attributed to the presence of Ar impurities.

A short investigation on the local homogeneity of Ar^+ ion beam mixed Mo/Si thin film irradiated to a dose of 2 x 10^{17} ions/cm^2 at an energy of 110 keV was also performed using secondary ion imaging techniques with SIMS. Significant local variation in decay lengths were observed for different local region of interest (RoI).

Further, issues pertaining to interfacial characterization of Mo/Si system upon compositional depth profiling with dynamic Secondary Ion Mass Spectrometry (SIMS) were investigated. While Mo/Si was presented as a case study, the study concerned characterization of polycrystalline material interfaces. This is because SIMS depth profile analysis of polycrystalline materials is often associated with ambiguous artifacts. Degradation in depth resolution and distortion in profile may arise due to several parameters like sputter induced change in surface composition and surface topography, surface roughness, matrix effect and radiation induced effects [10-12]. Hence, a careful data analysis is essential before interpreting a measured depth profile. Mo/Si thin films with varying Mo microstructures were characterized using SIMS depth profiling. The broadenings in the Mo profiles at the interfaces were investigated. Complementary techniques were used to investigate the aspect of diffusion and phase formation and the ensuing results are discussed. The broadening was correlated to roughness induced on the SIMS crater surface by the non-uniform sputtering of the differently oriented polycrystalline grains of Mo films. The effect of surface roughness on the resulting interfacial roughness is also discussed.

Further, as residual stress is inevitable in vacuum deposited thin films and it influences the film-to-substrate relation. It can cause deleterious effects like cracking of the film in case of tensile stress ‘or’ buckling in case of a compressive stress [^{1}3]. Hence, evolution of residual stress in Mo thin films sputter deposited over Si as a function of substrate temperature was investigated. The investigation emphasized on the use of asymmetric X-ray diffraction as a technique to measure residual stress in thin films [14-17]. The analyses were performed using a modified $\sin^2\psi$ with a single *hkl* as well as multi *hkl* peak shift approaches. The observed evolution of residual stress exhibits a reversal in the state of stress as a function of substrate temperature (T_s). It was observed to be compressive at low deposition temperatures and becomes tensile at higher deposition temperatures. This evolutionary trend is described in details. The thermal and intrinsic components were discerned and a mechanism different from atomic peening is mooted as the cause for manifestation of compressive stress at low deposition temperature.

The thesis is organized into six chapters. Chapters 1 and 2 pertain to introduction and experimental techniques. Chapters 3, 4 and 5 bring out the important experimental results and attempts to furnish physical explanations for the same. Chapter 6 gives a brief summary and scope for future work. The salient features of the contents of each chapter are briefly presented below.

Chapter 1: A brief introduction to thin films: surface and interface phenomenon

This chapter briefly discusses features that make thin films possess quite remarkably different characteristics from their bulk counterpart. The importance of microstructure, surfaces and interfaces in thin films are highlighted. The classification, some commonly used deposition techniques and different modes of growth are also discussed. In addition, there is a brief description on commonly used surface and interface analyses techniques. It is followed by motivation for pursuing this work and literature survey pertaining to various studies on Mo/Si system.

Chapter 2: Experimental technique

This chapter describes details of all the experimental techniques that were employed to perform research works whose subsequent results, analysis and interpretation constitute the present thesis. It includes radio frequency magnetron sputtering as the method for sample preparation. The working principle is briefly discussed. The experimental conditions used for various polycrystalline molybdenum thin films preparation are also discussed. The working principles and the methodologies used for conditioning treatment and characterization are also discussed. The conditioning treatment includes ion beam irradiation experiments of 43 nm thick Mo/Si thin films with Ar^+ ion beam to induce ion mixing at the interface and rapid flashed annealing of the sample at 800 °C in vacuum. The characterization techniques include secondary ion mass spectrometry, Rutherford backscattering spectrometry, grazing incidence X-ray diffraction, atomic force microscopy, Raman spectrometry, scanning electron microscopy and stylus based contact surface profiler.

Chapter 3: Phase formation in thin films: A study on Ar^+ ion beam irradiated Mo/Si thin film

This chapter deals with the phenomenon of phase formation in Mo/Si bilayer thin films upon Ar^+ ion beam irradiation and subsequent flash annealing. It describes details of deposition of Mo films on Si and irradiation of the system with Ar^+ ions at doses ranging from 7×10^{15} cm^{-2} to 2×10^{17} cm^{-2}. The thickness of Mo film (43 nm) and energy of Ar^+ ions (110 keV) were predetermined using TRIM code for efficient mixing across the interface. The interface mixing characteristics were investigated using SIMS and the phase characteristics with GIXRD and Raman spectroscopy. Only substantial mixing and inter-diffusion could be seen in the as-irradiated specimens. Subsequently, the specimens were flash annealed at 800 °C for 60 seconds in a Rapid

Thermal Processor (RTP). Formations of dose dependent polymorphic $MoSi_2$ phase were established using corroborative results from GIXRD and Raman spectroscopy indicating phase retardation. Post annealing composition revealed from SIMS and RBS indicates formation a graded disilicide phase. The probable role of Ar^+ in phase retardation of *h*-$MoSi_2$ to *t*-$MoSi_2$ is discussed.

Chapter 4: Residual stress in Mo thin films using X-ray diffraction

This chapter deals with the study on evolution of residual stress in sputter deposited polycrystalline Mo thin films as a function of substrate temperature using X-ray diffraction. It discusses the formalism used in the single *hkl* as well as multi *hkl* peak shift analyses and the results are compared. Thermal stress expected at various deposition temperatures were calculated from standard equation and relevant data were taken from standard references. These values were compared with the values of residual stress obtained from X-ray stress analysis. From the comparison, the tensile stress observed at high T_s were discerned as thermal stress due to mismatch in average thermal expansion co-efficient of Mo film and Si substrate. While at low T_s, intrinsic component which were compressive in nature dominates over the thermal component. SIMS depth profile measurements were performed for compositional analysis of the specimens. Based on the compositional distribution, the phenomenon of atomic peening by reflected neutral Ar atoms was ruled out as the cause of compressive stress in the present films. The compressive stress at low T_s was attributed to the incorporation of oxygen impurities in the grain boundaries which possibly occurs during the film growth.

Chapter 5: Effect of microstructure on secondary ion mass spectrometer depth profiling of Mo/Si interface

This chapter deals with the effect of microstructure on the interfacial characterization of Mo/Si with SIMS depth profiling. Mo thin films with varied micro-structural features were prepared by controlling the deposition temperatures during deposition. These microstructures were characterized by cross sectional SEM and were found to closely follow the structure zone model (SZM). The interface broadening that result upon SIMS depth profiling of these films was investigated. Interfacial phase formation and diffusion were ruled out on the basis of the results of GIXRD and RBS. The aspect of degradation in depth resolution due to sputter induced roughness (SIR) of the surface was investigated using AFM. The *rms* roughnesses of the SIMS craters were correlated with the interface width (IW) of the SIMS depth profiles. The effect of original surface roughness on the resulting IWs of the SIMS profiles were investigated by oxidizing the samples through a prolong exposure to ambient. A depth resolved SIMS sputtering and subsequent topographical mapping by AFM shows the evolution of SIR.

Chapter 6: Summary and scope for future work

This chapter outlines important research findings, their implications and recommendation for future work.

LIST OF FIGURES

LIST OF TABLES

LIST OF ABBREVIATIONS

AES	*Auger Electron Spectroscopy*
AFM	*Atomic Force Microscope*
BB	*Bragg Brentano*
CVD	*Chemical Vapour Deposition*
DC	*Direct Current*
GPa	*Giga pascal*
GIXRD	*Grazing Incidence X-Ray Diffraction*
IBM	*Ion Beam Mixing*
ITM	*Implantation Through Metal*
IW	*Interface Width*
MBE	*Molecular Beam Epitaxy*
PID	*Proportional Integral Derivative*
PLC	*Programmable Logic Controller*
PVD	*Physical Vapour Deposition*
RBS	*Rutherford Backscattering Spectrometry*
RF	*Radio Frequency*
rms	*Root Mean Square*
RoI	*Region of Interest*
RT	*Room Temperature*
RTP	*Rapid Thermal Processor*
SB	*Seemann-Bohlin*
SEM	*Scanning Electron Microscope*
SIMS	*Secondary Ion Mass Spectrometry*
SIR	*Sputter Induced Roughness*
SSR	*Solid State Reaction*
SZM	*Structure Zone Model*
XPS	*X-ray Photo Electron Spectroscopy*
XRD	*X-Ray Diffraction*
TEM	*Transmission Electron Microscope*
VLSI	*Very Large Scale Integration*
UHV	*Ultra high vacuum*

CHAPTER 1

A BRIEF INTRODUCTION TO THIN FILMS:

SURFACE AND INTERFACE PHENOMENA

1.1 Why thin films?

Thin films generally refer to materials constrained into an effective 2-dimensional form by limiting one of the physical dimensions i.e., thickness not exceeding few micrometer by a growth process. In context of thin films, a better question has always been ‘why thin films?’ rather than ‘what are thin films?’ Thin films possess unique material properties significantly different from the corresponding bulk. This is due to their dimensional constraint, geometry, microstructure and associated metallurgy that are characterized by the non-equilibrium growth process. The surface properties of the materials often dominate over the conventional bulk properties in thin films regime. This is because of the tremendous increase in the surface area-to-volume ratio brought about by the dimensional constraints. The incorporation of several defects during a growth process provides them different microstructure and metallurgy which manifest in unique properties, for example - increase in resistivity in thin film. Another important aspect of thin films is that their characteristics can be tailored to obtain desired properties. It thus formed a basis for development of several active, passive and mechanical components of devices. Hence, it finds use in applications related to semiconductor industries, microelectronics, optical device, biomedical device, solar industries and protective coating.

1.2 Thin films, thick films and coating

A broad classification based on the thickness regime has long existed in the scientific community. As a rule of thumb, thin film thickness range from 5 nm to 2 microns and thick films thickness vary from several tens of micrometers to hundreds of micrometers. This classification is sometime plausible and usage of 'terms' like thin and thick films are often driven by the usage or application rather than their thickness. If the film is used for surface properties (like electron emission, catalytic activity, reflectivity), then it is called 'thin films', where as if it is used for its bulk

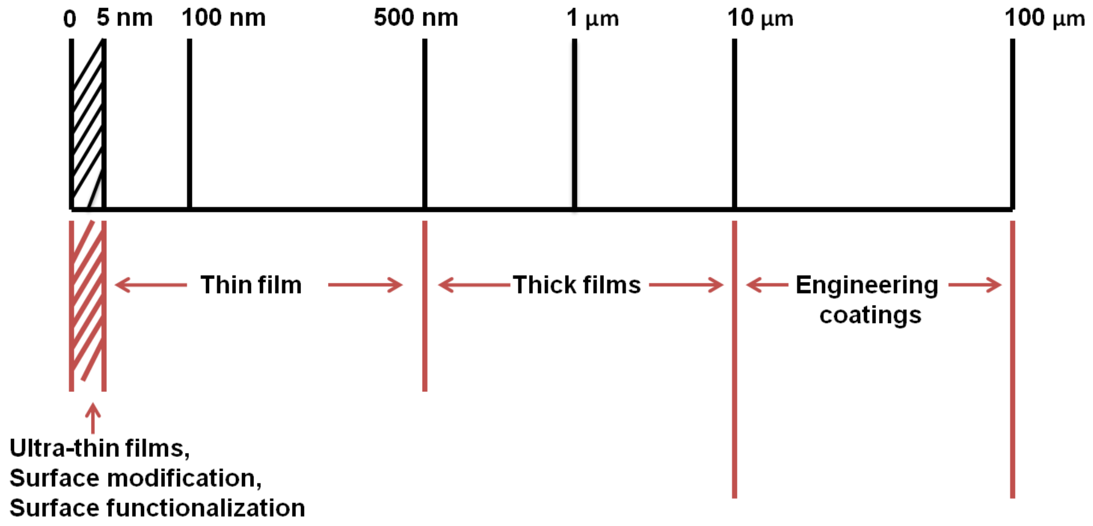

Fig. 1.1 *Thin and thick film regimes.*

properties like wear, erosion, oxidation and corrosion resistance, it is more suitably identified as a thick film [1] or coating, the surface engineering terminology for thick film. And as nanotechnology thrives with the miniaturization of various devices, the so called ultra-thin films has been increasingly investigated in literature, adding yet another dimension to the classification. An ultrathin film contains few layer/monolayer of atoms constituting the material and it includes molecular assemblies, Langmuir-Blodgett films, self-organized surfaces and epitaxial films grown by atomic layer deposition.

1.3 Methods for thin film deposition

All deposition techniques basically entail three distinct steps which are as follows: -

1. Production of the appropriate constituents of atomic, molecular or ionic species.
2. Transport of these species to a suitable substrate through vacuum or a suitable fluid medium.
3. Deposition onto the substrate via direct condensation or chemical/electrochemical reaction and subsequent film growth.

Based on the process that is involved in the deposition, it is classified into two broad categories: -

A. Physical vapour deposition (PVD) process:

The depositing species is vaporized into atomic species, molecules and clusters by physical means like evaporation, ion bombardment and laser ablation. Depositions then take place on the substrate by condensation of the vaporized species and no chemical reaction is involved in the entire process[†]. PVD techniques include evaporation (thermal, e-beam), sputtering (DC, RF, magnetron and ion beam), pulsed laser deposition and molecular beam epitaxy.

B. Chemical vapour deposition (CVD):

The depositing species are mixed with a volatile precursor that acts as a carrier. It involves either homogenous gas phase reactions or dissociation followed by a chemical reaction of gaseous reactant on or in the near vicinity of the heated substrate in an activated environment. CVD techniques include metallo-organic CVD, atomic layer deposition, organo-metallic MBE, plasma and laser assisted CVD.

These two techniques have their own merits and demerits.

1.4 Thin film growth modes

There are three modes of thin film growth:

1. Volmer-Weber mode:

It is also called the island growth mode. In almost all practical cases, majority of films grow by this mode. In this mode, there are strong interactions between ad-atoms, the magnitude of which far exceed that of interaction between the ad-atom and substrate. This leads to nucleation of isolated 3D islands of ad-atoms on the substrate that grows in all directions. The growing islands eventually coalesce to form a continuous film. The surface free energy condition for this growth is expressed as

---

[†] Reactive sputtering may be plausibly confused with a CVD process

$$\gamma_{substrate} < \gamma_{film} + \gamma_{interface} \tag{1.1}$$

2. Frank-Van der Merwe: Layer by layer or epitaxial growth:

This mode required a special compatibility between the substrate and the growing film in terms of lattice parameter matching and chemistry. In the mode, rather than the interaction among ad-atoms, the ad-atoms have a strong affinity for the substrate atoms. As a result, they bond to the substrate forming a sequential 2D layers. This growth often requires extremely slow deposition rate and enhanced substrate temperature. The surface free energy condition for this growth is expressed as

$$\gamma_{substrate} \geq \gamma_{film} + \gamma_{interface} \tag{1.2}$$

3. Stranski-Krastanov: Layer + Island growth:

This is a mixed mode characterized by both 2D layer and 3D island growth. It starts with a 2D layer growth and it switches into 3D island growth after reaching a critical thickness (one or more monolayer) depending upon surface energies and lattice mismatch strain.

The three modes of growth are pictorially depicted in Fig. 1.2.

1.5 Inside thin film – the microstructure

Microstructure is an important characteristic of a thin film which is a direct consequence of poly-crytstallinity and various other competitive processes operative during growth. Of the three growth modes enlisted in section 1.4, polycrystalline metal thin films deposited by PVD techniques commonly follow Volmer-Weber or the island mode of growth. It proceeds via a stage of pre-coalescence nucleation of isolated islands, a coalescence stage of islands merging together and filling of chann-

1. Volmer-Weber: Island growth [2]

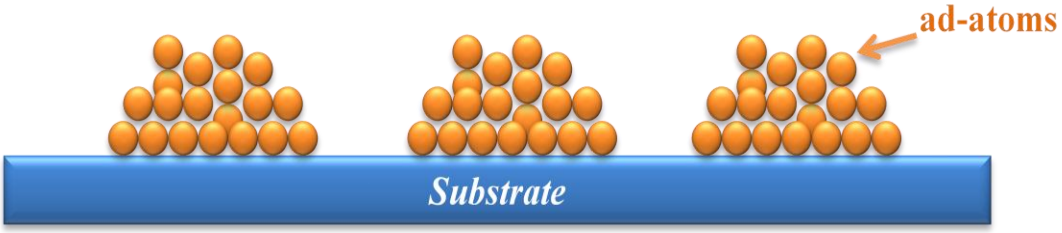

2. Frank-Van der Merwe: Layer by layer or epitaxial growth [3]

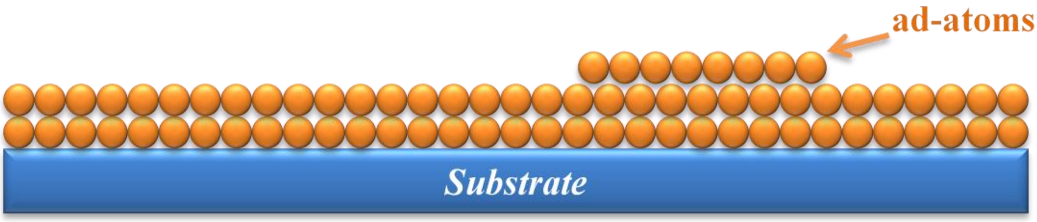

3. Stranski-Krastanov: Layer + Island growth [4]

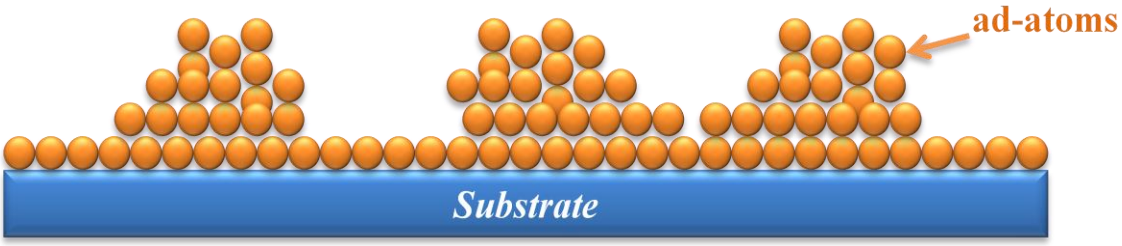

Fig. 1.2 *Different modes of thin film growth.*

-els. These sequential phenomena finally cause continuous film formation. The resulting micro-structure depends both on the deposition parameter and the method of deposition used, especially on parameters that directly affect the surface ad-atoms mobility. For example, a sputtered film tends to have superior micro-crystallinity compared to evaporated ones because of higher ad-atoms energy (~ few eV) for sputtered atoms as compared to evaporated atoms (0.1 eV). Temperature is a parameter that directly affects the ad-atom mobility, though other parameters like pressure (in case of sputtering) also affect it indirectly. A good guide about the relationship between various deposition parameters and the resulting microstructure of the deposited films is the structure zone model (SZM) proposed by Movchan and Demchishin [5] and by J. Thornton [6], although extension and modification to the model were proposed by several others over a course of time [7-8]. The microstructure of the film has a direct bearing on the mechanical properties of the thin film. The yield stress and hence the hardness of a polycrystalline metal thin film varies with the microstructure through grain boundary strengthening mechanism wherein smaller grained films exhibit higher yield stress [9]. The micro-structure plays an important role in the development of residual stress and its evolution in the thin films which affects the film-substrate relation. The microstructure of the film can significantly enhance the diffusion of a species via grain boundary diffusion which provides a much faster and easier diffusion path than n the case of bulk diffusion [10]. It also affects other material properties, often rendering them highly anisotropic. However, with a good understanding of the thin film growth phenomena, the microstructure of the film can be tailored to obtain desired properties by controlling the deposition parameters. This is an enabling tool available at material scientist's disposal.

1.6 Surface and interface

Interface science and engineering is an important branch of material research because of the important role that interface phenomena play in the development of advanced materials and their architectures required for various technological applications. An understanding of the physical and chemical processes that occur at the interface when two materials come into physical contact is important. This is particularly crucial for thin films because thin films are more often explored for their surface and interface properties. Surface exhibit lack of co-ordination in one dimension and possess unsaturated bonding which leads to deformation of bulk crystalline structure and electronic energy bands. Thus the bonding and electronic structure at a solid surface is distinctly different from bulk. These attributes are often gainfully exploited to tailor various functionalities to decisive technological advantage. Similarly, interfaces carry information from both the crystallographic registries in contact and provide novelties with regard to defects, strain-field and band structure attributes.

Hence, the structural composition of the material surfaces and interfaces on atomic scales drastically modify the material properties and govern the underlying macroscopic phenomena. Properties of materials or phenomena like corrosion, adsorption, wear, friction and catalysis depends on the structural composition of the surface or equivalently ‘solid/vacuum’ interface. There are other properties that are governed by the structural composition of internal interface (for example, interface between different material, grain boundaries) like phase formation, brittle fracture, creep, strain and re-crystallization. The realization of technological devices with structures requiring chemical and thermal stability (as in multilayer thin films) for reliable performance is facilitated by the understanding of interfacial micro-chemistry between materials. The mechanical integrity of the thin/multilayer film under different operating ambient is also desirable for reliable performance. In fact, the integration of any new material into an existing technology can be precisely seen as a challenge in interface science. And so it is rightly said that progresses in interface science plays a major role in the future development of advanced materials technology [11].

1.7 Surface and interface analysis methods

With the ever increasing application of thin films in various fields, there is a corresponding increase in the number of experimental techniques that can be used to analyse the surface and interface of thin films. There are above 50 numbers of surface and interface analysis techniques ranging from a traditional optical microscope to the complex of a secondary ion mass spectrometer (SIMS). Each technique probes some characteristics of the surface or the interface which can be topography, morphology, elemental composition and structure. Some commonly used surface and interface analytical techniques are grazing incidence X-ray diffraction (GIXRD), atomic force microscope (AFM), scanning electron microscope (SEM), transmission electron microscope (TEM), SIMS, X-ray photoelectron spectroscopy (XPS) and Auger electron spectroscopy. For the chemical analysis of thin film structures and interfaces, techniques employing combination of ion sputtering and spectrometry, although destructive in nature, have received widespread acceptance [11]. This is because of their superior ability to probe the elemental composition over a wide range of depth with optimal resolution close to atomic monolayer. They can also address interface mixing and diffusion phenomenon across interfaces. Later on, a chapter is dedicated on discussing critical issues in interfacial characterization of crystalline solids using SIMS.

1.7 Motivation for the present work

Thin films are used in a wide range of technological applications. A majority of these technological applications uses thin films in their polycrystalline form. Among them, polycrystalline Mo thin films, subject matter of the present investigation are used as gate electrode, back contact layer in solar cell industry and protective coating [12-13]. The micro-structural characteristics of the Mo films influence several macroscopic properties like residual stress and impurity diffusion among others [14]. Mo has also been investigated extensively in its technologically important disilicide form ($MoSi_2$) for use as interconnect and gate in VLSI technology [15]. The disilicide $MoSi_2$ phase is formed by solid state reaction of Mo thin film with Si substrate initiated either by thermal activation or aided by energetic ion beam irradiation [16-18]. The solid state reaction is reported to have several reproducibility issues as it is highly sensitive to initials conditions and interfacial impurity (eg. native oxides on Si prior to deposition). Therefore, the use of ion beam irradiation to disrupt the native oxide and induce interfacial mixing seems to provide a promising route, especially with the ion through metal (ITM) technique which uses dopant ions (As^+ ,P^+) to induce mixing and silicidation [19]. However, the aspect of forming $MoSi_2$ through inert Ar^+ ion beam irradiation is clearly not investigated. Moreover, there are other interests wherein a chemically and thermally stable Mo and Si interface is desirable, such as the Mo/Si multilayer for use as X-ray mirrors and in UV lithography [20-22]. So, there is a clear need for studies to improve understanding on interfacial characteristics of Mo/Si system. These characteristics includes both phenomenon occurring at atomic scale like inter-diffusion, chemical reaction, phase formation and macroscopic phenomena influencing the mechanical aspect of the film-to-substrate relation like adhesion and macro-stress. The latter aspects influence integrity of the film because of the increasing number of operating environment to which thin films are being increasingly exposed to. The energy stored in mechanically stressed thin films and moisture ingress into the interface can lead to delamination of the film [23]. Residual stresses are inevitable in vacuum deposited thin films [24]. The origin and control of this stress is an active area of research [25]. Stress not only affects the mechanical characteristics but also other associated properties of the material like for example, the superconducting transition temperature of Mo has been reported to vary with residual stress [26]. Measurement of residual stress and understanding the growth process in terms of deposition parameters are necessary for the optimization of synthesis/deposition process and application. Among other techniques, two non-destructive techniques are commonly used: - a) substrate curvature measurement method and use of Stoney's equation [27] and b) residual stress analysis from peak shifts using X-ray diffraction. X-ray stress analysis (XSA) are advantageous over the curvature method as it allows the determination of full stress tensor for all crystallite phases present and can also provide other additional information like texture and crystallite size [28]. However, the traditional $\sin^2\Psi$ method which is performed in the highly penetrating symmetric Bragg Brentano (BB) geometry often fails when applied to thin films [29]. The limiting factor being the low diffraction volume and the corresponding low peak-to-noise ratio and occurrence of crystalline textures. Hence, stress measurements in thin films through X-ray diffraction are performed in an asymmetric diffraction geometry employing a low and fixed angle of incidence [30-32]. While the starting mathematical formalism remains same, these new analyses often involves modifying the plotting axes based upon the assumption made with regards to lattice symmetry, elastic properties and stress state [33]. These modified $\sin^2\Psi$ methods analyzes both single *hkl* and multiple *hkl* peak shifts to find the stress in thin films materials [28-34]. Herein, both approaches are used to study the effect that the deposition temperatures have on residual stress in sputter deposited Mo thin films along with a comparison of these quantitative estimates. A good understanding on the origin of residual stress in these Mo films and better control of deposition parameters can be gained from a detailed study of the observed evolution in residual stress. The relevant competing processes and phenomena that lead to the reversal of stress from compressive to tensile ones upon increasing the deposition temperatures and how it is related to the microstructure is scientifically intriguing. Although compressive stresses in sputter deposited thin films had long been largely attributed to the process of atomic peening from reflected neutral argon [35-37], new insight that suggest different mechanism that may be responsible for the cause of compressive stress in low temperature sputter deposited Mo films are investigated.

While the interfacial characterization, particularly the chemical analysis is necessary, most commonly used techniques for such characterization are the ones based on ion sputtering as mentioned in section 1.7. Among them, SIMS is the most commonly used techniques because of its unique capability to achieve high dynamic range and high sensitivity (ppm – ppb) for all the elements in the periodic table [38]. However, SIMS depth profiles analysis of polycrystalline materials like metal films are difficult because of the associated artifacts and degradation in depth resolution. These degradation and distortion in profile may arise due to several parameters like sputter induced change in surface composition and surface topography, surface roughness, matrix effect and radiation induced effects [39-41]. Hence, a careful data analysis is essential before interpreting a measured depth profile. The correlation of sputter induced roughening and grain size were reported in a published work by

Kiyohisa et al., [42] using Mo thin films deposited on Si substrate having substantial SiO_2 layer on top. However, they employed high primary ion energy (14.5 keV) and beam current (100 nA) which could severely limit the depth resolution. They also relied upon oxygen profiles instead to study the subsequent degradation in depth resolution resulting from non uniform sputtering of crystalline grains. The broadening associated with the interface profile of a polycrystalline bilayer often resembles an apparent diffusion like profile signature and gives rise to ambiguity in analysis. A complete analysis with controlled samples employing complementary techniques will help in thorough understanding of this issue. There are many reports on ion beam induced change of surface topography and resulting degradation in depth resolution. However, they are more confined to other techniques like AES and XPS and still lack discussing this critical issue with necessary evidences to eliminate the ambiguity specifically with regard to SIMS.

1.8 Scope of the thesis

This thesis investigates certain aspects influencing the micro-structural and phase characteristics of thin films and interfaces. The investigation is aimed at both providing an understanding of the evolution of growth and discuss critical issues pertaining to characterization of thin films and interfaces as well. Mo thin films deposited over Si have been chosen as the base system for the present investigation. These investigations include interface mixing, phase formation, micro-structure, residual stress and issues pertaining to interface characterization of the system with SIMS. The deposition temperature dependent micro-structural evolution of sputter deposited Mo thin films are established on the basis of a detailed investigation. The aspect of forming $MoSi_2$ through inert ion beam mixing of Mo/Si thin film bilayer system and subsequent rapid thermal processor (RTP) annealing are discussed. The dose dependence of polymorphic $MoSi_2$ phase evolution is presented. The effect of temperature and the resulting microstructure on the evolution of residual stress are investigated using X-ray diffraction. The use of asymmetric grazing incidence geometry for stress analysis is explored using modified $\sin^2\Psi$ techniques. A comparison between a single *hkl* and multi *hkl* method is presented. An insight into the cause of compressive stress in sputtered deposited Mo thin films is reported based upon the analysis of experimental results obtained in this study. The effect of microstructure in the interfacial characterization of Mo/Si system with SIMS and the ensuing artifacts are discussed based on the experimental results.

References

---

1. R.F. Bunshah, *Handbook of deposition technologies for films and coatings*, Noyes Publication (1994) New Jersey.
2. M. Volmer and A. Weber, Z. Phys. Chem 119 (1926) 277.
3. F.C. Frank and J. H. Van der Merwe, Proc. R. Soc. London, Ser A 198 (1949) 205.
4. J. N. Stranski and L. Krastanov, Ber, Akad, Wiss Wien 146 (1938) 797.
5. B.A. Movchan and A.V. Demchishin, Phys. Met. Metallogr. 28 (1969) 83.
6. J.A. Thornton, *Annu. Rev. Mater. Sci*. 7 (1977) 239.
7. P.B. Barna, M. Adamik, *Thin Solid Films* 317 (1998) 27–33.
8. S. Mahieu, P. Ghekiere, D. Depla, R. De Gryse, *Thin Solid Films* 515 (2006) 1229–1249.
9. N. Hansen , *Scripta Materialia*, 51 (2004) 801 – 806.
10. H. Mehrer, *Diffusion in Solids: Fundamentals, Methods, Materials, Diffusion-Controlled Process*, Springer (2007) New York.
11. S. Hofmann, *Rep. Prog. Phys*. 61 (1998) 827.
12. M. Andritschky and V. Teixeira, *Vacuum*, 43 (5 – 7) (1992) 455 – 458.
13. A. Bollero, M. Andrés, C. García, J. de Abajo and M. T. Gutiérrez, *Phys. Status Solidi A* 206, No. 3, (2009) 540–546.
14. J-H. Yoon, T-Y Seong and J-h Jeong, *Prog. Photovolt: Res. Appl*. 21 (2013) 58–63.
15. G. VALYI, H. Ryssel, W. Moller, *Nucl. Instr. And Methds. In Phys. Research B* 39 (1989) 268.
16. M. A. Nicolet, S.S. Lau, VLSI Electronics 6, ed., N.G. Einspruch, Academic Press, New York, (1983) 330-459.

17. T. Gessner, R. Reich, W. Unger, W. Wolke, *Thin Solid Films* 177 (1989) 255.
18. A. Zambova, I. Nedev, *Vacuum* 43 (1992) 223.
19. R. S. Rastogi, V. D. Vankar, K. L. Chopra, *Thin Solid Films* 164 (1988) 449
20. J. M. Slaughter, A. Shapiro, P. A. Kearney, C. M. Falco, *Physical Review B* 44 (1991) 3854.
21. I. Nedelcu, R. W. E. van de Kruijs, A. E. Yakshin, F. Bijkerk, *Physical Review B* 76 (2007) 245404.
22. T. Chass’e, H. Neumann, B. Ocker, M. Scherer, W. Frank, F. Frost, D. Hirsch, A. Schindler, G. Wagner, M. Lorenz, G. Otto, M. Zeuner and B. Rauschenbach,*Vacuum* 71 (2003) 407–415.
23. P. Waters and A. A. Volinsky, *Exp. Mech.*, 47 (2007) 163-170.
24. J.A Thornton and D.W. Hoffman, *Thin Solid Films*, 171 (1989) 5 -31.
25. L. B. Frreund and S. Suresh, *Thin Film Materials: Stress, Defect Formation and Surface Evolution*, Cambridge University Press (2003) UK.
26. L. Fabrega, I. Fernandez-Martinez, M. Parra-Borderias, O. Gil, A. Camon, R. Gonzalez-Arrabal, J. Sese, J. Santiso, J.-L Costa-Kramer and F. Briones, *Applied Superconductivity,* 19, no.6 (2009) pp.3779 – 3785.
27. G.C.A.M. Janssen, M.M. Abdalla , F. van Keulen, B.R. Pujada and B. Van Venrooy, *Thin Solid Films* 517 (2009) 1858–1867.
28. U. Wezel, J. Ligot, P. Lamparter, A.C. Vermeulen and E. J. Mittemeijer, J. Appl. Cryst. 38 (2005) 1-29.
29. C. Quaeyhaegens, G. Knuyt and L.M. Stals, Surf. Coat. Technol., 74-75 (1995), 104 -109.
30. C.-H. Ma, J.-H. Huang, H. Chen, Thin solid films 418 (2002) 73-78.

31. K. V. Acker, L. De Buyser, J. P. Celis and P. V. Houtte, J. Appl. Cryst. 27 (1994) 56-66.
32. V. Valvoda, R. Kuzel, JR., R. Cerny, D. Rafaja, J. Musil, S. Kadlec and A.J. Perry, Thin Solid Films 193/194 (1990) 401-408.
33. A. C. Vermeulen, Mater. Sci. Forum, 404-407 (2002) 35-42.
34. A. Baczmanski, C. Braham, W. Seiler and N. Shiraki, Surf. Coat. Technol. 182 (2004) 43-54.
35. J. A. Thornton and D. W. Hoffman, *J. Vac. Sci. & Technol*, A3 (1985) 576.
36. J. A. Thornton, J. Tabock and D. W. Hoffman, *Thin Solid Films*, 64 (1979) 111-119.
37. D. W. Hoffman and J. A. Thornton, *Thin Solid Films*, 40 (1977) 355-363.
38. A. Benninghoven, F.G. Rüdenauer and H.W. Werner, *Secondary Ion Mass Spectrometry: Basic concepts, Instrumental Aspects , Applications and Trends*, Wiley, New York (1987).
39. A. Zalar, S. Hofmann, *Vacuum* 37 (1987)169-173.
40. Y. Gao, Y. Marie, F. Saldi, H. N. Migeon, *International Journal of mass Spectrometry and ion Process* 143 (1995) 11 – 18.
41. N. Q. Lam, *Surf. Interface Anal.* 12 (1988) 65.
42. Kiyohisa Fujinaga and Izumi Kawashima, *J. Vac. Sci. Technol. A* 6 (1988) 213.

CHAPTER 2

EXPERIMENTAL TECHNIQUES

2. 1 Introduction

This chapter explains the details of the various experimental techniques used in the present thesis. It includes techniques for sample preparation, treatment and characterization. The thin film samples were prepared using a radio frequency (RF) magnetron sputtering unit. The as-prepared as well as the flash annealed samples were characterized using various techniques which includes grazing incidence X-ray diffraction (GIXRD), secondary ion mass spectrometry (SIMS), Rutherford backscattering spectrometry (RBS), scanning electron microscopy (SEM) and atomic force microscopy (AFM). The thin film samples were flash annealed in a rapid thermal processor (RTP).

2.2 Thin film sample preparation

The thin films samples were prepared using radio frequency (RF) magnetron sputtering unit, a variant of physical vapour deposition (PVD) technique outlined in chapter 1. This deposition technique makes use of the sputtering process wherein target atoms are ejected from the surface of the target upon energetic particle bombardment. The bombardment set off a collision cascade in the target and sputter-

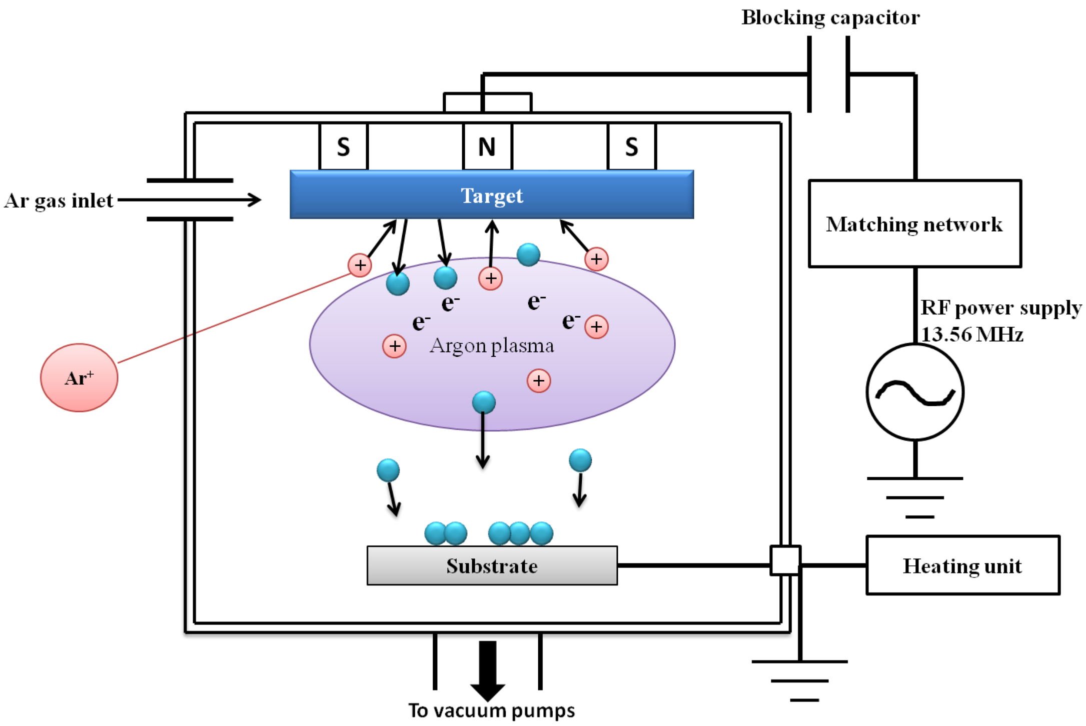

Fig. 2.1 *A schematic diagram showing the working of a RF magnetron sputtering.*

-ing results from the backward recoils that reach the surface with energies above the average surface binding energy. All the variant of sputter deposition processes relies on sustained glow discharge plasma created by breakdown of a gas/gaseous mixture at low pressure by the application of an electric field. The discharge in a RF magnetron sputter deposition process is a capacitive discharge as can be seen in Fig. 2.1, where the target (cathode/power electrode) is coupled to the RF generator that produces a RF field at 13.56 MHz frequency through a blocking capacitor. The anode (substrate) is usually grounded. A consequence of this capacitive coupling is the development of self biasing of the target that is negative with respect to the plasma potential necessary to make the average charge current over one RF cycle zero. This provides an effective negative DC voltage offset that is needed to sputter the target (irrespective of its electrical nature) by the Ar^+ ions. Magnetrons are permanent magnet add-ons so configured with the cathode surface to trap electrons near the cathode and maximize sputtering efficiency by using magnetic and electric fields. It can be used with DC, pulsed DC and RF sputter source. Thus RF magnetron sputtering is a universal technique capable of depositing both conducting as well as non-conducting thin films. Fine details about sputtering and all the variants of sputtering deposition are available in the handbook of thin film deposition by R.F. Bunshah [1]. Details about the deposition unit and the parameters used in depositing the samples for the present thesis work are given below.

The deposition chamber was evacuated to a base pressure of ~ 5 x 10^{-6} mbar using a combination of rotary and turbo-molecular pump. The sample stage is equipped with heater controlled by a proportional integral derivative (PID) controller and it can heat samples/substrates up to 800 °C. The heater and the thermocouple assembly are hermetically packed in a vacuum compatible metal casing and aluminium foils are wrapped upon the thermocouple leads. These arrangements lead to formation of Faraday’s cages which act as an effective shield against RF interferences. The distance between the substrate and the target d is ~ 6 cm. The working pressure p in the chamber is about 1.5 – 4 x 10^{-3} mbar and hence, the $p \times d$ ~ 0.6 to 2.4 Pa – cm. The target is 99.9% pure Mo target and sputtering proceeds through plasma created by argon gas feed. The substrates used were *n*-Si (100) and *p*-Si (111) single crystal wafers. The wafers were cleaned by a series of alternating steps involving ultra-sonication and dip rinsing in organic solvents (acetone and ethanol) and deionised water. The silicon substrates were finally dried using hot air blower (from the backside) before they were loaded into the deposition chamber. Initial optimization of the deposition parameters, especially, the sputter power was performed using the surface roughness (*rms* roughness) of the as-deposited films as a parameter by depositing films at different sputter powers ranging from 70 W to 200 W. Based on the value of *rms* roughness measured by AFM, sputter power of 130 W was chosen for the deposition. The thicknesses of the films were measured by masking a portion of the film and doing a post deposition stylus measurement. Molybdenum thin films with desired thickness were deposited for a particular set of deposition parameters by using the calibrated deposition rate with an error of ~ 5%. Different sets of films were prepared with different deposition parameters. Different set of Mo thick films were deposited using different deposition parameters for various investigations which makes up the present thesis. 43 nm thin Mo films were deposited on Si substrate to study interface mixing upon Ar^+ ion irradiation and subsequent formation of technologically important molybdenum disilicide ($MoSi_2$). Thicker Mo (~ 160 – 200 nm) thin films with varying microstructures were also deposited on Si substrate using different substrate/deposition temperatures (RT to 800 °C) to study issues related to interfacial characterization and diffusion with SIMS. Samples were also prepared to study the effect of deposition temperature on the residual stress in Mo thin films. These studies are discussed in details in later chapters.

2.3 Secondary ion mass spectrometry (SIMS)

SIMS is a versatile surface and near surface micro analytical technique that can perform elemental and isotopic depth profiles, in thin films and bulk materials with high depth resolution. This technique is capable of detecting trace levels of all the elements in the periodic table with varying degrees of sensitivity i.e., in the range of ppm - ppb (10^{-6} - 10^{-9}) atomic concentration [2]. The high sensitivity comes from the inherent capability towards trace analysis that is associated with a mass spectrometry technique. The schematic diagram of SIMS is shown in Fig. 2.2 below.

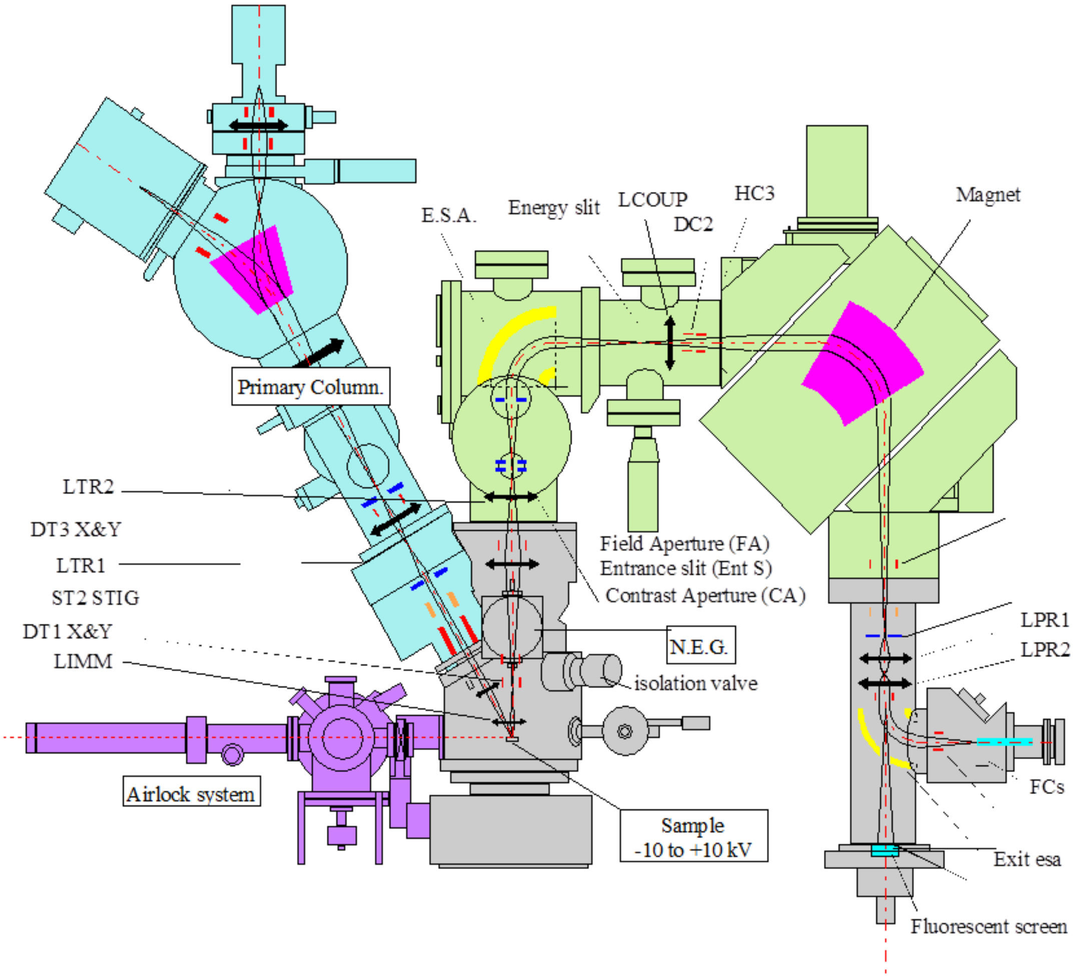

Fig. 2.2 *A schematic diagram of a secondary ion mass spectrometer.*

The basis of SIMS technique is the use of focused primary ion beam (few kV) as a microprobe to systematically sputter the sample's surface to eject secondary ions which are then mass analyzed. The primary ion beam (O_2^+, O^- or Cs^+) bombardment induces a collision cascade and sputtering process results from the backward recoil. The Cs^+ primary ions are produced by thermionic surface ionization of a Cs containing compound like Cs_2CO_3, while O_2^+ (and O^-) primary ions are produced by a

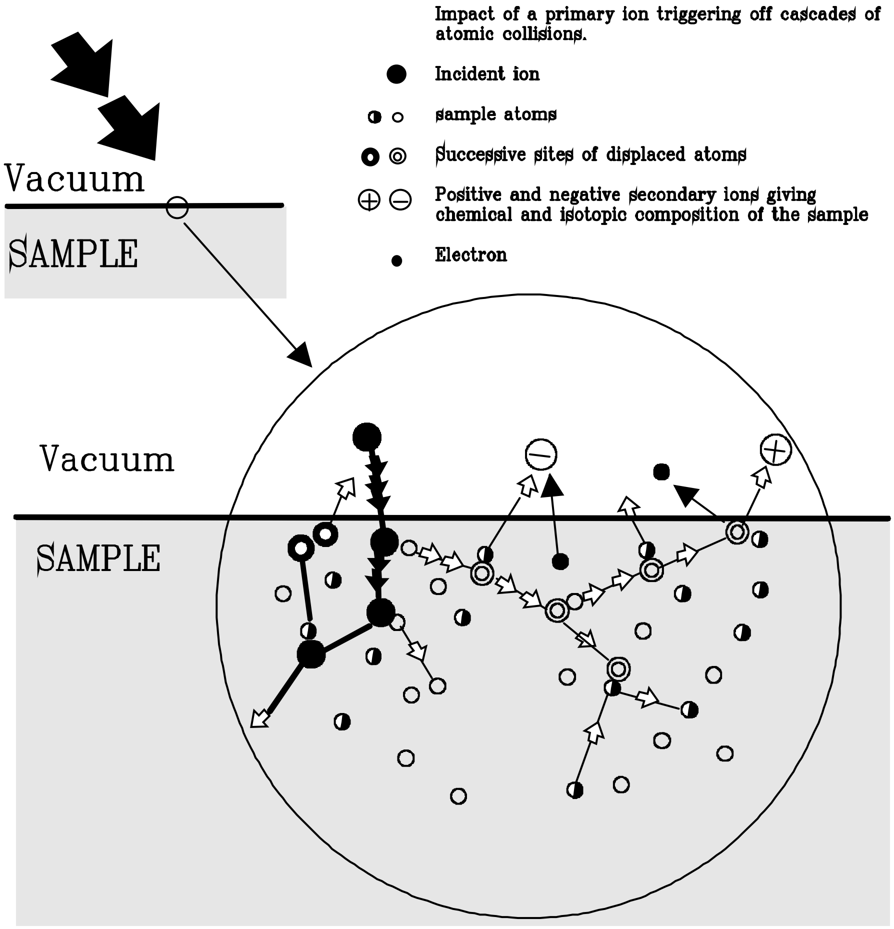

Fig. 2.3 *A schematic diagram showing the interaction of primary ion and the sample surface.*

cold cathode plasma discharge in a duoplasmatron. The secondary species that are ejected during primary ion bombardment induced sputtering process includes electrons, photons, resputtered primary ions, neutral atoms, charged monatomic/polyatomic (molecule) or clusters with energy ranging from 0 to several hundred eV. A schematic representation of the primary ion interaction with the sample surface is shown in Fig. 2.3.

A fraction of the sputtered atomic species undergoes charge exchange in the near surface environment resulting in the formation of secondary ions, either positively/negatively charged, which carries characteristics of the sample surface. The basic SIMS equation which relates the secondary ions intensity of species m in the layer with various fundamental parameters is given by

$$I_s^m = I_p Y_m \alpha \, q_m \, \eta \tag{2.1}$$

where I_p, Y_m, α, q_m, *and* η are the primary ion intensity, total sputter yield for species m, ionization probability, fractional concentration of species m in the surface layer and the instruments transmission efficiency respectively. These secondary ions (most often positive than negative) are extracted by an electrical potential and subsequently analyzed in a mass spectrometer to give the composition of the sample. The ion detectors at the detecting ends include a Faraday cup, electron multiplier, micro-channel plate and resistive anode encoder. The SIMS uses a combination of these detectors to offer a high dynamic range in detection by covering a wide range of count rate from 10 to 5 x 10^9 counts per second. Detailed information on the working principle of SIMS and its instrumentation are available in the book by *A. Benninghoven* [1].

There are several operating modes for carrying out analysis using SIMS:

1. Dynamic SIMS for compositional depth profiling
2. Static SIMS for surface analysis
3. Imaging SIMS
4. Mass spectrum
5. Bar graph
6. High resolution
7. Line scan

Among the modes listed above, the first three modes of analysis are routinely used. Static SIMS uses low primary ion dose (below 1 x 10^{12} ions/cm^2) for qualitative analysis of the top sub-monolayer of the sample to determine surface concentrations of elements and molecules without significantly altering the analyte. Spectrometer with time-of-flight detector is best suited for static SIMS. Spectrometer with magnetic sector like the CAMECA IMS 7F SIMS is more suited for dynamic SIMS analysis of thin films and bulk samples. With dynamic SIMS which involves use of much higher energy primary beam (large current), one can analyze trace impurities and variation in elemental composition with depth from the so called depth profiles [3]. Dynamic SIMS is well suited for studying solid state diffusion, interface mixing and impurities profiles in thin films/multi-layers structures. Imaging SIMS is yet another mode of SIMS. It provides spatially-resolved elemental mapping of the sample or analytes. Imaging can be performed either in *scanning ion /ion micro-beam mode* 'or' *direct ion/ion microscope mode* depending upon the image that is focused on the detector plane and the detector used.

SIMS measurement forms an important experimental part of this present thesis. All the SIMS measurement were carried out in a CAMECA IMS 7F SIMS with Cs^+ primary ions produced by thermionic surface ionization - Cs vapor emanating from a resistively heated reservoir (Cs_2CO_3) thermally ionizes to Cs^+ ions when it is passed through porous tungsten plate heated to 1100 °C. The interface mixing between Mo and Si in Mo/Si bilyaer thin films upon ion beam irradiation has been investigated with SIMS. The issues and artifacts related SIMS depth profiling of polycrystalline materials are investigated using Mo thin films with varied micro-structure. Impurity profiles in Mo thin films sputter deposited at ~ 4 x 10^{-3} mbar at various temperatures. Studies of homogeneity in ion beam mixed zone using SIMS ion imaging with a resistive anode encoder and the power of the offline analysis software are also presented.

2.4 Rutherford backscattering spectroscopy

RBS is a nuclear analytical technique widely used for the elemental and compositional analysis of near surface layer of materials. Projectiles with energies between 100 keV to 4 MeV bombard a target and an energy sensitive detector records the energies of the backscattered ions. The scattering in RBS includes both elastic scattering and inelastic scattering and covers nuclear reaction regime as well. The projectile normally uses includes protons (H^+) or doubly ionized α- particles (He^{++}) as the Rutherford cross section are better known for these ions, stopping power extensively investigated and incur less damage among other ions of comparable energies. Sometime, Li^+ ions are also used as projectiles.

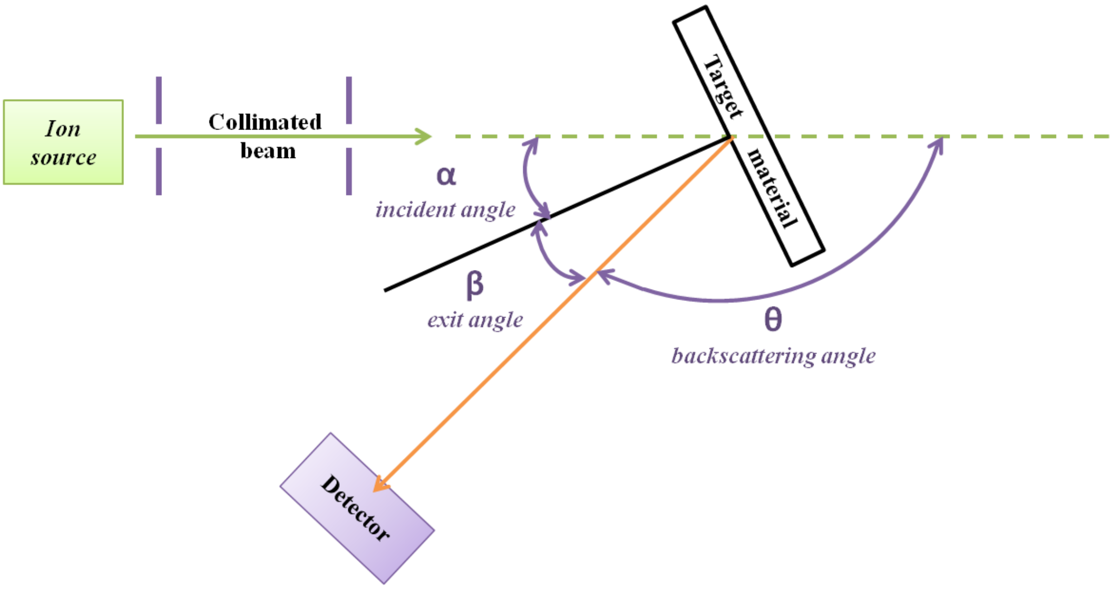

Fig. 2.4 *A schematic of the experimental set-up for Rutherford backscattering geometry (IBM).*

A schematic of a typical RBS setup in the IBM geometry is shown in Fig 2.4. In IBM geometry, the incident beam, exit beam and surface normal are in the same plane and they satisfies the condition

$$\alpha + \beta + \theta = 180^{\circ}.$$

The simplicity of two-body kinematics can be applied to the backscattering events (with appropriate energy losses consideration). The energies of the backscattered projectile (ions) incident with energy E_0 and having mass M_1 depend on the mass M_2 of the target atoms as

$$E_1 = KE_0 \tag{2.2}$$

where

$$K = \frac{M_1^2}{(M_1 + M_2)^2}\left\{\cos\theta \pm \left[\left(\frac{M_2}{M_1}\right)^2 - sin^2\,\theta\right]^{\frac{1}{2}}\right\}^2 \tag{2.3}$$

is called the kinematic factor, *defined as the ratio of the projectile's energy after and before the collision.* Significant amount of momentum (energy) is transferred to the light target atom by the incident projectile. As the mass of the target atoms M_2 increases, much reduced momentum is transferred and the energy of the back-scattered ions asymptotically approaches the incident projectile energy. The energy separation is given by

$$\Delta E_1 = E_0 \frac{dK}{dM_2} \Delta M_2 \tag{2.4}$$

And hence RBS has good mass resolution for lighter elements, but good sensitivity for heavier elements in lighter target and vice versa.

The energy of backscattered ions (as well as yield) is also a function of the depth from which the ions are back-scattered. This occurs because of the energy losses suffered by the ions during inward and outward travels within the target. With the knowledge of the stopping power *S*, *defined as the energy loss (nuclear and electronic collisions) per by unit distance traversed*, of the projectile in the material, the measured energy E_1 can be converted into a depth scale x to give elemental depth profiles or thickness. At low energy (< 100 keV), the nuclear stopping due to collision with target nuclei is important, while electronic stopping gain importance with increasing energy. The stopping power is related to the scattering cross section ϵ by the relation

$$\epsilon = \frac{S}{N} = \frac{1}{N}\frac{dE}{dx} \tag{2.5}$$

where *N* is the density of the target material.

The energy loss by the ions in both inward and outward path is governed by the $\boldsymbol{S}$ or ϵ which are characteristics of each material. For a compound consisting of different elements i with atomic concentrations c_i, Bragg's rule gives the total scattering cross section as

$$\epsilon = \sum_i c_i \epsilon_i \tag{2.6}$$

where ϵ_i is the scattering cross section of individual element. Fine details about the RBS technique and related mathematical analysis are available in many books [4-5].

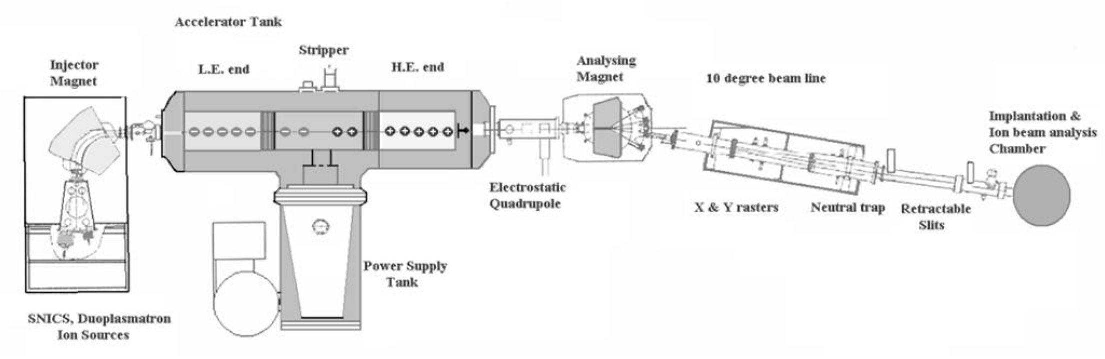

Fig. 2.5 *The schematic diagram for the 1.7 MV tandetron accelerator.*

A 1.7 MV Tandetron accelerator was used for performing the RBS experiments presented in this thesis. The schematic diagram of the accelerator is shown in Fig. 2.5 and the image of the 1.7 MV tandetron accelerator in Fig. 2.6. The accelerator works on the principle of *tandem acceleration* i.e. the ions are accelerated twice using the same high voltage applied at the middle of the accelerating tube. Negative ions generated by the source are initially accelerated by the high voltage terminal at the middle of the tube, where a stripper canal filled with nitrogen gas converted them into positive ions which are again accelerated by the same high voltage terminal towards ground potential. The maximum energy of positive ions transformed from negative ions into charge 'q' and accelerated by a terminal voltage 'V' has the energy given by

$$E = V\,(1+q) \tag{2.7}$$

The configuration has another advantage of having both the ion injection system and target at the ground potential. There are two ion sources for beam injection namely (i) a duoplasmatron ion source for production of H^+ and He^+ ions

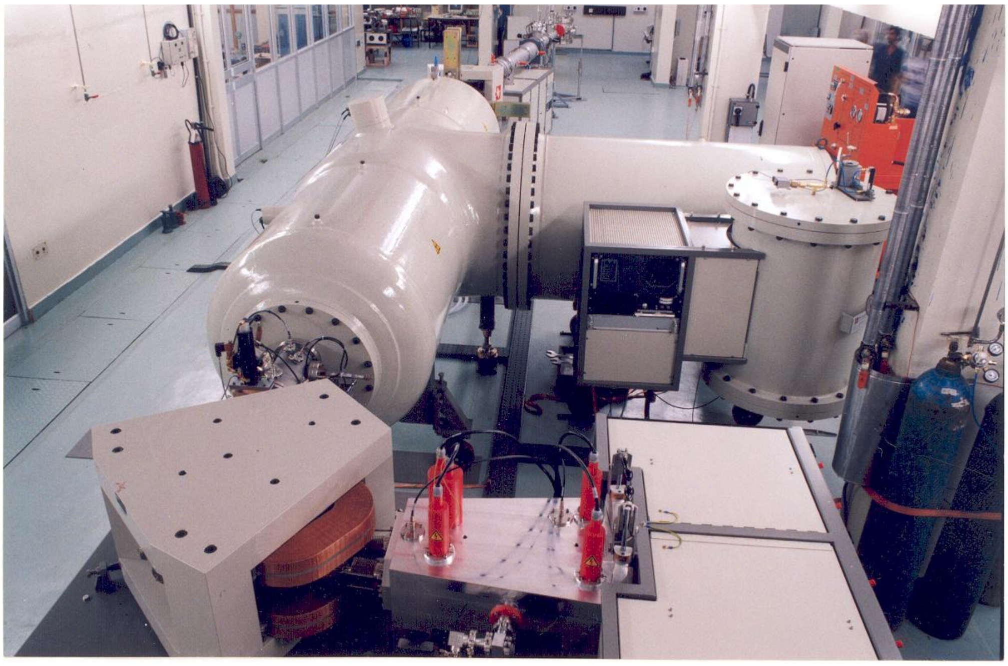

Fig. 2.6 *The 1.7 MV tandetron accelerator.*

and (ii) a SNICS (Source of negative ions by cesium sputtering) sputter source capable of producing negative ions of almost all elements. The beam injection into the accelerator is facilitated by a 90° mass analyzing magnet (resolution ~ 190) for both ion sources. High voltage insulation of the entire accelerating structure is achieved byenclosing it with a pressure vessel filled with SF_6 gas at 6 kg/cm^2. An ultra high vacuum of 10^{-7} mbar is maintained in the accelerating tubes and a turbo-molecular pump has been installed at the high voltage terminal for recirculation of the stripper gas. The high voltage in the range 100 kV to 1.7 MV with a high stability of ± 100 V is generated using a Cockroft-Walton type solid state power supply. The accelerated ions are focused by an electrostatic quadruple lens before a high energy switching magnet analyzes the energy of the beam and switch it to the experimental ports located at ± 10° and ± 30° angular positions. An implantation beam line with a beam sweep system, neutral trap, beam profile monitor and retractable slits for beam collimation has been installed at the 10° port of the switching magnet. An UHV compatible irradiation cum ion beam analysis chamber (Fig. 2.7) has been installed at the end of the beam line. The RBS measurements work presented in this thesis were performed in this chamber.

And the computer simulation program known as SIMNRA develop by M. Mayer [6] for analyzing RBS spectra was used to model the compositional layer of acquired RBS spectra for various samples.

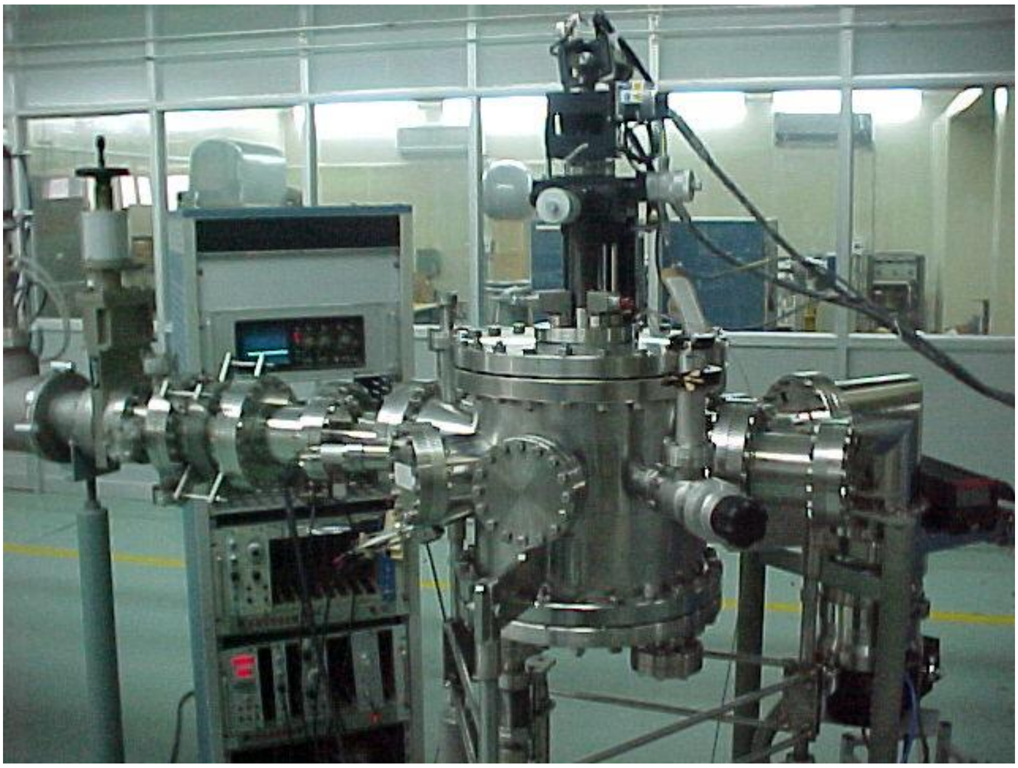

Fig. 2.7 *The ion beam analysis chamber.*

2.5 Grazing incidence X-ray diffraction

X-ray diffraction experiments for fairly thick films and bulk samples are generally performed in the symmetric Bragg-Brentano (BB) diffraction geometry. The BB geometry is highly penetrating (10 – 100 μm) [7] and is most often not useful for analyzing thin to very thin films (nm range) because of the correspondingly low diffraction volume within the thin film that results in a very low peak-to-noise ratio and poor structural information about the film [8]. When an X-ray diffraction experiment is performed in an asymmetric geometry employing a low fixed grazing incidence, it is referred to as GIXRD. A schematic of grazing incidence X-ray diffraction (GIXRD) configuration is shown in Fig. 2.8.

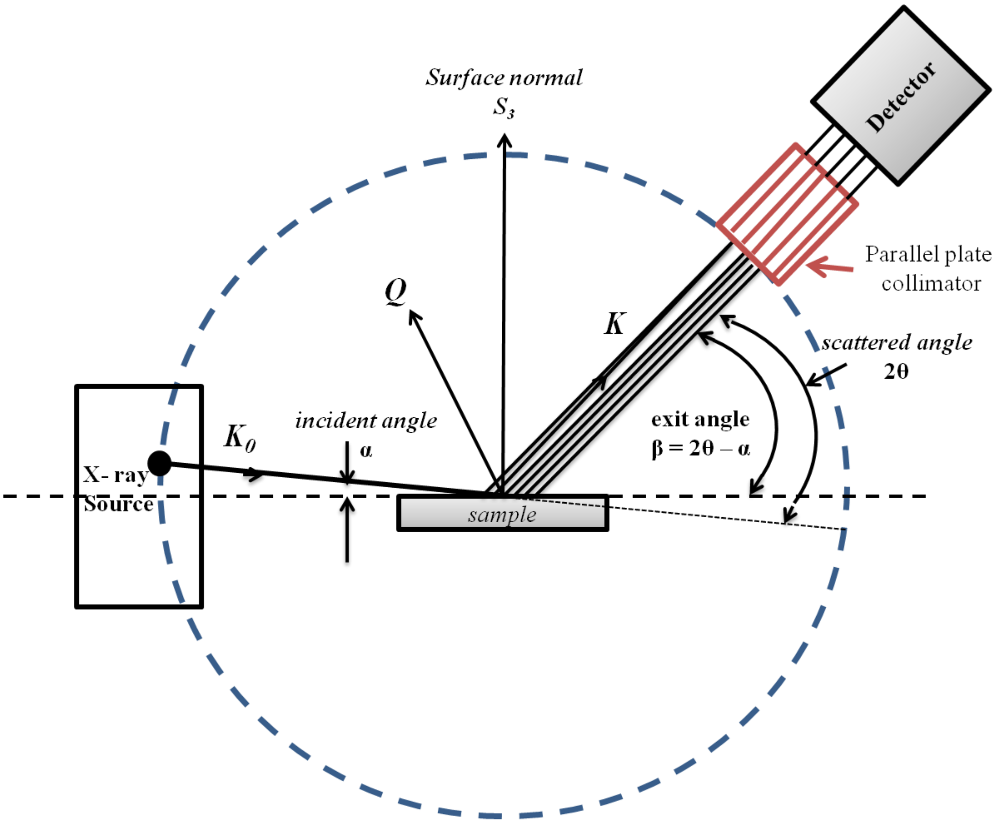

Fig. 2.8 *A schematic diagram of the experimental configuration for grazing incidence X-ray diffraction.* $\boldsymbol{K_o}$*,* ***K*** *and* ***Q*** *are the incident wave vector, scattered wave vector and the scattering wave vector respectively.*

As in the symmetric (BB) case, the configuration is still coplanar with wave vectors $\boldsymbol{K_o}$, $\boldsymbol{K}$ and $\boldsymbol{S_3}$ all lying in the same plane. However unlike in BB geometry, the incident angle is kept fixed at a low value near critical angle and the detector scans the 2θ circle. The crystalline planes scattering the X-rays are no longer the plane parallel to the sample surface, but planes perpendicular to the Q vector as shown in Fig. 2.8.

The advantage of using a low and fixed incidence angle is that it limits the penetration of the X-ray beam and maximizes the diffraction volume within the thin films by increasing the path length as well as foot prints of the X-ray beam within the thin film specimen as shown in Fig. 2.9. The path length of the X-ray beam within a film of thickness t becomes $l = t/\sin\alpha$ which can be multiple times of the actual thickness of the film and the foot print (of the X-ray beam with width d) = $d/\sin\alpha$.

The penetration depth of X-ray in a material having a linear absorption co-efficient μ is given by the equation

$$\tau = \frac{\sin\alpha\sin\beta}{\mu(\sin\alpha + \sin\beta)} \tag{2.8}$$

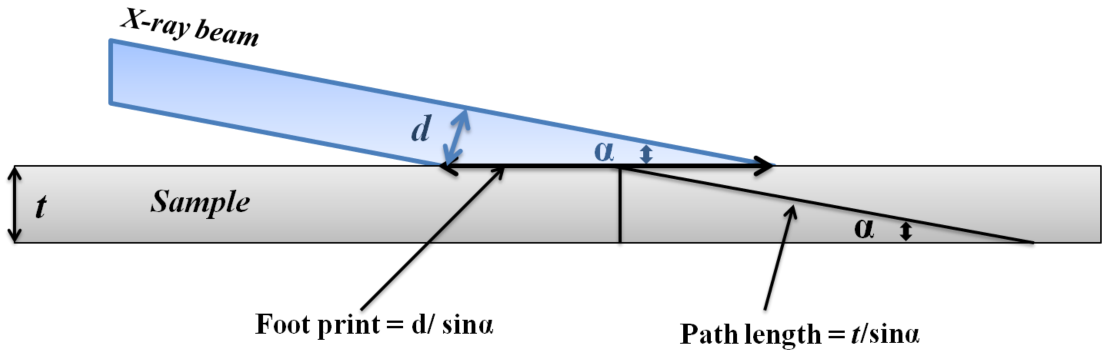

Fig. 2.9 *X-ray path length and foot print in GIXRD.*

where α, β are the incident exit angle of the X-ray respectively. The essence of this depth is that about 63 % of the diffracted beam originates from depth τ below the sample surface.

In GIXRD, the penetration depth varies strongly for values of α near the critical angle according to the above expression, but if α is not too close to the critical angle i.e., if θ^{hkl} is not in the vicinity of 0 or 90°, it can be approximated to the expression

$$\tau = \frac{\sin\alpha}{\mu} \tag{2.9}$$

A reliable choice of α is guided by the criteria that the average path length

$$l = \frac{1}{\mu} \tag{2.10}$$

The X-ray diffraction data are not just limited to structural information such as the crystalline phases and sizes. A well equipped lab source X-ray diffractometer can give information regarding the full stress tensor, strain and textures. Synchrotron X-ray sources can still give more information including that of amorphous materials. The XRD measurements presented in this thesis were performed in two diffractometer systems namely: - (a) Stoe GmbH diffractometer and (b) Bruker Discover D8 Diffractometer. The STOE diffractometer works with Cu k_α (λ = 1.5406 Å) produced by a tube source and experiments were performed in the parallel beam grazing incidence geometry with sample rotation. The phase characterization of the ion beam irradiated Mo/Si samples were performed in the Stoe diffractometer. The Bruker D8 diffractometer is a four circle diffractometer and is equipped with a 6 kW rated rotating Cu anode generator that produces pure Cu k_α (λ = 1.5406 Å) with intensity that is much higher than the conventional tube source diffractometer. The rotating anode generator is operated at 4.5 kW and 100 mA current in a vacuum of 1 x 10^{-7} mbar. The Eulerian cradle (i.e., goniometer) in the D8 diffractometer allows the sample to the tilted and rotated along any specific orientation using χ and φ axis making it well suited for residual stress and texture measurements. These are in addition to routine diffraction investigation for structure analysis. Hence, the involved measurements for stress analysis were performed in the Bruker diffractometer as specified in the respective chapters that is to follow. The stress measurements were performed in the asymmetric parallel beam geometry with a 0.7° angle of incidence following a modified $\sin^2\Psi$ method of analysis. The χ axis was used to vary the sample tilt angle Ψ. Measurements were also made with detector (2θ) scan in an extended range from 30º to 145º to record all measurable reflections. These extended 2θ scans form the basis of residual stress analysis using multiple *hkl* reflections.

2.6 Ion beam irradiation - 150 kV gaseous ion implanter

Materials undergo significant atomic rearrangement when irradiated with energetic ions. The phenomenon is referred to as *ion beam mixing* if the atomic intermixing and alloying due to ion irradiation occurs at the interface separating two materials eg.: the interface of binary or multi-layer thin film systems [9]. The ion beam irradiation of the Mo/Si thin films in the present thesis were performed in *J*-15 gaseous ion accelerator facility. A schematic diagram illustrating the layout of the ion irradiation facility is shown in Fig. 2.10 and the 150 kV accelerator used for the purpose is shown in Fig. 2.11. The accelerator is an electrostatic accelerator and it consists of a radio frequency (RF, 100 MHz) gaseous ion source. The ions are then extracted from the source and accelerated along the accelerating tubes to the required

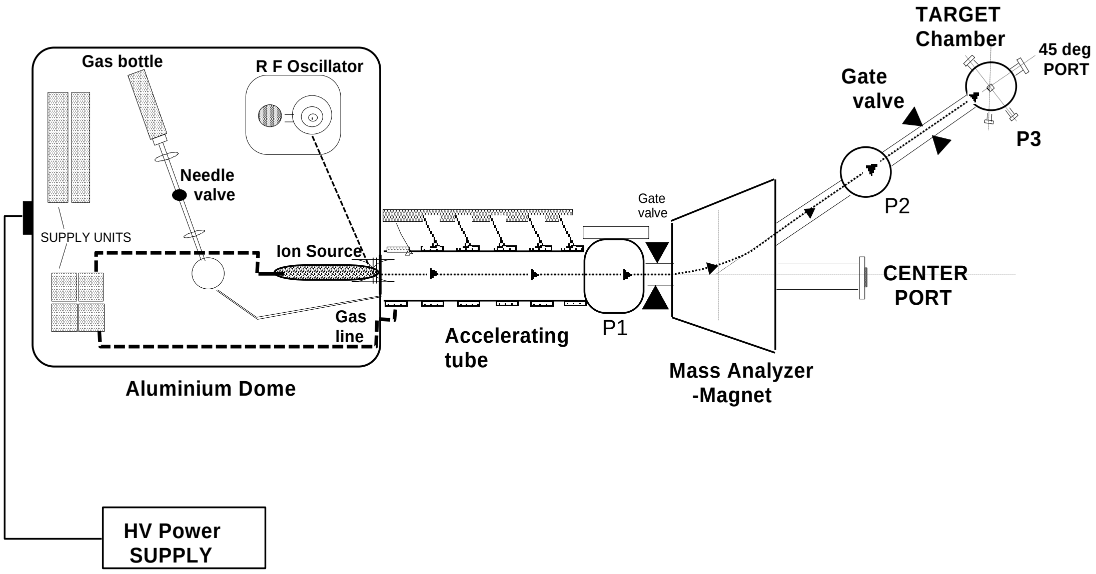

***Fig. 2.10** A schematic diagram of the experimental set-up for J 15 150 kV gaseous ion accelerator.*

***Fig. 2.11** J 15 150 kV gaseous ion accelerator.*

voltage in the range 10 – 150 kV. A Cockfoft –Walton voltage generator produce the required high power voltage (tuneable 10 – 150 kV). The ions are mass analyzed by a 45° bending electromagnet with appropriate magnetic field. The accelerated mass analyzed ion beam is collimated and focused using an electrostatic quadropole lens, and allowed to impinge on the sample placed inside an irradiation chamber. The irradiation chamber as well as the accelerating tube are maintained at ultra high vacuum (~10 -7 mbar) using a turbo-molecular pump. A liquid nitrogen trap is used for trapping organic contaminants to maintain oil free vacuum.

The beam current and ion dose (ions/cm^2) were measured using a current integrator. To facilitate beam current measurements, the sample stage is made out of a block of copper which is insulated from the rest of the chamber. A secondary electron trap (Faraday cup) is used to eliminate error in beam current measurement resulting from emission of secondary electrons form the target. A 40 V potential is used to suppress the secondary electrons from escaping the Faraday cup (thin metallic cylinder). A low beam current 0.5 μA was maintained during the irradiation to avoid the beam heating of the sample during irradiation. An X-Y beam rastering was used over an area of 1 cm^2 for uniform irradiation of the sample. All the irradiations were carried out at room temperature. The gaseous ions used for the irradiation work of this thesis are Ar$^+$ ions and the energy of the ions were 110 keV.

2.7 Scanning electron microscopy

The SEM is a microscope that uses a focused beam of electrons to scan the surface of a sample. The major advantages of SEM over ordinary microscope are the large depth of field and a much higher resolution (down to few nm) which provides a clear 3D image of the topographical features of the scanned sample surface. The maximum magnification and hence resolution is decided by the minimum diameter of the focused electron beam. Resolution down to 1 nm is achievable with SEM equipped with field emission (FE) electron gun compared to ~ 10 nm that can be achieved with normal SEM with thermionic electron source. The interaction of these impinging electrons with the atoms of the sample surface produces various secondary signals. These secondary species gives information on sample's elemental composition and topography based on whether characteristics X-rays or backscattered and secondary electrons are detected. Detection of back-scattered electrons (BSE) can tell about the distribution of mean atomic number of the sample as BSE signals are atomic number dependent (bright regions associated with heavy elements). Combining BSE with characteristic X-ray spectrometry, one can get elemental distribution of different elements present in the sample. X-ray spectrometry alone can perform elemental analysis of all elements down to atomic number 5 (boron) in a scanned area few mm wide and deep. The most commonly detected signal is that of secondary electrons emitted by surface atoms excited by the probing electron beam. The number of secondary electrons is a function of angle between the probing beam and the emitting surface, and hence it contains information about the topographical features of the surface.

In the present thesis, a Gemini make FE-SEM was used for imaging the microscopic or morphological features of the Mo films deposited at different temperatures. Cross sectional scanning micrographs were acquired to study the micro-structural evolution of Mo films.

2.8 Atomic force microscopy

Atomic force microscopy is one of the most commonly used scanning probe microscope for the visualization of surface micro-topographies ranging from atomic structures to features extending to few tens of micrometers. The AFM works for both conducting as well as non-conducting samples and in this regard has an edge over scanning tunnelling microscope which only works on conducting samples. The operating principle of an AFM is depicted in Fig. 2.12. It illustrates the working principle of the laser beam deflection method. The paths of the laser beam both ‘directed onto’ and ‘reflected from (as a result of change of angle)’ the cantilever head changes as the cantilever bends. This deviation is detected by the position sensitive photodiode detector. The cantilever bends because of the force between the tip and the sample. This force, F, can be calculated using the following equation

$$F = k\,s \tag{2.11}$$

where ‘s’ is the distance by which the cantilever bends and ‘k’ is its spring constant.

It can operate in several modes [10]:

(a) Contact mode

In this mode, the tip is in mechanical contact with the sample surface. Typical force exerted on the sample surface by the tip ranges from ~ 0.1 μN to 1μN. In this mode, the repulsive part of the Van der Waals force from the surface balances the force applied predominantly on the tip by the bending cantilever. This mode is well suited for acquiring well resolved micro-topography of hard crystalline sample and surfaces, but not suitable for soft surfaces because of the associated elastic and plastic deformation.

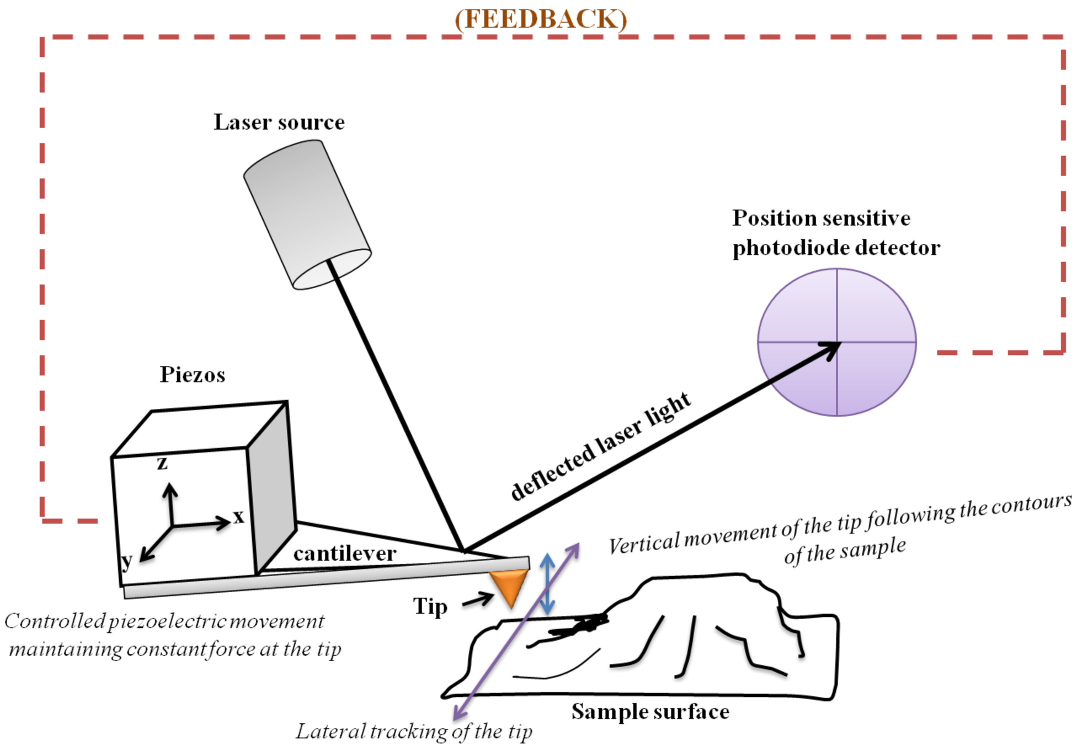

Fig. 2.12 *A schematic illustration of the working principle of an atomic force microscope.*

(b) Non-contact mode

In this mode, the cantilever oscillates close to its resonance frequency near the sample surface (5-10 nm) so that the force on the tip arises predominantly from the attractive part of the Van der Waals force field. The magnitude of force is very small ~ 1 pN. This mode is truly non-invasive and suitable for soft and biological samples. However, the resolution in non-contact mode is not as good as in contact mode.

(c) Tapping mode

In tapping mode, the cantilever oscillates at resonance frequency very close to the sample surface and the tip comes into contact with the sample's surface momentarily during each oscillation. Since it is a combination of both the contact and non-contact modes, it is sometime called semi-contact mode. The magnitude of vertical force on the tips in this mode remains same with that of contact mode; however with lesser interaction between the sample and the tip as a result of tapping, it enables one to scan soft surfaces with better resolution than non-contact mode. The lateral friction and drag forces present in the contact mode are also overcome in this mode.

In the thesis, AFM micro-topographic scans were exclusively performed in the tapping mode to study the surface topography of different as-deposited Mo films deposited under different deposition parameter. It was also used to study the topographic evolution of the SIMS crater in various Mo films. The acquired topographic micrographs were used to determine roughnesses of the surfaces. The roughness parameter used in the present thesis is the *de facto standard* root mean square (rms) roughness – the surface heights relative to least square fitted line profile and it is expressed as

$$R_q = \sqrt{\frac{1}{L}\int_0^L Z^2\,(x)dx} = \sqrt{\frac{1}{L}\sum_{i=1}^{N_L} Z_i^2\,(x)} \qquad (2.12)$$

2.9 Rapid thermal processor

Rapid thermal processor is an annealing set-up normally used in semiconductor device fabrication and microelectronics technology for flash heating of silicon wafers to high temperature (up to ~ 1200 °C). The heating duration is short ranging from few seconds to several minutes in contrast to conventional furnace annealing. Because of the rapid and short heating durations, it is used in many applications like dopant activation annealing in silicon wafers, annealing out defects introduced by ion irradiation, contact alloying or metallization in integrated circuits, crystallization, rapid thermal oxidation, nitridation and thermal diffusion. In the present thesis, I have made use of a Jipelec JetFisrt 100C for flash annealing as-deposited and ion irradiated Mo/Si thin film samples. The main component of a RTP is the cold-wall reactor chamber and the heating equipment - an array of 12 tubular infrared lamps heating a 4 inch Si wafer on which samples are placed. The unit is equipped with both K-type thermocouple and pyrometer for temperature measurement and the control is through a PID temperature controller. The reactor chamber can be pumped down to 1 x 10 $^{-3}$ mbar enabling vacuum annealing. There are two purge lines for performing annealing in different flowing gaseous ambient. The annealing cycle is executed through programmable logic controller (PLC) and PC interface with user defined recipes and parameters.

Fig. 2.13 *A Jipelec JetFirst 100C rapid thermal processor [11]*

2.10 Summary

In this chapter, details of all the experimental techniques which include techniques for thin film deposition, treatment and characterization, used for carrying out the work of the present thesis were discussed. The techniques are RF magnetron sputtering (PVD), SIMS, RBS, GIXRD, SEM, AFM, RTP and ion beam irradiation facility. The accelerators used for RBS and ion irradiation are also discussed.

References

---

1. R.F. Bunshah, *Handbook of deposition technologies for films and coatings*, Noyes Publication (1994) New Jersey
2. A. Benninghoven, F.G. Rüdenauer and H.W. Werner, *Secondary Ion Mass Spectrometry: Basic concepts, Instrumental Aspects, Applications and Trends*, Wiley, New York (1987) 1022-1028.
3. C. W. Magee and R.E. Honig, Surf. Interfcae Anal. 40 (1982) 35
4. K.E. Sickafus, E.A. Kotomin and B. P. Uberuaga, *Radiation effects in Solids*, Springer, (2004) 223 – 233.
5. D. Brune, R. Hellborg, H.J. Whitlow and O. Hunderi, *Surface Characterization: A User's Sourcebook*, Wiley-VCH, Weinheim (1997) 245
6. M. Mayer, SIMNRA user's guide. Tech. Rep. IPP 9/113, Max-Planck-Institut für Plasmaphysik, Garching (1997).
7. M. Birkholz, *Thin films analysis by X-ray scattering*, Wiley-VCH, Weinheim (2006) 143
8. U. Wezel, J. Ligot, P. Lamparter, A.C. Vermeulen and E. J. Mittemeijer, J. Appl. Cryst. 38 (2005) 1-29.
9. M. Nastasi and J. W. Mayer, *Radiation Effetcs in Solids*, Springer (2007) 387-400.
10. D. Brune, R. Hellborg, H.J. Whitlow and O. Hunderi, *Surface Characterization: A User's Sourcebook*, Wiley-VCH, Weinheim (1997) 79.
11. http://www.jipelec.com/products/index.htm.

CHAPTER 3

PHASE FORMATION IN THIN FILMS: A STUDY ON Ar^+ ION BEAM IRRADIATED Mo/Si THIN FILM

3. 1 Introduction

Phase formation in thin films and multilayer systems are quite intriguing as they often posses unique attribute in that they differ from their bulk synthesis. The presence of interfaces with high surface energy, defects and impurities makes it more complicated. Probably, the phenomenon of phase formation in binary thin film systems has been best investigated using various metal-silicon thin film systems and many studies on reactive phase evolution in binary metal-silicon thin film systems are well known for the past few decades [1]. Investigations on silicide systems have acquired importance not only due to their vast technological applications, but also because of their academic interest [2]. While it is possible to observe the co-existence of multiple silicide phases in bulk synthesis process, the phase formation in thin film binary systems is quite different. Usually, when two films in contact are heated, formation of only a single phase is observed [3]. Walser et.al, have predicted the first phase to nucleate in a number of metal-silicon binary systems to be the most stable congruently melting compound adjacent to the lowest-temperature eutectic on the bulk equilibrium phase diagram [4]. However, many experimental results show formation of different phases that deviate from their theoretical predictions. A number of controversial reports in this regard make it amply clear that the process of phase formation in thin film binary systems intricately depend on various parameters like diffusion, solid solubility, chemical reactivity, temperature and interfacial impurities. Hence there is always a technologically motivated need to perfect the understanding of the interfacial silicidation process.

In the present study, phase formation of molybdenum disilicide ($MoSi_2$) in ion beam irradiated Mo/Si thin films is investigated. The motivation for choosing $MoSi_2$ among other metal silicides in this work has been the suitability of $MoSi_2$ in a wide variety of technological applications and the absence of literature (to my knowledge) on formations of $MoSi_2$ through inert gas, particularly Ar^+ ion beam mixing (IBM). $MoSi_2$ is one of the many refractory transition metal silicides being investigated for possible replacement of poly-silicon gate in VLSI technology due to its low electrical resistivity, high chemical resistivity and thermal stability [5-6]. It is considered as a promising high temperature material for aerospace applications and is also being extensively investigated for use in multilayer based X-ray optics [7-8]. Conventionally, $MoSi_2$ is prepared by solid state reaction (SSR) of deposited molybdenum film over silicon, initiated by thermal reaction [9-10]. However, the SSR technique is reported to have several reproducibility issues and highly sensitive to the initial conditions and interfacial impurities. Moreover, the high temperature furnace anneals cause out-diffusion and redistribution of impurities and dopants. As such, ion beam synthesis, which generally is an athermal processes provides an alternate promising route for fabricating silicides. Ion beam process like implantation through metal (ITM) based on the direct dopant ion implantation into silicon through the metal enables silicidation as well as doping in a single implantation step. There are many such reports on the formation of $MoSi_2$ by ITM [4,11]. However, formation of $MoSi_2$ by inert gas ion beam mixing (IBM) are extremely rare or not quite reported in literature.The present work report the phase evolution of interfacial *t*-$MoSi_2$ ($C11_b$) [12] by IBM and post implantation flash annealing in a Rapid Thermal Processor (RTP). An investigation and discussion on the possible reasons for the co-existence and persistence of polymorphic phases even after high temperature anneals is also presented.

3.2 Sample preparation and experiments

3.2.1 Thin film deposition

Thin Mo film having thickness ~ 43 nm were sputter deposited on clean *n* – Si {100} substrate in a radio frequency (RF) magnetron sputtering system. at room temperature (RT). Argon was used as the sputter gas and a constant working pressure of 1.5×10^{-3} mbar was maintained during deposition. The sputter power used was 130 watt. The thickness of the film was determined from step height measurement of a masked portion of the Si substrate prior to film deposition using a surface stylus profilometer.

3.2.2 Ar^+ Ion beam irradiation

Ion irradiations were carried out on the as-deposited samples with Ar^+ ions at four different ion fluencies: (1) 7×10^{15} cm^{-2}; (2) 2×10^{16} cm^{-2}; (3) 7×10^{16} cm^{-2} and (4) 2×10^{17} cm^{-2}. The irradiations were performed in a 150 kV *J-15* gaseous ion accelerator with 110 keV Ar^+ ions at RT. The energy of the Ar^+ ions were chosen to be 110 KeV for maximizing atomic mixing at the interfacial region based upon the mean ion range (R_p) values calculated using TRIM code [13]. The mean ion range of 110 keV Ar^+ ions, R_p is ~ 45 nm in pure Mo target; while R_p is ~ 63 nm in Mo (43 nm)/Si bilayers from the TRIM calculation. The extended ion range R_p for Mo (43 nm)/Si bilayer target compared to the all-Mo target is attributed to the drastic decrease in stopping power of Si layer.

3.2.3 Other experimental details

The ion beam mixing (IBM) induced phase evolution was investigated by performing X-ray diffraction and Raman scattering measurements on the pristine, as irradiated and annealed samples. The X-ray diffraction experiments were performed on a STOE diffractometer in the Grazing Incidence X-ray Diffraction (GIXRD) geometry. The angle of incidence was 0.5 º. The Raman scattering experiments were performed using *514 nm* laser excitation in a Renishaw inVia Raman microscope. The as-implanted samples were flash annealed in a Rapid Thermal Processor (RTP) at 800 °C for a duration of 60 seconds. Secondary ion mass spectrometry (SIMS) was extensively used to study the interfacial composition, intermixing and diffusion, both before and after annealing. Rutherford backscattering spectrometry (RBS) was used qualitatively to complement the compositional studies of the post-annealed samples by SIMS. SIMS depth profile measurements were carried out using a CAMECA IMS-7f SIMS equipment. The depth profiles were carried out using Cs^+ primary ion beam. The measurement parameters used during the acquisition for impact energy, beam current, angle of incidence, raster size, analyzed area (optical gate) and mass resolution were 5 keV, 2 nA, 45º, 250 x 250 μm, 63 μm and 400 respectively. The species were sampled by detection of quasi-molecular Cs-complex ion viz., $(CsM)^+$, *where M is a metal*, to minimize matrix effect inherent to SIMS. RBS measurements were performed in a *Tandem* accelerator with 2 MeV He^+ ion beam. The backscattered particles were detected by a surface barrier detector kept at 165 º to the incident beam.

3.3 Experimental results

3.3.1 GIXRD and SIMS analyses

GIXRD measurements were performed on the pristine and as-irradiated samples for exploring IBM induced phase formation. Fig. 3.1a and Fig. 3.1b shows the GIXRD patterns for the as-deposited films and various as-irradiated samples respectively. The GIXRD peak patterns for the as-deposited films were found to be polycrystalline in nature as expected. The peak patterns for as-deposited Mo film were indexed to cubic-bcc structured polycrystalline Mo, and the pattern for both as-deposited and various as-irradiated Mo films matches well with the *JCPDS* card No. *421120*. There are no additional peaks indicating any phase formation. However, at high doses, only the (110) peak of Mo could be observed as all the other peaks have feeble intensities. Irradiation induced disorder in a crystalline solid, the magnitude of which in general depends on dose, is a well known phenomenon [14]. The suppression of the peak intensities in the various as-irradiated films is indicative of irradiation induced amorphization (Fig. 3.1b). The nature of the mixing and subsequent interfacial broadening can be understood from the SIMS depth profile. At low temperature ion irradiation, ballistic effects dominate and therefore, the mixing process is relatively temperature insensitive [5] and hence only mixed layer containing Mo and Si is generated. The SIMS depth profiles of Mo and Si for the samples irradiated to different ion doses are shown in Fig. 3.2a and Fig. 3.2b respectively. The Mo depth profiles show a systematic increase in mixing and diffusion of Mo into the Si matrix with the increase in the ion fluence. The Si depth profiles for the as-deposited sample shows a fairly sharp interface with the silicon signal climbing up sharply at the interface. With increasing fluence, the silicon front move towards the surface due to IBM and inter-diffusion which shows a trend sugge-

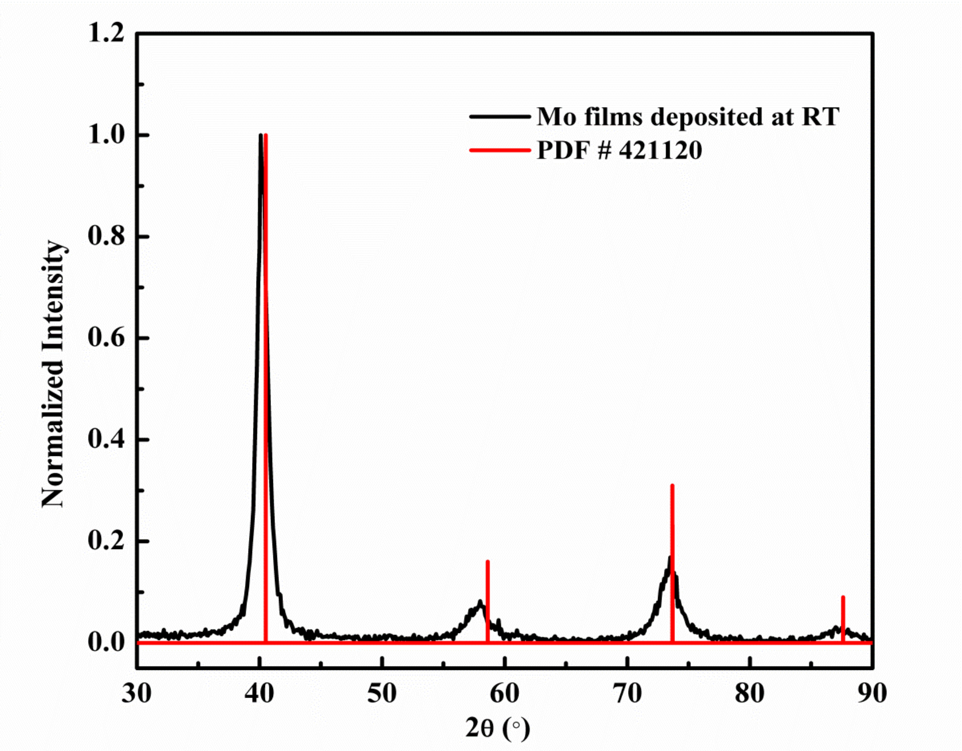

Fig. 3.1a *GIXRD peak patterns for the as-deposited Mo thin film.*

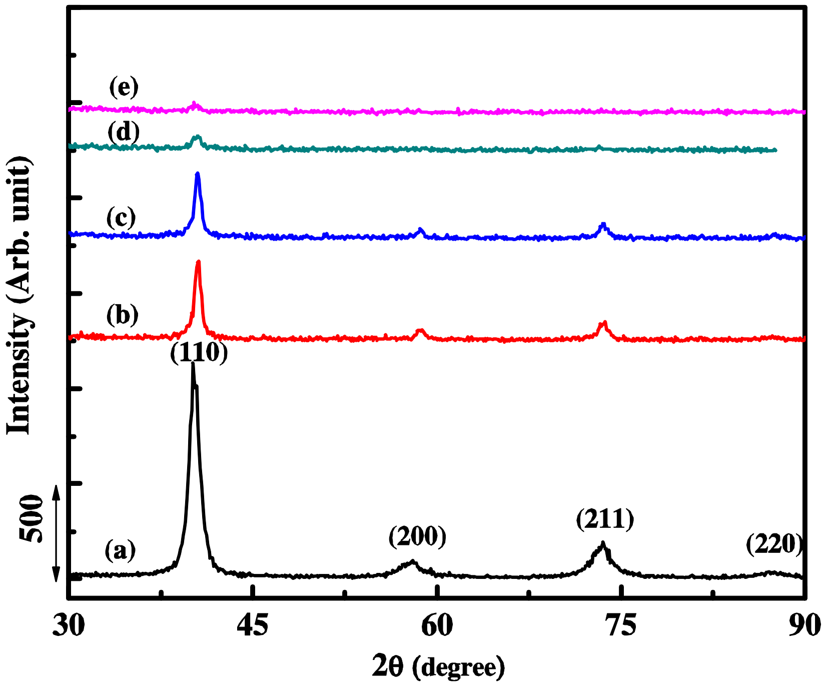

Fig. 3.1b *GIXRD patterns for (a) As-deposited Mo films, and those as-irradiated to doses (b) 7 x* 10^{15} *cm*$^{-2}$*; (c) 2 x* 10^{16} *cm*$^{-2}$*; (d) 7 x* 10^{16} *cm*$^{-2}$*; (e) 2 x* 10^{17} *cm*$^{-2}$*.*

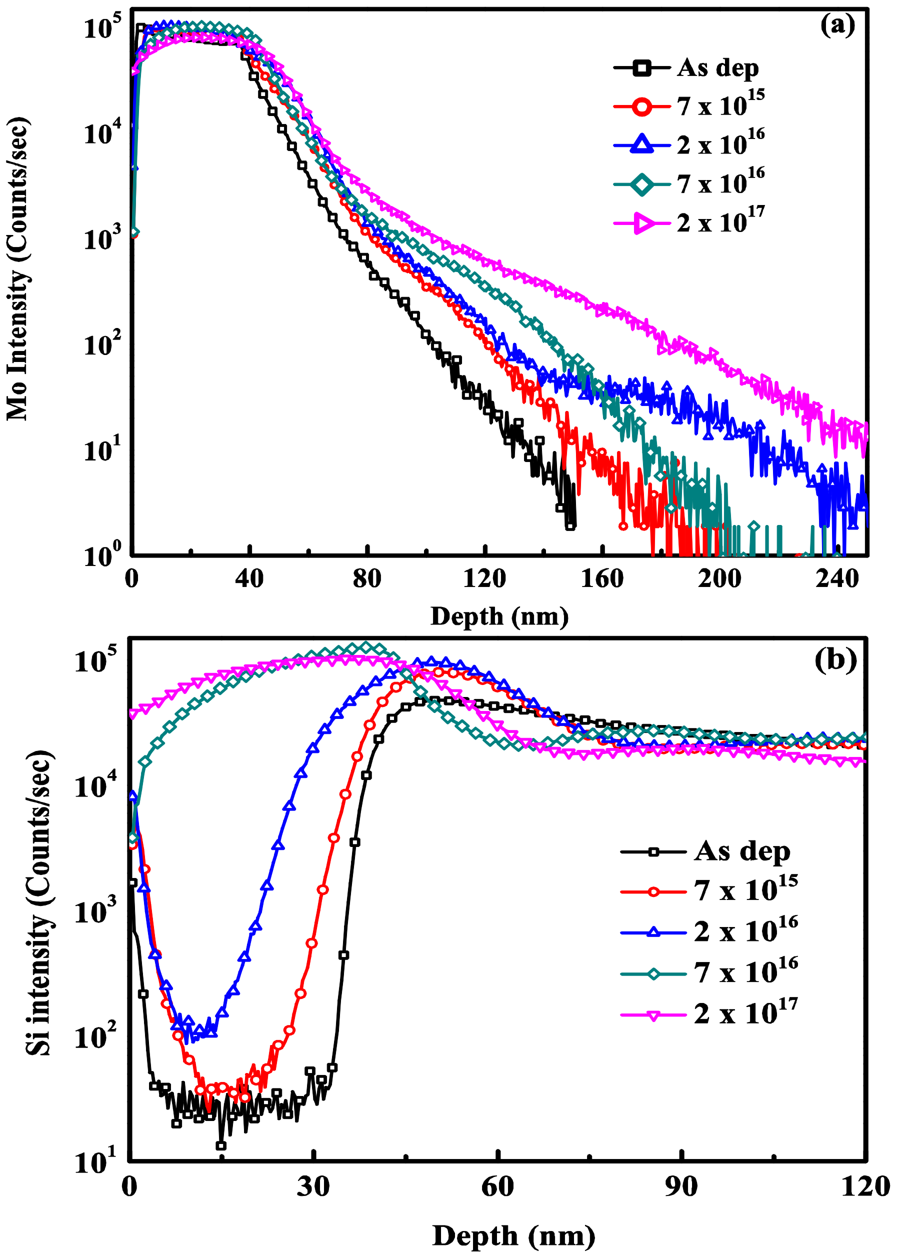

Fig. 3.2 *SIMS depth profiles of (a) Mo and (b) Si ; for as-deposited Mo films and those as-irradiated to doses:- 7 x 10* ^{15} *cm*$^{-2}$*, 2 x 10* ^{16} *cm*$^{-2}$*, 7 x 10* ^{16} *cm*$^{-2}$ *and 2 x 10* ^{17} *cm*$^{-2}$*.*

-stive of gradual mixing and diffusion into the Mo film up to a dose of 2 x 10 ^{16} cm^{-2}. Beyond this, the interfacial broadening increases substantially to an extent that Si could be detected at the surface which is indicative of complete mixing in this region yielding an amorphous layer composed of both Mo and Si. The nature and extent of mixing across the interface can be further examined from the oxygen depth profiles for the as-deposited and various as-irradiated samples which are displayed in Fig. 3.3. The initial high intensity of oxygen at the surfaces is attributed to the presence of adsorbed oxygen. Herein, the inherent native oxide layer present at the Mo-Si interface at a depth of ~ 43 nm can be treated as a marker owing to its typical thickness of about 2-3 nm. The evolution of the oxygen marker layer as a function of ion dose illustrates the extent of mixing. It is observe that no significant mixing takes place up to a dose of 2 x 10^{16} cm $^{-2}$ and that the disruption of the native oxide still remains incomplete. Hence, the corresponding radiation induced damage at this dose is only limited to partial amorphization of the Si substrate (Fig. 3.1b). However, when the dose is increased to 7 x 10^{16} cm^{-2}, significant mixing proceeds across the interface with the corresponding increase in amorphization of the Si substrate. This phenomenon is further evidenced for sample irradiated to 2 x 10^{17} cm $^{-2}$, where complete disruption of the native oxide and uniform dispersion of oxygen across the interface occurs. The resulting changes in the oxygen peak profile as a function of ion doses across the interface are shown as an inset in Fig. 3.3 for clarity. Herein, investigation performed with secondary ion imaging techniques on the sample irradiated to 2 x 10^{17} cm^{-2} reveals that local in-homogeneity exist in the ion beam mixed zone at the microscopic level. This result is presented later in appendix A. The Ar depth profiles for the as-deposited and the various as-irradiated samples are illustrated in Fig. 3.4. The as-deposited sample shows a negligible but finite amount of Ar contamination attributed to atomic peening during sputter deposition. The Ar depth profiles of all the as-irradiated samples exhibits two peaks, one main peak with distribution typical of an ion irradiation process having a maximum near the interface

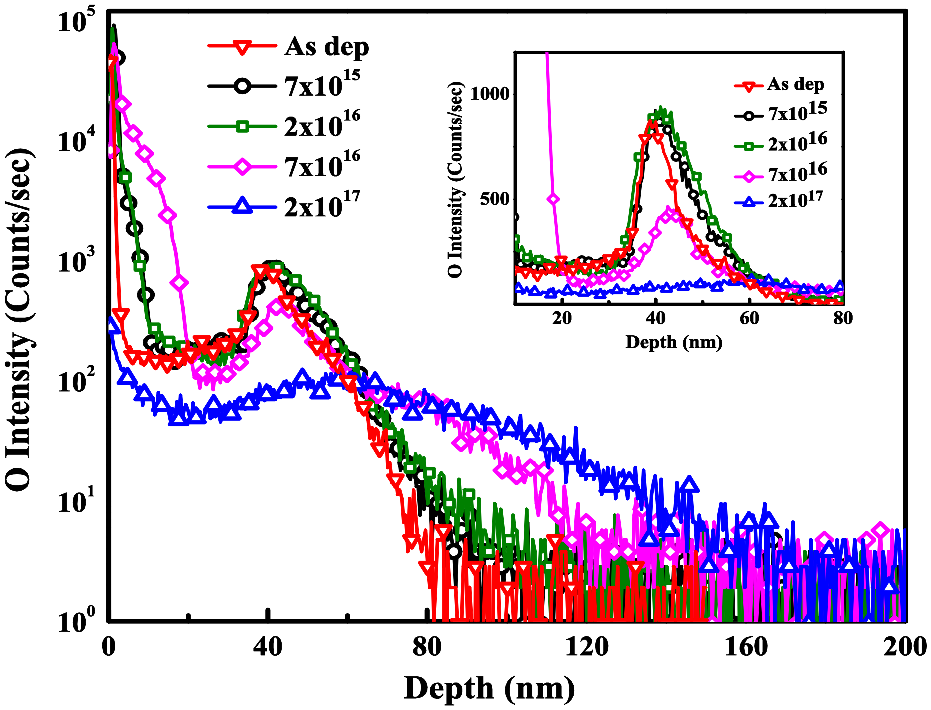

Fig. 3.3 *SIMS depth profiles of O for as-deposited Mo films and those as-irradiated to doses:- 7 x 10* ^{15} *cm*$^{-2}$*, 2 x 10* ^{16} *cm*$^{-2}$*, 7 x 10* ^{16} *cm*$^{-2}$ *and 2 x 10* ^{17} *cm*$^{-2}$*. Inset: O peak profile at the interface as a function of varying ion doses.*

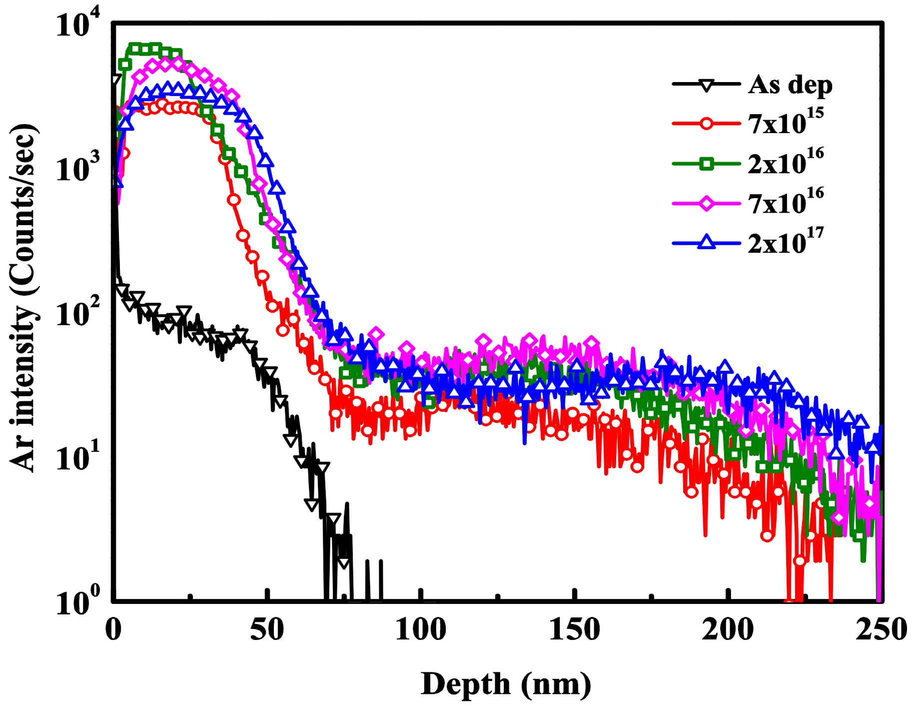

Fig. 3.4 *SIMS depth profiles of Ar for as-deposited Mo films and those as-irradiated to doses:- 7 x 10* ^{15} *cm*$^{-2}$*, 2 x 10* ^{16} *cm*$^{-2}$*, 7 x 10* ^{16} *cm*$^{-2}$ *and 2 x 10* ^{17} *cm*$^{-2}$*.*

and a smaller broad peak superposed on the straggling end of the first distribution. The latter one is located well inside the Si substrate. However, the peak position of the second broad peak shifts deeper into the silicon substrate with increasing ion fluence. This can be attributed to the consequent reduction in the thickness of Mo film due to the increase in surface sputtering with the ion dose. The reduction in energy loss of the ions inside the Mo film subsequently increases the incoming energy and hence the range of the Ar^+ ions into the silicon substrate across the interface. The implanted Ar^+ ions are relatively immobile and it results in an increasing Ar concentration in the matrix. Since noble gases have a tendency to diffuse by a vacancy assisted mechanism, trapping of the gaseous atoms by bombardment-induced vacancies could also result in formation of very small bubbles in the form of inert gas vacancy clusters. However, the predicted volume fraction of these small bubbles is expected to be less than 2 vol% as estimated for similar studies elsewhere [15]. A comparison of these results with the diffraction data suggests that although substantial mixing at the interface takes place at higher doses, there is no characteristic peak indicative of formation of crystalline molybdenum silicide. This could be possible if the silicide formation is below the detectable volume accessible to GIXRD technique (i.e. less than 5% of the volume at the surface). To identify and confirm the presence of miniscule fraction of silicide phase entrained in the matrix, raman spectral measurements were carried out and is discussed in the next section.

3.3.2 Raman and GIXRD analyses upon RTP annealing

The spectra of the irradiated samples do not show any indication of silicide formation even for the sample with highest dose Fig. 3.5a. This corroborates the results of the GIXRD measurements on the various irradiated samples. Subsequently, the samples were flash vacuum annealed at 800 ºC for 60 secs in a RTP. Although the

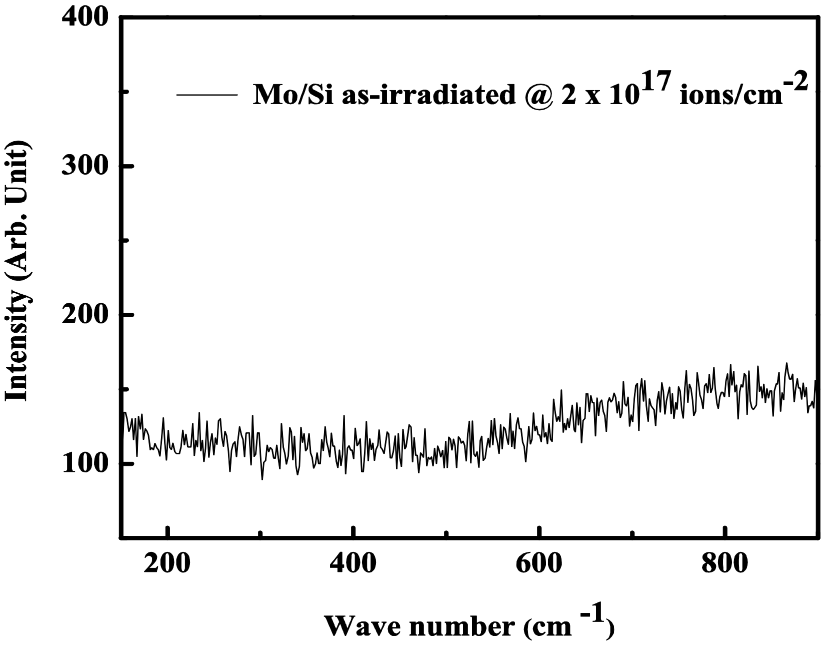

Fig. 3.5a *Raman spectra for the sample as-irradiated to a dose of 2 x 10* ^{17} *cm*$^{-2}$*.*

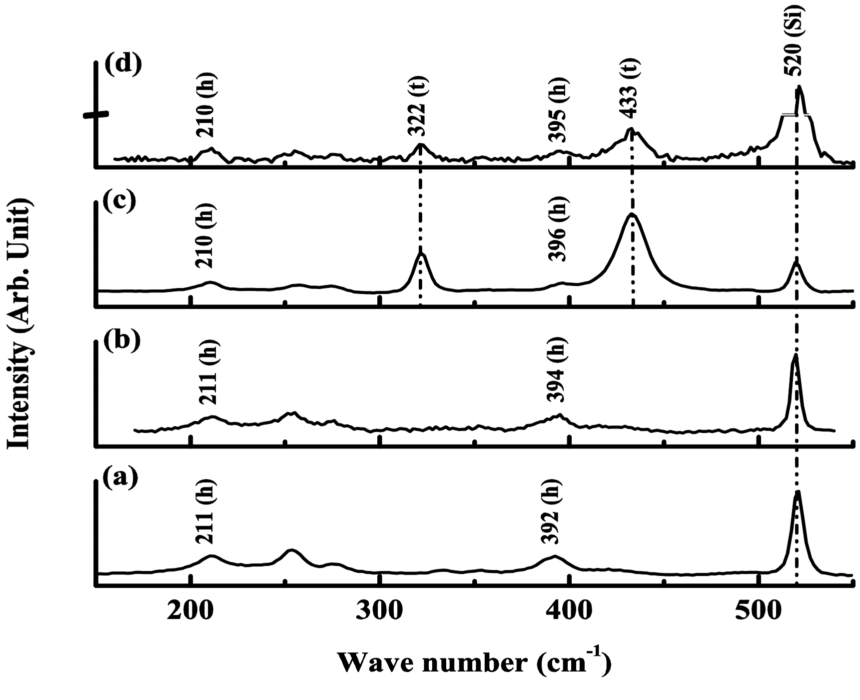

Fig. 3.5b *Raman spectra of the samples annealed at 800 ºC in a RTP unit, after being subjected to irradiation at various doses :- (a) 7 x 10* ^{15} *cm*$^{-2}$*; (b) 2 x 10* ^{16} *cm*$^{-2}$*; (c) 7 x 10* ^{16} *cm*$^{-2}$*; (d) 2 x 10* ^{17} *cm*$^{-2}$*.*

structures of *t*-$MoSi_2$ ($C11_b$) and *h*-$MoSi_2$ (C40) [12] are locally similar, they have different symmetries resulting in strikingly different Raman spectra. Raman spectral analysis of the annealed samples reveals that for ion doses below 2 x 10^{16} cm^{-2}, only lines corresponding to hexagonal or *h* - $MoSi_2$ are observed. The bands corresponding to *t*- $MoSi_2$ appeared only for ion doses 7 x 10^{16} cm^{-2} and above as shown in Fig. 3.5b. Using group theory, Doland et.al [16], had predicted two Raman active modes, an A_{1g} mode and a degenerate E_g mode for *t*- $MoSi_2$ while nine Raman active modes, one A_1 mode, four degenerate E_1 mode and four degenerate E_2 mode had been predicted for *h*- $MoSi_2$. Experimentally they observed strong peaks at 325 and 440 cm^{-1} for bulk *t*- $MoSi_2$. They had measured strong peaks near 210, 260, 395, and 420 cm^{-1} and some weak features between 260 and 395 cm^{-1} for *h*- $MoSi_2$. Apart from this, Srinivas et. al., [17] have observed lines at 322 and 434 cm^{-1} for Si rich film annealed at 1150 °C for 30 sec. In the present study, strong *t*- $MoSi_2$ peaks at 322 and 433 cm^{-1} were observed for ion doses above 7 x 10^{16} cm^{-2}, whereas no *t*- $MoSi_2$ peaks could be detected for doses lower than 7 x 10^{16} cm^{-2} suggesting that the ion fluence has a key role to play in the formation of the stable silicide phase. However, the persistence of peaks pertaining to *h* - $MoSi_2$ near 210 and 395 cm^{-1} were observed even for the samples irradiated to a dose of 7 x 10^{16} cm^{-2} and above. The characteristic Raman peak for crystalline Si at 520 cm^{-1} is also shown as a reference. From these observations, it is clear that the stable *t* - $MoSi_2$ silicide phase forms only at higher doses.

The GIXRD pattern for the RTP annealed samples are shown in Fig. 3.6a and 3.6b. It is observed that samples irradiated to ion dose of 7 x 10^{16} cm^{-2} and below shows peaks pertaining to *h* - $MoSi_2$ only, while samples irradiated to a dose of 7 x 10^{16} cm^{-2} and above show GIXRD peaks pertaining to *t* - $MoSi_2$ in addition to the *h* -

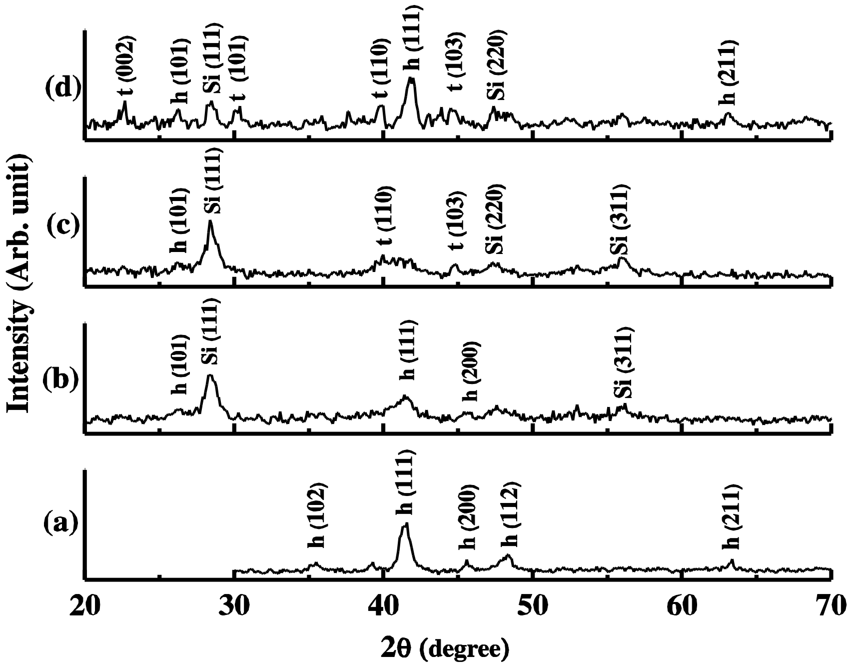

Fig. 3.6a *GIXRD pattern for the samples annealed at 800 ºC in a RTP unit, after being subjected to irradiation at various doses :- (a) 7 x 10* ^{15} *cm*$^{-2}$*; (b) 2 x 10* ^{16} *cm*$^{-2}$*; (c) 7 x 10* ^{16} *cm*$^{-2}$*; (d) 2 x 10* ^{17} *cm*$^{-2}$*.*

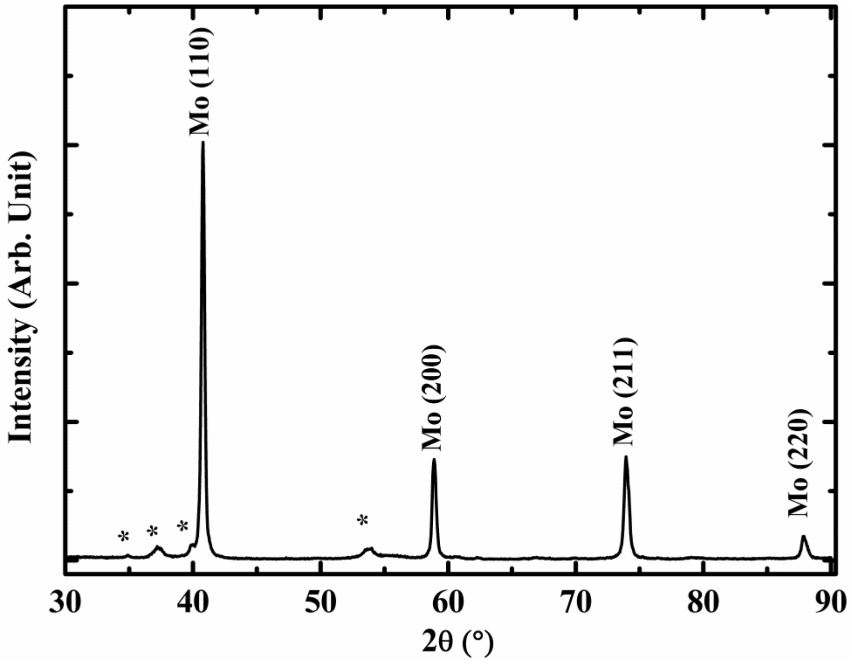

Fig. 3.6b *GIXRD pattern of the as-deposited sample annealed at 800 ºC in a RTP without any ion irradiation. Peaks mark * represent oxide phases of Mo.*

$MoSi_2$ peaks (Fig. 3.6a). The as-deposited films subjected to the same flash annealing condition (800 °C for 60 secs) without ion irradiation shows no silicide phase formation. It only shows enhancement in crystallinity of the bcc structured polycrystalline Mo film and few peaks pertaining to partial oxidation of the Mo films. This highlights the crucial role played by the native oxide on the interface between Mo/Si as an effective barrier to any diffusive phase formation of silicides. Ion beam irradiation as such, disrupts this native oxide and initiates atomic level mixing of Mo and Si thereupon aiding formation of silicides on flash annealing. As can be seen, the GIXRD results for the RTP annealed samples corroborate well with the results from Raman analysis of the annealed samples. Hence, it is concluded that h - $MoSi_2$ and t - $MoSi_2$ phases co-exist at higher irradiation doses.

3.3.3 RBS and SIMS analyses of the annealed samples

The composition of the interface upon IBM and subsequent flash annealing is studied by means of RBS. Fig. 3.7 shows the RBS spectra for the as-deposited and the annealed samples irradiated to a fluence of 2×10^{17} cm^{-2}. The RBS spectra for the as-deposited sample exhibit a fairly sharp interface and there is no indication of phase formation or interface broadening. However, sample irradiated and annealed at 800 °C shows a shift in the leading Si edge towards higher energy channels and the inflection in silicon edge shows the possible formation of the silicide phase (Fig. 3.7). The loss in Mo yield for the irradiated samples is attributed to surface sputtering of the Mo films which increases with ion dose. The experimental data were fitted to a computer simulation using SIMNRA code [18]. The as-deposited sample was fitted to a simple Mo/Si bilayer model, whereas the annealed sample irradiated to a fluence of 2×10^{17} cm^{-2} was fitted to an 11 layer model.

Depth profiles constructed from the simulation are shown in Fig. 3.7 as an inset. The stoichiometric ratio for $MoSi_2$ exists only within the top film up to a depth of ~ 20 nm, after which presence of Si concentration in excess to what is required for the stoichiometric ratio is observed. The Mo concentration in the reacted zone starts declining near the interface and ultimately falls off to zero at a depth of ~ 100 nm.

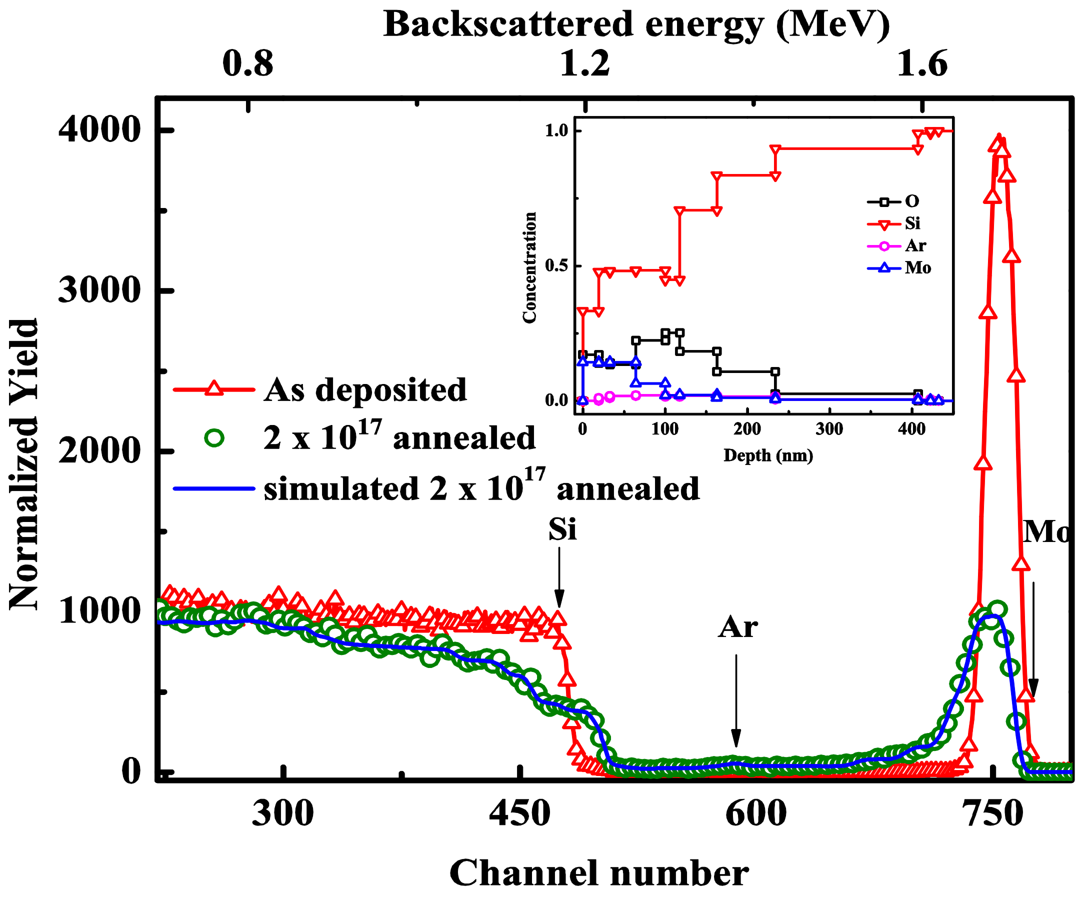

Fig. 3.7 *RBS spectra for as deposited Mo films, Mo silicides formed upon annealing of the sample subjected to ion beam mixing at a dose of 2 x* 10^{17} cm^{-2} *and simulated spectra. Inset: Concentration profile of Mo, Si, O and Ar from the simulation.*

The composition is best described as a graded one, rather than a uniform one. Such a graded nature is also seen in the oxygen profile. Herein, a snow ploughing of oxygen similar to those reported in other studies is observed [19]. Moreover, the snow

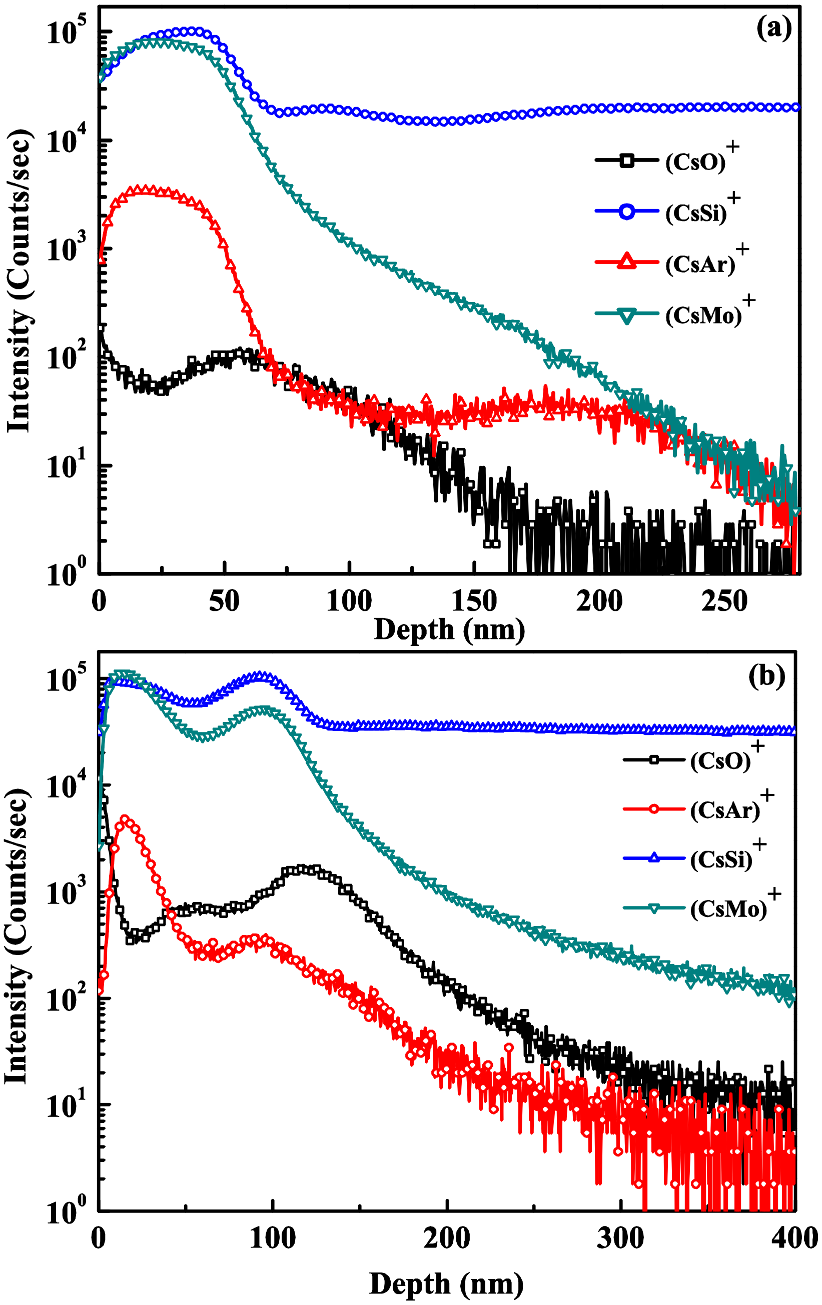

Fig. 3.8 *SIMS depth profiles for the sample irradiated to 2 x* 10^{17} *cm*$^{-2}$ *:- (a) As-irradiated before annealing and (b) After flash annealing in an RTA chamber at 800 ºC for 60 seconds .*

ploughing effect which looks partial is towards the interface as indicated by the broad peak near the interface in the substrate. The snow ploughing and the related phenomena are further complemented by the SIMS depth profiles analysis given in

Fig. 3.8a and 8b, which shows profiles of irradiated sample before and after flash annealing.

Comparison of the oxygen profiles before and after annealing clearly shows the snow ploughing of the oxygen towards the interface seen by the peak shifting towards the interface for the annealed samples. In addition, one can notice a small amount of oxygen ingress probably creeping in during annealing and sample handling. The implanted Ar^+ ion species in the matrix have diffused towards the interface and are dispersed over a wide range. However, the Ar ions in the first 20 – 40 nm have not diffused significantly. Mo signal too, have diffused to a significant depth, however bulk of them are confined to a depth a little over 100 nm.

3.4 Discussion

This chapter present a systematic study on the phase evolution in Mo/Si system irradiated to various Ar^+ ion doses and flash annealed at 800 ºC for 60 sec. Micro-structural characterization with GIXRD and Raman spectral analyses of the RTP annealed samples show formation of metastable *h*-$MoSi_2$ alone for samples irradiated to lower doses and that of stable *t*-$MoSi_2$ for samples irradiated to higher doses. However, the presence of *h*-$MoSi_2$ can be found in all the annealed samples including the ones irradiated to higher doses. This is quite in contrast to the conventional solid state reaction where all the samples are supposed to have resulted in the formation of $MoSi_2$ when annealed at 800 °C [17]. This aspect is further discussed in the following paragraph.

IBM at the interface leads to formation of Mo-Si amorphous compound and provides nucleation sites for the crystalline silicide phase to form. Hence, the stoichiometry of interface layer is an important aspect which determines the phase corresponding to the composition under thermal treatment. Thereupon, formation of a new phase at the interface is controlled by the existence of a temperature dependent critical size embryos (characterized by radius r) having equal chance for shrinking or growing. Below certain critical size, the embryos of the new phase are generally unstable. The embryos larger than a critical radius 'r_c' have a tendency to grow because at large 'r', the gain in volume free energy dominates over the energy loss. This stable volume of the new phase is called the nucleus and the process by which stable nuclei are produced is commonly known as nucleation. Growth of a stable nucleus takes place when atoms are transported to the growing nuclei by diffusion. Consequently, the rate of phase transformation is very sensitive to temperature [20]. The nucleation and growth of both t - $MoSi_2$ and h - $MoSi_2$ phases occur at the present annealing temperature. However, the formation of only h - $MoSi_2$ at lower doses indicates that the composition of the species and the extent of intermixing at the interface depends on the fluence and dominate the nucleation process. While the concentration gradient of the constituent species are established by RBS and SIMS, the nucleation of h - $MoSi_2$ at lower doses and t - $MoSi_2$ for higher doses upon annealing as elucidated by both GIXRD and Raman spectra is rather unique. This clearly shows that the extent of mixing and the resultant atomic ratio arising from the atomistic shuffling of Mo and Si in the amorphous zone have an impact in determining the nucleation. In many cases, bulk thermodynamics is inadequate to explain the initial interactions in thin films. The effects of impurities, nucleation and growth kinetics are important issues in the initial phases of thin film solid state reactions. Generally, metals and silicon react when the chemical free energy is larger than the activation energy for nucleation. Subsequently nucleation is rather easy and rapid so that it is possible to isolate it and observe experimentally. In the present case, the bulk free energy of *t* - $MoSi_2$ must be larger than the bulk free energy of *h* - $MoSi_2$, since *t* - $MoSi_2$ is the stable phase in bulk. However, if the interfacial energy at the silicide/silicon interface is lower for *h* - $MoSi_2$ than *t* - $MoSi_2$, the free energy of the cluster formation may depend on cluster size. If ΔG is the energy barrier and *r* is the critical radius for the nucleation of *t* - $MoSi_2$, the lower surface free energy of *h* - $MoSi_2$ result in a lower nucleation barrier ΔG' and smaller critical radius r' for *h* - $MoSi_2$ [16]. Indeed such abrupt crystallization is observed to occur in the amorphized interfacial region where it crosses a threshold thickness of 2 nm [21]. Eventually, presence of any impurities at the interface will affect the silicidation process and act as a nucleation barrier.

In the present study, apart from the intentional Ar^+ implantation for interface mixing, a certain amount of unintentional oxygen impurities is picked up during annealing process as observed in RBS and SIMS concentration profile of Fig. 3.7 and Fig. 3.8 respectively. However, the influencing effects of oxygen impurities in the present study is ruled out on the basis of the XRD results which shows an absence of any metal rich silicides like Mo_5Si_3 and Mo_3Si that should have resulted if the oxygen impurity is substantial [22]. Hence, we attribute the co-existence of the polymorphic phases which persists even after high temperature annealing to the presence of Ar bubbles that could act as a nucleation barrier and hinder the transport of the constituent atoms by diffusion. Such Ar bubble formation is also evidenced in Ti/Si system [23]. Hence, the simultaneous nucleation of *h*-$MoSi_2$ and *t*-$MoSi_2$ could possibly be due to rapid crystallization at the interface as ion beam synthesis is well known to produce systems far from thermodynamic equilibrium. In such cases, conversion of metastable phase into the stable phase during annealing could be possibly hampered by the presence of Ar which restricts the atomic transport needed for the formation of stable *t*-$MoSi_2$ phase.

3.5 Conclusion

In conclusion, IBM with Ar^+ ion on a Mo/Si bilayer system leads to mixing at the interface with a graded elemental concentration. Subsequent RTP annealing of this ion beam mixed samples results in the formation of the polymorphic silicide phases. RTP annealing of the as-deposited samples without any irradiation shows no silicide phase formation. Samples irradiated with lower doses exhibit formation of metastable *h* - $MoSi_2$, whereas samples with higher doses shows formation of stable *t* - $MoSi_2$ in addition to *h* - $MoSi_2$. The co-existence of the polymorphic phases at higher doses is attributed to the presence of Ar in the matrix as impurity which hinders the structural transformation of *h* - $MoSi_2$ into *t* - $MoSi_2$.

References

1. R. Pretorius, A. M. Vredenberg, F. W. Saris, R. de Reus, *J. Appl. Phys.* 70 (1991) 3636
2. G. Ottaviani, F. Nava, G. Queirolo, G. Iannuzzi, G. De Santi, K. N. Tu, *Thin Solid Films* 146 (1987) 201.
3. E. G. Colgan, F. M. d'Heurle, *J. Appl. Phys*. 79 (1996) 4087.
4. R. M. Walser, R. W. Bene, *Appl. Phys. Lett*. 28 (1976) 624.
5. G. VALYI, H. Ryssel, W. Moller, *Nucl. Instr. And Methds. In Phys. Research B* 39 (1989) 268.
6. A. Zambova, I. Nedev, *Vacuum* 43 (1992) 223.
7. J. M. Slaughter, A. Shapiro, P. A. Kearney, C. M. Falco, *Physical Review B* 44 (1991) 3854.
8. I. Nedelcu, R. W. E. van de Kruijs, A. E. Yakshin, F. Bijkerk, *Physical Review B* 76 (2007) 245404.
9. M. A. Nicolet, S.S. Lau, *VLSI Electronics 6, ed., N.G. Einspruch*, Academic Press, New York, (1983) 330-459.
10. R. S. Rastogi, V. D. Vankar, K. L. Chopra, *Thin Solid Films* 164 (1988) 449.
11. T. Gessner, R. Reich, W. Unger, W. Wolke, *Thin Solid Films* 177 (1989) 225.
12. L. F. Mattheiss, *Physical Review B* 45 (1992) 3252.
13. TRIM calculation, http://www.srim.org/
14. P. M. Ossi, *Material Science and Engineering* 90 (1987) 55.
15. S. Amirthapandian, B. K. Panigrahi, A. K. Srivasta, A. Gupta, K.G. M. Nair, R. V. Nandedkar, A. Narayanasamy, *J. Phys. Condens. Matter* 14 (2002) L641.
16. C. M. Doland, R. J. Nemanich, *Journal of Materials Research* 5 (1990) 2854.
17. G. Srinivas, V. D. Vankar, *Materials Letters* 30 (1997) 209.

18. M. Mayer, SIMNRA user's guide. Tech. Rep. IPP 9/113, Max-Planck-Institut für Plasmaphysik, Garching (1997).
19. A. H. Van Ommen, M. F. C. Willemsen, R. A. M. Wolters, *Nucl. Instr. And Methds. In Phys. Research B* 19-20 (1987) 742.
20. J. Burke, *The kinetics of phase transformations in metals*, Pergamon Press, London (1965).
21. C. Johnson, K. Anderson, A. Gromko, D. Johnson, *J. Am. Chem. Soc.* 1998 ; *120* , 5226.
22. F. Nava, G. Majni, P. Cantoni, G. Pignatel, G. Ferla. P. Capelletti, F. Mori, *Thin Solid Films* 1982 ; *94* , 59.
23. G. Ottaviani, R. Tonini, D. Giubertoni, A. Sabbadini, T. Marangon, G. Queirolo, F. La Via, *Microelec. Eng.* 2000 ; *50* , 153.

CHAPTER 4

RESIDUAL STRESS IN Mo THIN FILMS USING X-RAY DIFFRACTION

---

4. 1 Introduction

Vast majority of important technological applications of thin films are in their polycrystalline form. Polycrystalline metal thin films are used in wide range of applications like VLSI and ULSI metallization and protective coatings. However, all common thin film deposition techniques utilize vacuum deposition processes. These deposition processes inherently introduce residual stress in the deposited thin films that merit investigation [1]. This stored mechanical stress can have deleterious effects on the film-substrate system. It can either cause cracking of the film in case of tensile stress ‘or’ buckling in case of a compressive stress [2]. It also plays an important role in the evolution microstructure and thus affects the mechanical and other associated properties of the film like for example, change in superconducting transition temperature T_c of Mo films with residual stress [3]. As such, evaluation of residual stress in vacuum deposited polycrystalline metal thin films is technologically important from both application and the related deposition process optimization point of view and as well as for understanding the nature of thin film growth characteristics. Among the two commonly used non-destructive techniques, residual stress analysis using X-ray diffraction has found wide acceptance as it allows the determination of complete stress tensor for all crystallite phases present and can also provide other additional information like texture and crystallite size [4]. The other method is substrate curvature measurement method based on Stoney's formalism [5]. However, the classical $\sin^2\psi$ method (d *Vs* $\sin^2\psi$) for stress analysis which relies on the measurement of peak shifts of a high angle reflection as a function of specimen tilt 'ψ' often fails when applied to thin films [6], the limiting factors being the thickness of films and the occurrence of crystallographic texture. The highly penetrating symmetric Bragg Brentano (BB) geometry used in the $\sin^2\psi$ method and the resulting low diffraction volume therein result in a signal too weak to be measurable with good peak to noise ratio. The elastic anisotropy introduced due to texture often limits the number of measurable reflections at high angle [7-8]. Hence, an asymmetric geometry employing low grazing incidence is generally used for the residual stress analysis of thin film specimens, because of its inherent advantage in limiting the penetration of X-ray beam and maximizing the diffraction volume within the films. Indeed, several authors have proposed and employed different modified $\sin^2\psi$ methods using a small fixed grazing incidence either in the Seemann-Bohlin (SB) or GIXRD geometry [9-10] for thin films. These modifications are possible when assumptions with regard to lattice symmetry, elastic properties and stress state are considered[11]. While some authors measure the peak shift of a single reflection, some of them combines the peak shifts from multiple reflections to find out the stress [4,7,12]. But both or all the approaches are same in a way because stress is calculated from the slope of a straight line fitting obtained through a linear regression of some function of the inter-planar spacing *d* and the specimen tilt angle *'ψ'* as in the traditional $\sin^2\psi$ method. A comparison is given in most cases. It is also noteworthy to mention that while a multiple *hkl* method gives a stress value averaged over all crystallographic planes, a single *hkl* method provides stress for a selected family of planes. These two values can differ.

In this chapter, the effect of substrate temperature (T_s) on the in-plane biaxial residual stress in polycrystalline Mo thin films is investigated. The residual stresses are estimated using both multi *hkl* reflection peak shifts as well as single *hkl* reflection peak shift methods in a parallel beam geometry. These estimates were used to study the evolution of residual stress as a function of T_s and the results are compared. The deposited films exhibit a compressive stress at low deposition temperature which reverses to a tensile one at high deposition temperature. The origin and evolution of the residual stress as a function of T_s is elucidated in this chapter.

4.2 Mathematical Formalism

Hooke's law relating the stress to the strain forms the basis of X-ray stress analysis in materials. Hooke's law in its generalized form [13] is given by

$$\varepsilon_{ij} = \frac{1+\nu}{E}\sigma_{ij} - \delta_{ij}\frac{\nu}{E}\sum_{k}\sigma_{kk} \tag{4.1}$$

where ε_{ij} *and* σ_{ij} are the ijth component of the strain and stress tensors, respectively; E and ν represent elastic modulus and Poisson ratio, respectively.

Experimentally, X-ray stress analysis relies upon the measurement of strain induced in the lattice by the residual stress. The direction of the measured strain is defined by the rotation of the azimuth angle ϕ and inclination of the specimen tilt angle ψ, respectively, in a laboratory frame of reference. The lattice spacing d^{hkl} is related to the diffraction angle $2\theta^{hkl}$ by Bragg's law

$$2d^{hkl}\sin\theta^{hkl} = \lambda \tag{4.2}$$

where λ is the wavelength of the X-ray used.

The strain is then given by

$$\varepsilon_{\phi\psi}^{hkl} = \frac{d^{hkl} - d_0^{hkl}}{d_0^{hkl}} \tag{4.3}$$

where d_0^{hkl} is the strain free lattice spacing of the *hkl* lattice planes. Stress is then derived from the measured strain by inserting a reliable proportionality constant. Fig. 4.1 (a) shows the relation between laboratory and specimen frames of references and Fig. 4.1(b) shows the various angles with their axes.

The strain tensor in the laboratory frame is related to the strain in the specimen reference frame by a tensor transformation which is given by

$$\varepsilon_{\phi\psi}^{hkl} = \varepsilon_{33}^{L} = m_i^s \varepsilon_{ij}^s m_j^s \tag{4.4}$$

$$\text{where } \boldsymbol{m}^s = \begin{pmatrix} \sin\Psi\cos\phi \\ \sin\Psi\sin\phi \\ \cos\Psi \end{pmatrix} \tag{4.5}$$

is a unit vector along the direction of diffraction vector as expressed in the specimen frame of reference.

Upon substituting the equation (4.1) into equation (4.3), the fundamental equation for X-ray stress analysis is obtained as:-

$$\begin{aligned} \varepsilon_{\phi\psi}^{\mathrm{hkl}} = \frac{1}{2}\mathrm{S}_2[(\sigma_{11}^{\mathrm{s}}\ \cos^2\phi + \sigma_{22}^{\mathrm{s}}\sin^2\phi + \sigma_{12}^{\mathrm{s}}\sin 2\phi)\sin^2\Psi \\ + (\sigma_{13}^{\mathrm{s}}\cos\phi + \sigma_{23}^{\mathrm{s}}\sin\phi)\sin 2\psi + \sigma_{33}^{\mathrm{s}}\cos^2\Psi] \\ + \mathrm{S}_1(\sigma_{11}^{\mathrm{s}} + \sigma_{22}^{\mathrm{s}} + \sigma_{33}^{\mathrm{s}}) \end{aligned} \tag{4.6}$$

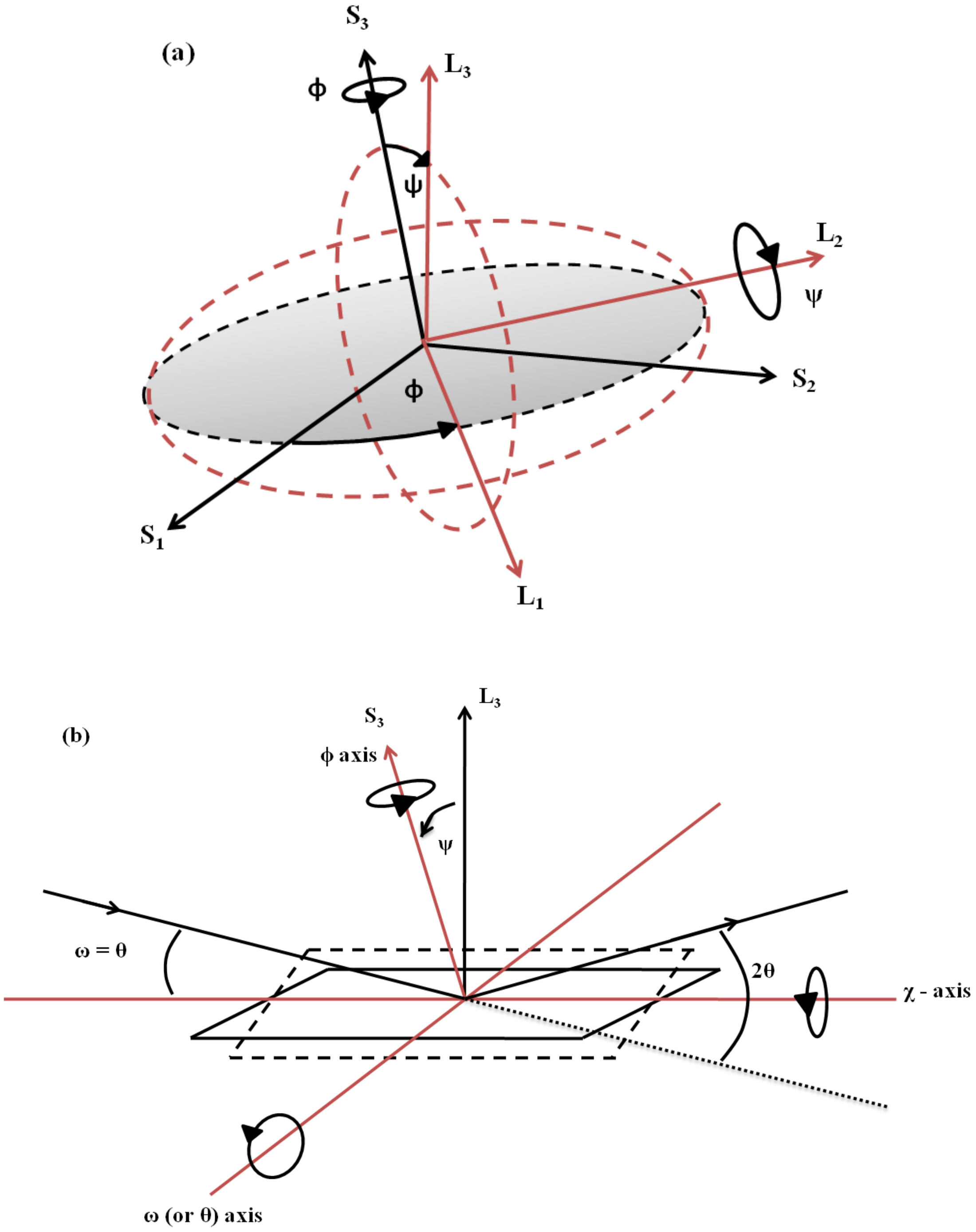

***Fig. 4.1** (a) Relation between the specimen (S) and the laboratory (L) reference frames; (b) the ω, ϕ and χ axes that describe the orientation of the specimen with respect to the laboratory frame of reference.*

where S_1 and $\frac{1}{2}S_2$ are the elastic constants of the material. For isotropic materials, these are related to *E* and *ν* of the material by the following relations

$$S_1 = -\frac{\nu}{E} \tag{4.7}$$

and

$$\frac{1}{2}S_2 = \frac{(1+\nu)}{E} \tag{4.8}$$

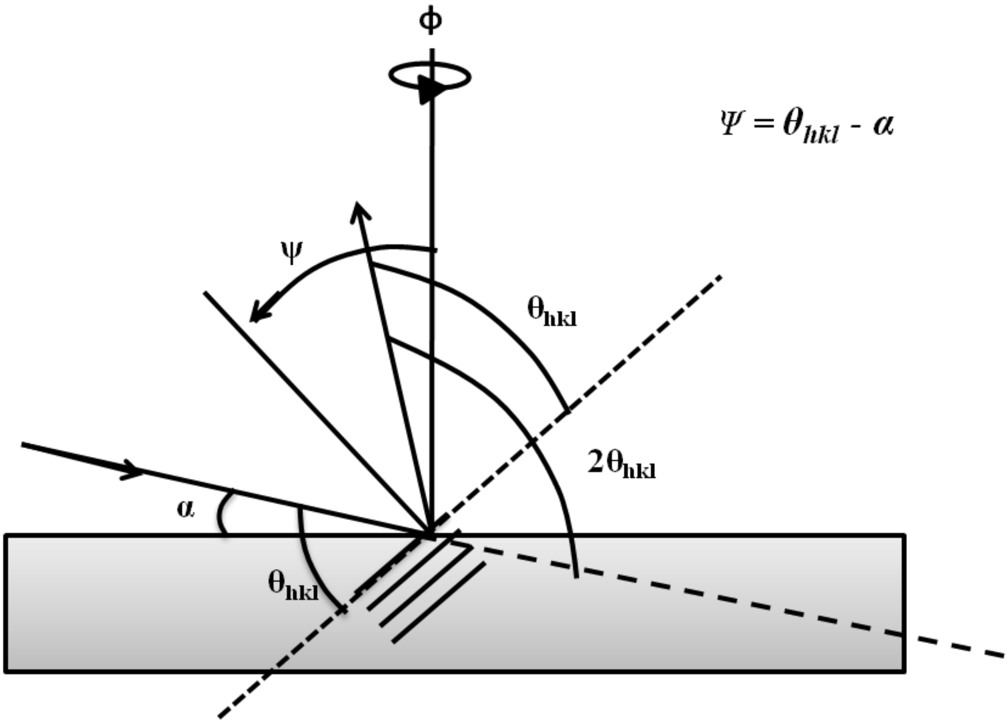

Fig. 4.2 (a) Relation between the specimen tilt angle Ψ, the incident angle α and the Bragg angle θ_{hkl} for a set of {hkl} planes in the asymmetric diffraction geometry.

In the biaxial stress model, all off diagonal components of the stress tensor vanish along with the out-of-plane component (i.e.$\sigma_{33}^{s} = 0$) and the only non vanishing components are the in-plane component $\sigma_{11}^{s} = \sigma_{22}^{s} = \sigma_{\parallel}$ such that the stress tensor transform to

$$\sigma_{ij}^{S} = \begin{pmatrix} \sigma_{\parallel} & 0 & 0 \\ 0 & \sigma_{\parallel} & 0 \\ 0 & 0 & 0 \end{pmatrix} \tag{4.9}$$

Considering the specimen to have rotational symmetry, the fundamental equation (4.6) reduces to

$$\varepsilon_{\Psi} = \frac{1+\nu}{E}\sigma_{\parallel}\sin^2\Psi - \frac{2\nu}{E}\sigma_{\parallel} \tag{4.10}$$

This is the well known classical $\sin^2\psi$ formalism

4.3 Sample preparation and experiments

4.3.1 Thin film deposition

For the present study, polycrystalline Mo thin films were sputter deposited onto clean *p*-Si (111) substrates from a pure 2” Mo target using a radio frequency magnetron sputtering unit. The substrate temperature T_s was systematically varied from room temperature (RT) to 800 °C in steps of 100 °C. The base pressure and the argon partial pressure in the deposition chamber during deposition were ~ 10^{-6} mbar and 4×10^{-3} mbar, respectively. The sputter power and deposition times were maintained at constant values of 130 watt and 7 minutes, respectively for all the depositions. In addition, a pre-deposition sputtering for about 5-10 min was maintained to achieve both sputtering equilibrium as well as to remove any surface oxide present on the Mo target. The thickness of the films thus deposited ranges from 183 – 215 nm as measured by a surface profiler.

4.3.2 Stress measurement using GIXRD

All the XRD measurements in the present study were performed on a Bruker D8 diffractometer with parallel beam Cu kα; $\lambda = 1.5406$ Å. The diffractometer is equipped with a rotating anode (Cu) generator and it is operated at 4.5 kW and 100 mA current. Two methods were used:-

(a) multi *hkl* method

Using a low angle of incidence $\alpha = 0.7^{\circ}$, the 2θ-detector scan was performed for an extended range of 2θ from 30º to 145º to record all measurable reflections in the GIXRD geometry. This extended 2θ scan was used to study the phase characteristics of the deposited films. It further formed the basis for residual stress analysis using multiple *hkl* reflections. It is because in the asymmetric geometry, each diffraction vector of different *hkl* reflection makes different angles with the specimen surface normal. These angles are uniquely related to the specimen tilt angle ψ. As can be seen in Fig. 4.2, the angle ψ for a set of {*hkl*} planes is given by

$$\Psi = \theta^{hkl} - \alpha \qquad (4.11)$$

where 'θ^{hkl}*' is the Bragg angle for a corresponding hkl plane.*

Rotational symmetry of the stress state was checked by measuring the strain at three different azimuth angles ϕ = 0, 45 and 90º 'or' by doing ϕ – scans.

(b) Single *hkl* method

For thin films, it is important to select a ‘strong’ rather than a ‘high’ *hkl* reflection which can be measured with reliable peak-to-noise ratio for an extended range of ψ. Hence in the single *hkl* reflection method, the angle of incidence was fixed at a low value α = 0.7º and the detector scanned the 2θ range from 37.5º to 43.5º to measure the Mo (110) peak – the 100% peak for Mo. The measurement was repeated for various values of the specimen tilt angle ψ. The set of ψ values[†] were chosen so as to obtain an equidistant net of d values in the $\sin^2 \Psi$ plots. The χ-mode (Fig. 4.1b) was used to vary the specimen tilt angle ψ in the range from 0º to 71.57º in a way similar to the traditional $\sin^2\psi$ method, but in the asymmetric parallel beam geometry. The angle α was kept constant for each $\chi \neq 0$ (i.e. each ψ) value by adjusting the angle ω as per the condition given in reference no. 4 which is

$$\sin\alpha = \sin\omega\cos\chi \qquad (4.12)$$

4.3.3 Other experimental details

The compositional distributions of the impurities in the films were probed by using a CAMECA IMS-7F Secondary Ion Mass Spectrometer (SIMS). The parameters used for acquiring the depth profiles were 10 nA Cs^+ primary ion beam current, 45° angle of incidence, 5 keV impact energy, 250 µm raster size and 33 µm analyzed area. The species of interest were sampled as molecular Cs-complex ions viz., $(CsM)^+$, where M is a metal. The SIMS crater depths were determined using a DEKTAK surface profiler. The peak positions (centroid) of all the measured XRD peaks presented in this chapter were determined by line profile analysis using a pseudo-Voigt function fitting.

[†] Values of ψ = 0º,18.43º, 26.57º, 33.21º, 39.23º, 45º, 50.77º, 56.79º, 63.43º and 71.57º

4.4 Experimental Results

The GIXRD patterns for the as-deposited films are shown in Fig. 4.3. The peak patterns were indexed [14] to cubic-bcc structured polycrystalline Mo and these are in good agreement with JCPDS card no: 421120.

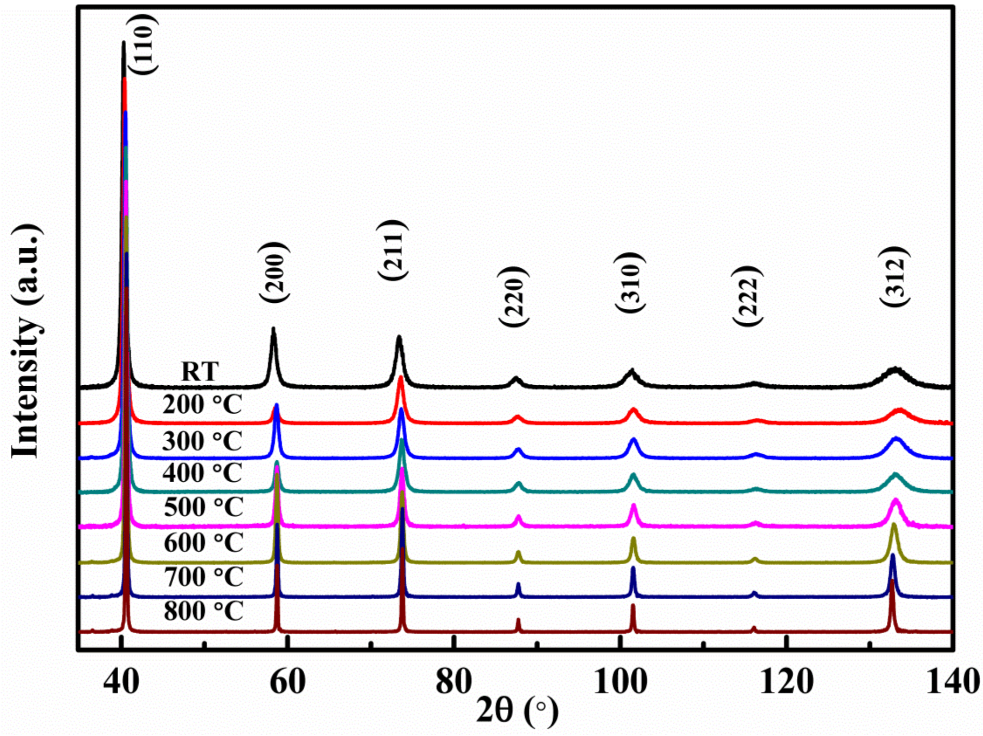

Fig. 4.3 *GIXRD pattern for the Mo thin films deposited at various substrate temperatures.*

For thin films with cubic symmetry, elastic isotropy and rotational symmetry, the residual stresses can be obtained from the slope of linear regressions performed on the strain distribution given by the fundamental equation for X-ray stress analysis in accordance with Eqn. (4.10) and the insertion of appropriate elastic constants. The value of Poisson ratio and elastic modulus used in the present study were: $v = 0.31$ and $\boldsymbol{E} = 329$ GPa, respectively.

4.4.1 Single hkl method

For the single *hkl* peak shift analysis, the strongest reflection Mo (110) was selected as it can safely be measured with a reliable peak-to-noise ratio for the large angular range of tilt angles Ψ from 0 to 71.57 °. The measured values of lattice spacing give the d-$\sin^2\psi$ distribution plot for each specimen. Some representative d-$\sin^2\psi$ plots are shown in Fig. 4.4. The unstrained lattice or d-spacing d_o were determined from the d-distribution plot as the d-value corresponding to the strain free tilt angle Ψ^* which is derived from Eqn (4.10) after setting $\varepsilon_\psi = 0$ as

$$\sin^2 \Psi^* = \frac{2\upsilon}{1+\upsilon} = 0.4732 \tag{4.13}$$

for each film deposited at various temperatures. These d_o values show good agreement with values lying within 2.223 ± 0.004 Å. The lower and upper bound of d_0 value observed in this study are shown in Fig. 4.4. The corresponding plots of lattice strain ε_ψ *Vs* $\sin^2\psi$ obtained for all the specimens are shown in Fig. 4.5. The values of residual stresses obtained upon performing linear regression analyses of the plots shown in Fig. 4.5 are tabulated in Table 1. One can observe that high compressive stress results at low deposition temperature which gradually relaxes and then changes to a tensile one at high deposition temperature. However, unlike films deposited at other temperatures, the d-distribution plot of the films deposited at 400 °C and 500 °C shows an oscillatory behavior (Fig. 4.6) suggesting presence of strong textures/anisotropy in the deposited films. Moreover, there is no significant Ψ-splitting of the d-distribution plot for positive and negative tilts showing the absence of shear stress. Hence, the single *hkl* peak shift analysis fails for cases where anisotropy is introduced by grain texturing/grain interactions.

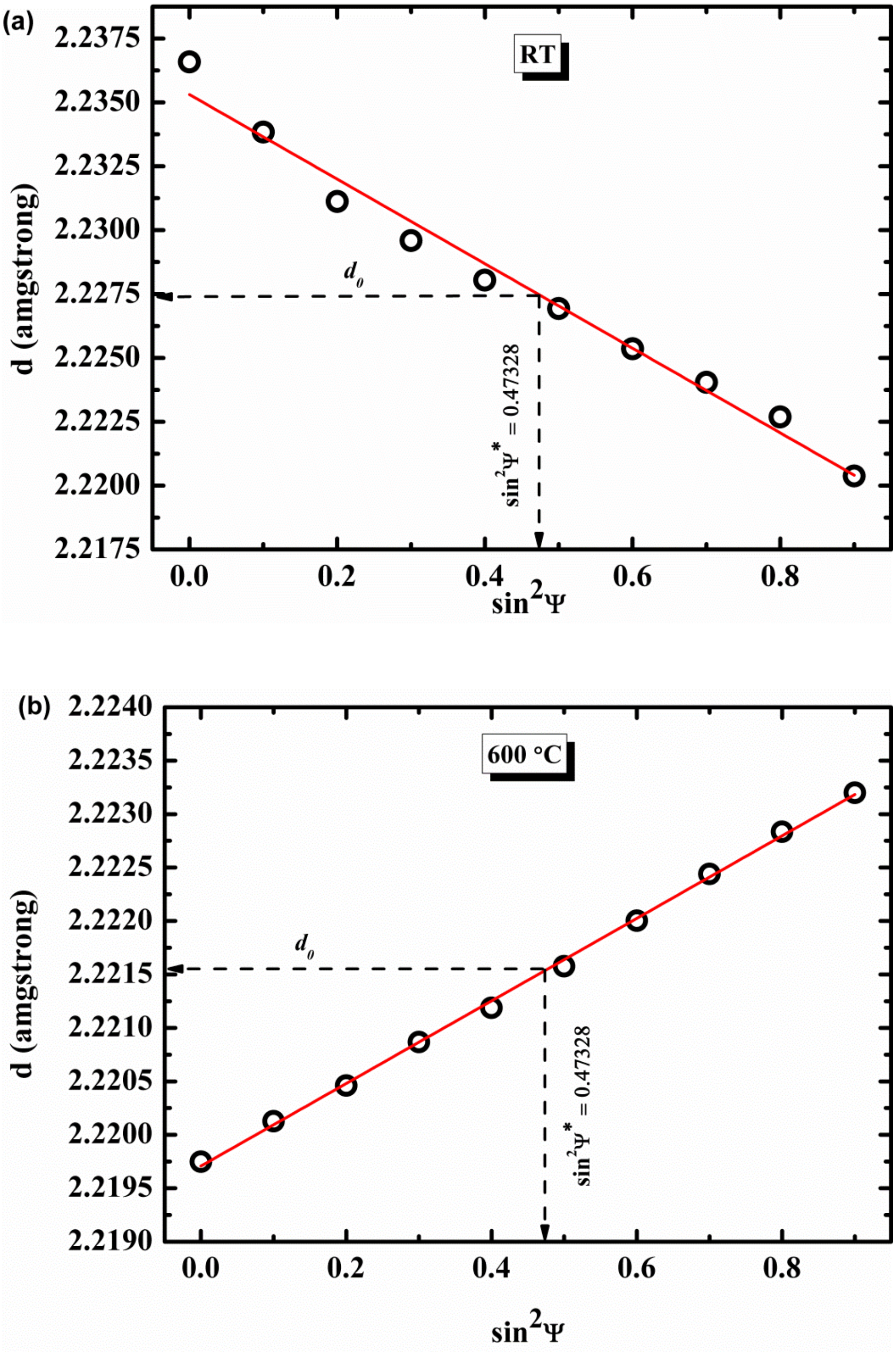

Fig. 4.4 *d-$\sin^2\psi$ plots for (110) reflection of Mo films deposited at (a) room temperature and (b) 600 °C. Ψ^* and d_0, respectively, are the stress free tilt angle and stress free lattice spacing in corresponding film.*

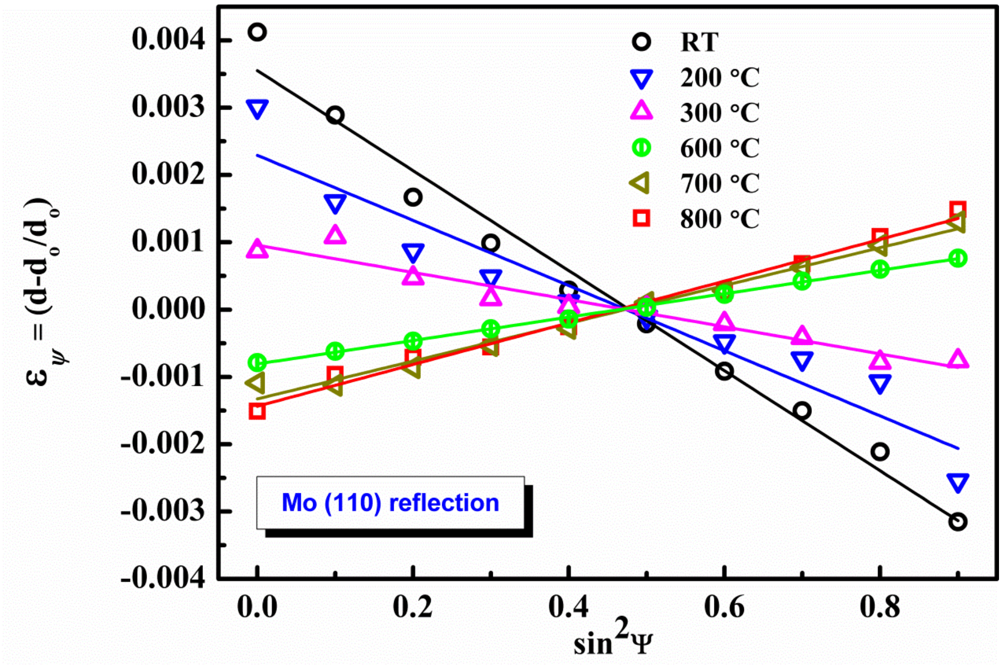

Fig. 4.5 *Lattice strain ε_ψ Vs $\sin^2\psi$ plots from Mo (110) reflections of Mo thin films deposited at various substrate temperatures. The straight lines represent the corresponding linear regression lines.*

4.4.1 Multi hkl method

The peak positions of the GIXRD pattern in Fig. 4.3 were used to perform the multi *hkl* analysis for residual stress in the deposited films. For cubic system, the lattice spacing *d* of each *hkl* reflection is uniquely related to the lattice parameter *a* by the relation

$$a = d\sqrt{h^2 + k^2 + l^2} \tag{4.14}$$

And hence, the strain ε can be expressed either as

$$\varepsilon = \left(\frac{d - d_0}{d_0}\right) \; or \; \varepsilon = \left(\frac{a - a_0}{a_0}\right) \tag{4.15}$$

depending on the availability of either a reliable strain free lattice spacing d_0 or lattice

Table 4.1

Comparison of residual stress values obtained through single hkl and multiple hkl peak shifts analysis in Mo thin films.

Substrate temperature (°C)	**Residual stress $\boldsymbol{\sigma_{\|}}$ (GPa)**		
	Single *hkl* method	**Multi *hkl* method**	
		$\left(\frac{d-d_0}{d_0}\right)$ Vs $\sin^2\Psi$	$\left(\frac{a-a_0}{a_0}\right)$ Vs $\sin^2\Psi$
30	-1.858	-2.526	-2.471
200	-1.215	-2.084	-2.029
300	-0.507	-0.853	-0.798
400	anisotropic	-0.288	-0.233
500	anisotropic	-0. 222	-0.167
600	0.436	0.126	0.181
700	0.705	0.658	0.713
800	0.778	0.728	0.801

parameter a_0. In the former case, as many d_0^{hkl} values as the multiple *hkl* reflections are included in the analysis for the stress determinatiom. In the present study, d_0^{hkl} values from the standard Mo powder data (*JCPDS card no: 421120*) were used to find the corresponding strain in each *hkl* reflection of the measured pattern. In the latter approach, the recorded lattice spacing d of each *hkl* reflection is converted into equivalent lattice parameters a (through Eqn. 4.14) [15] and the strain is determined using the well known bulk lattice parameter of Mo (a_0 = 3.147 Å). Subsequently, residual stress is determined by fitting the measured strain as a function of $\sin^2\psi$ using

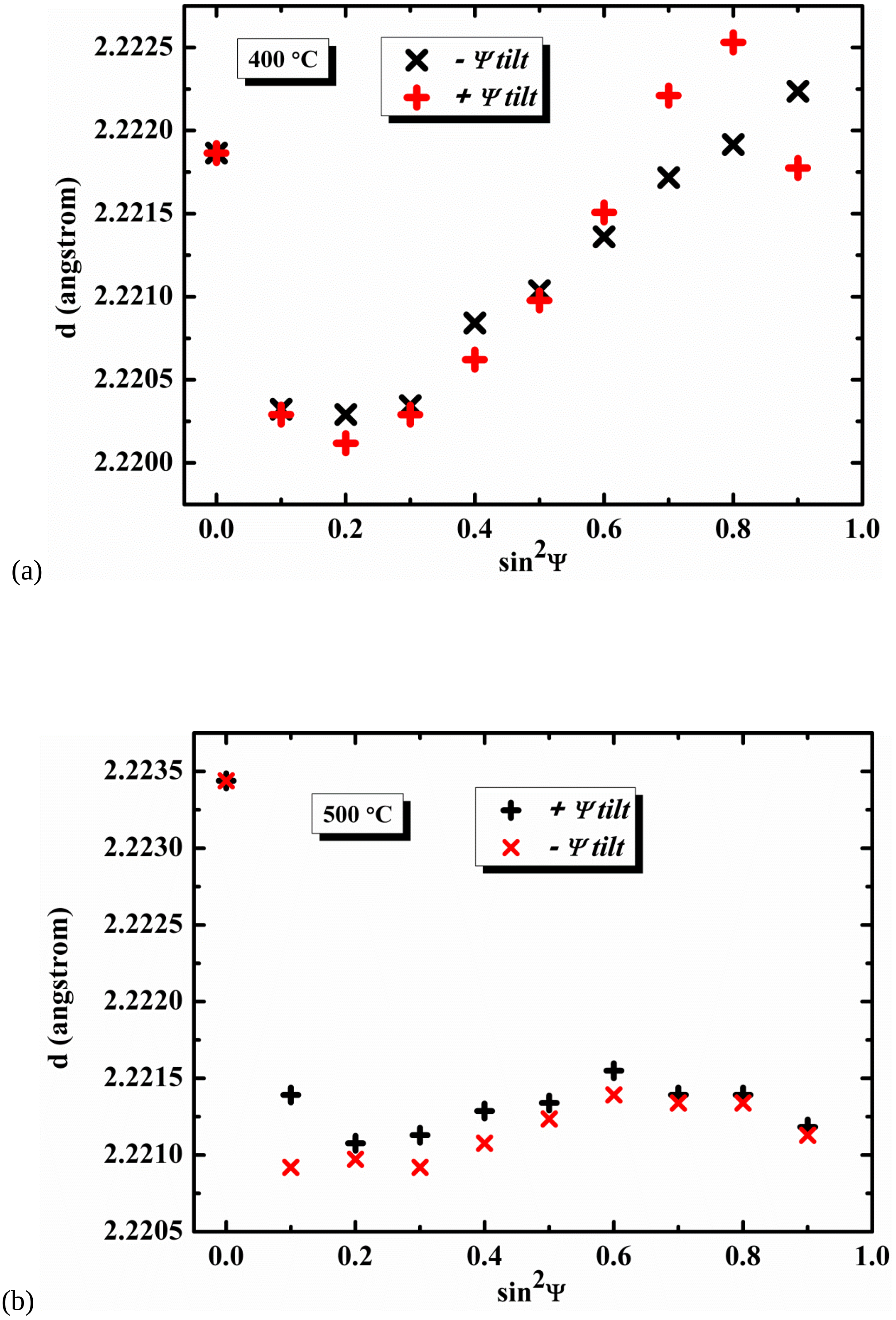

Fig. 4.6 *Oscillatory behaviour in d Vs* $\sin^2\psi$ *plots obtained from (110) reflection of Mo films deposited at (a) 400 °C and (b) 500 °C.*

Equation (4.10). Representative plots showing both the mutli *hkl* approaches are illustrated in Fig. 4.7. Although the latter approach have been claimed to be beneficial [12], no significant difference in the values of the residual stresses were observed in the present study. The values of residual stresses obtained using both these multiple *hkl* approaches are given in Table 1. While both the multi *hkl* methods show comparable values of residual stress, the averaging effect of the stresses over all crystallographic planes in the multiple *hkl* method makes it slightly different from the values estimated using single *hkl* reflection. However, unlike in the single *hkl* method, texture seems to have little effect on the measurement of stress in the multi *hkl* approach as can be seen from ε *Vs* $\sin^2\psi$ plots for 400 °C and 500 °C in Fig. 4.8. This is indicative of the fact that the multi *hkl* approach has distinct advantages over the single *hkl* approach.

Both the single and multi *hkl* approaches clearly demonstrate the general evolutionary trend of residual stress in Mo films as a function of substrate temperature. Low temperature deposited films contain high compressive residual stress. The stress is so high (~ 2.5 GPa) for RT deposited films that blister buckling delamination that is common in compressively stressed film [16-17] is seen in the form of formation of telephone cord structures on aging. Though this kind of delamination may be driven by the wetting of the substrate prior to deposition of the film from the residual water vapour in the deposition chamber, the magnitude of strain energy that is stored in the films deposited at such low temperature compounded the process of delamination into a physical manifested pattern as shown in Fig. 4.9.

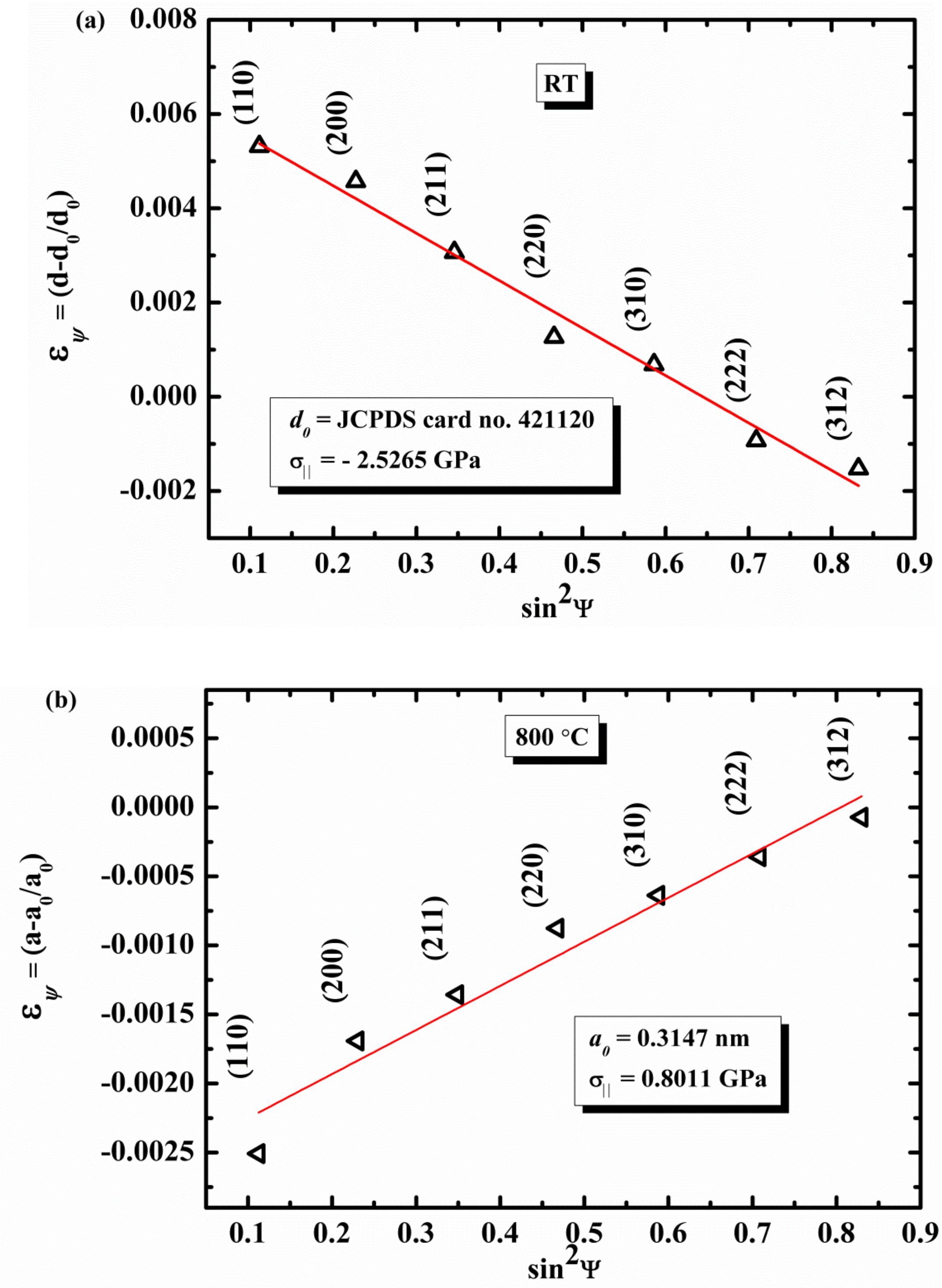

Fig. 4.7 *Lattice strain* ε_{Ψ} *Vs* $sin^2\psi$ *plots for the multi hkl approach (a)* $(d-d_0)/d_0$ *Vs* $sin^2\Psi$ *for RT and (b)* $(a-a_0)/a_0$ *Vs* $sin^2\Psi$ *for 800 °C. The straight lines represent linear regression lines.*

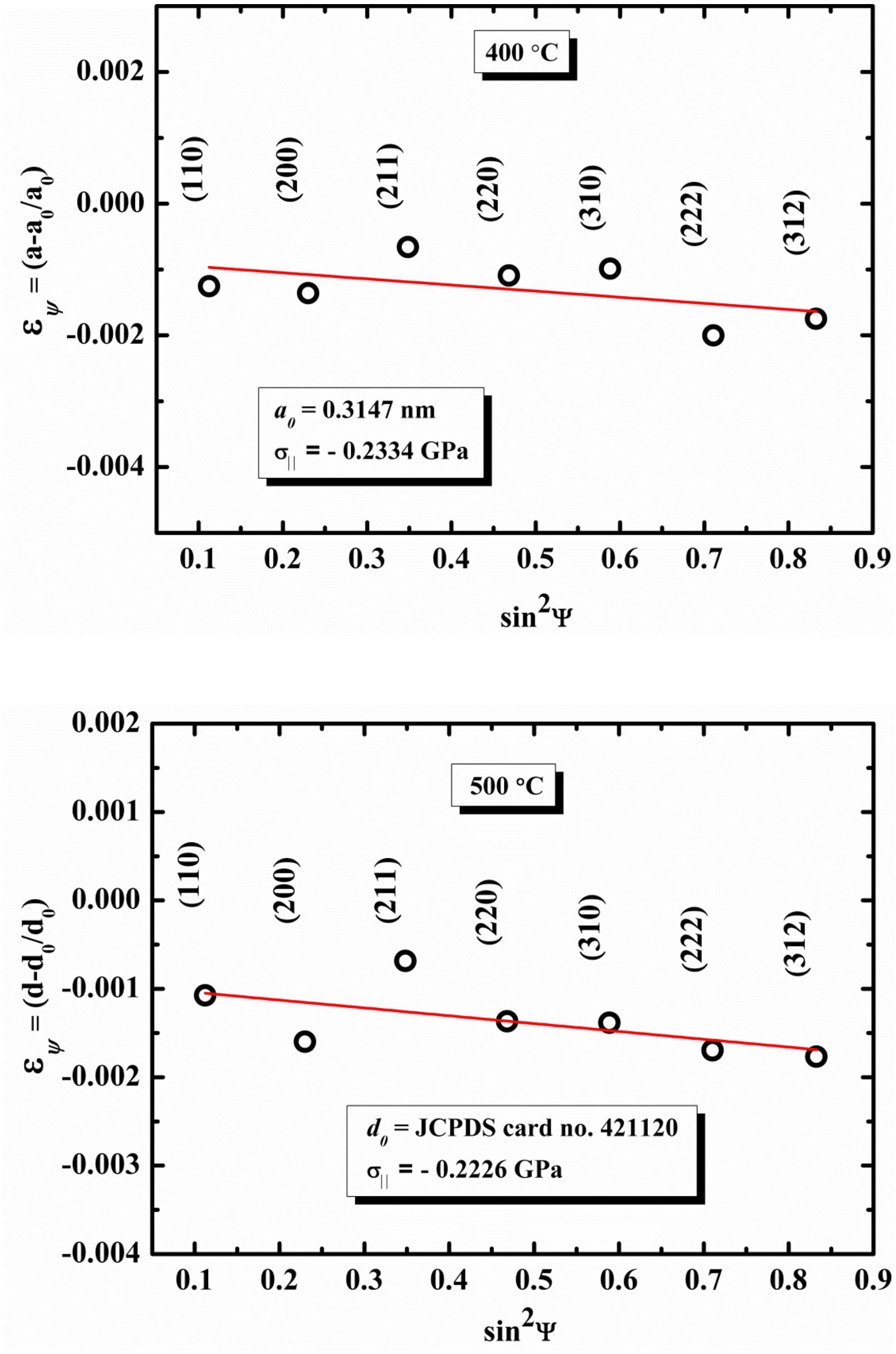

(a)

(b)

***Fig. 4.8** Lattice strain ε_Ψ Vs $sin^2\psi$ plots for the multi hkl approach: (a) $(a - a_0)/a_0$ Vs $sin^2\Psi$ for 400 °C and (b) $(d - d_0)/d_0$ Vs $sin^2\Psi$ for 500 °C. The straight lines represent linear regression lines.*

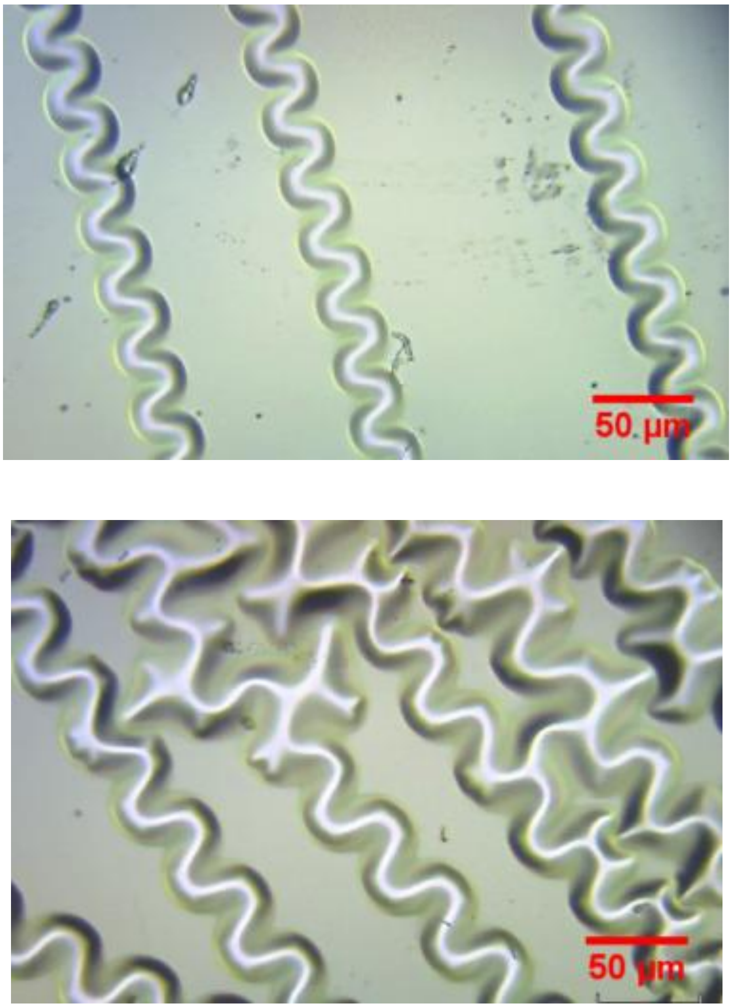

Fig. 4.9 *Telephone cord structure assisted buckling in Mo films deposited at room temperature indicating presence of large amount of compressive stress stored in the film.*

The delamination is absent in rest of the thin film specimen deposited at higher substrate temperature. This is due to the fact that the magnitudes of stress are comparatively less and also because a heated substrate assembly serves to desorb any absorbed water vapour. The magnitudes of compressive residual stress slowly decrease with increasing T_s and it turns into a tensile stress at high T_s.

4.5 Discussion

The evolution of stress as a function of T_s can be understood as below. The total macroscopic residual stress in a thin film system is basically composed of two components – (a) intrinsic and (b) thermal components [18]. Intrinsic stress is the component of stress that results from the cumulative effects of crystallographic defects that occur due to the non-equilibrium nature of the growth process. Thermal stress is the component that results because of the mismatch in thermal expansion co-efficient of the film and the substrate; it is generally observed when the film-substrate system is cooled down to RT after deposition. Generally, intrinsic stress dominates at low T_s and is important for films with low ad-atom mobility, but thermal stress gains importance and dominates at high T_s. For films whose thickness is small in comparison with the substrate's thickness and assuming that the plastic flow in the substrate is negligible, the thermal stress in the film is given by [18]:

$$\sigma_{th} = \frac{E_f}{(1-\upsilon)}\left(\alpha_f - \alpha_s\right)(T_s - T_a) \tag{4.14}$$

where E_f is the young's modulus of the film, α_f and α_s are the average thermal expansion co-efficient for the film and substrate, respectively. T_a is the temperature at which stress measurement is carried out (usually RT).

A positive value of σ_{th} indicates a tensile stress while a negative value that of compressive stress. As T_s almost invariably exceeds RT (T_a) in all practical cases, a tensile stress is generally expected for films having higher thermal expansion co-efficient than the substrate. Accordingly, from Equation (4.14), a tensile stress is expected when Mo is deposited on Si substrate because of the higher thermal expansion co-efficient of Mo than Si at all range of temperatures [19-20]. The calculated values of thermal stresses that are expected to be generated in Mo films deposited at different elevated temperatures upon cooling down to RT are given in Table 2. There is a good agreement between these calculated values and the values estimated from X-ray stress analysis at high T_s as shown in Fig. 4.10. Hence, the observed tensile stress in films deposited at high T_s is attributed to the thermal stress generated in the Mo films upon being cooled down to RT. However, such an observation is overshadowed by the dominance of intrinsic stress at low T_s. At low T_s, the ad-atoms mobility is quite low and intrinsic stresses that are compressive in nature results, the reason for which is analyzed and deliberated in the following.

Table 4.2

*Values of thermal stress expected in Mo films deposited on Si substrate at various elevated temperatures from Equation (4.14) with data from Ref. 19 and 20***.**

Substrate temperature (°C)	Thermal stress σ_{th}(GPa)
200	0.16
300	0.237
400	0.313
500	0.40
600	0.51
700	0.638
800	0.795

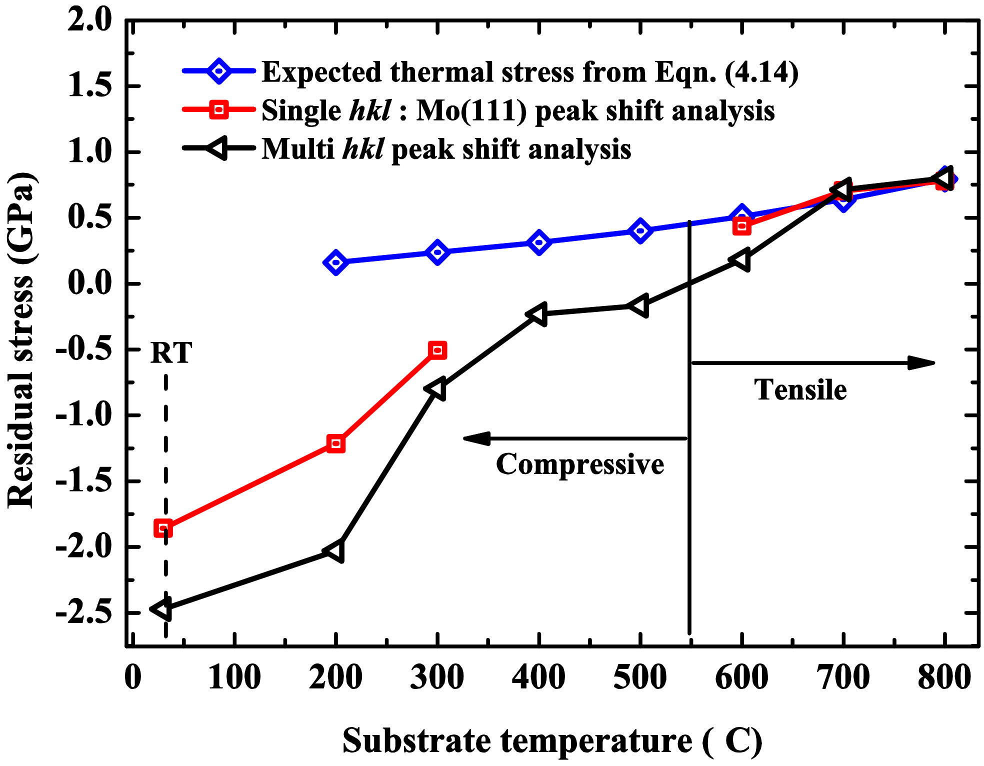

Fig. 4.10 *Evolution of residual stress in sputter deposited Mo thin films as a function of substrate temperature.*

Atomic peening from reflected neutral argon atoms had been long considered as the cause of compressive stress in sputter deposited thin films [21-23]. However, it is more so for cylindrical magnetron and forms small to negligible contribution for planar magnetron geometries [24]. In cases where such peening process is profound, the amount of trapped working gas (Ar) in the films will serve to indicate the extent of such peening effect. Fig. 4.11 shows the SIMS compositional depth profiles of Ar and O impurities in the deposited films. It is observed that the Ar intensity and hence the amount of atomic peening thereby ascribable to it, are constantly low in all the thin film specimen, revealing that peening is indeed negligible for the planar magnetron geometry used in the present study. On the other hand, the presence of oxygen impurities can be observed in the films deposited at low T_s below 500 °C, while films deposited at high T_s and above 500 °C are free of oxygen impurities. It has been recently reported that the origin of compressive stress in polycrystalline thin films can be traced to diffusion of ad-atoms into the grain boundaries because of higher than equilibrium condition that raise the surface chemical potential during growth [25-26]. And since the O impurities get completely desorbed from the growing film at high temperature $T_s > 500$ °C, it is less likely that it occupies a substitutional impurity site. With less thermal energy for desorption at low T_s, the most probable place for O atoms to get absorbed into the growing film are the grain boundaries. These O atoms may also play a decisive role in the evolution of the film's microstructure as a function of substrate temperature (which mainly influences the ad-atom mobility). The cross sectional SEM micrographs of Fig. 4.12 illustrate the micro-structural evolution of the Mo films deposited at different substrate temperatures. Features ranging from wavy crystalline to fibrous grains that are characteristics of zone *I* in Thornton's structure zone model (SZM) scheme [27], and Zone *Ia, Ib* and *Ic* of the extended SZM scheme of Mahieu [28] can be seen in low temperature deposited films. The growth of these fibrous grainy features through diffusion is limited by both the oxygen impurities and ad-atoms mobilities at relativity low T_s. This fact is further supported by the observation of T. Yamaguchi et al. where they investigated the role of O in decreasing the width of the fibrous grains with increasing oxygen and the associated compressive stress it generates [29]. Hence, the compressive nature of the intrinsic stress prevailing at low deposition temperature is attributed to the oxygen impurities that are incorporated into the growing film along with other defects associated with low ad-atom mobility. And as T_s increases, thermal desorption of O atoms increases and correspondingly ad-atom mobility also increases leading to grain

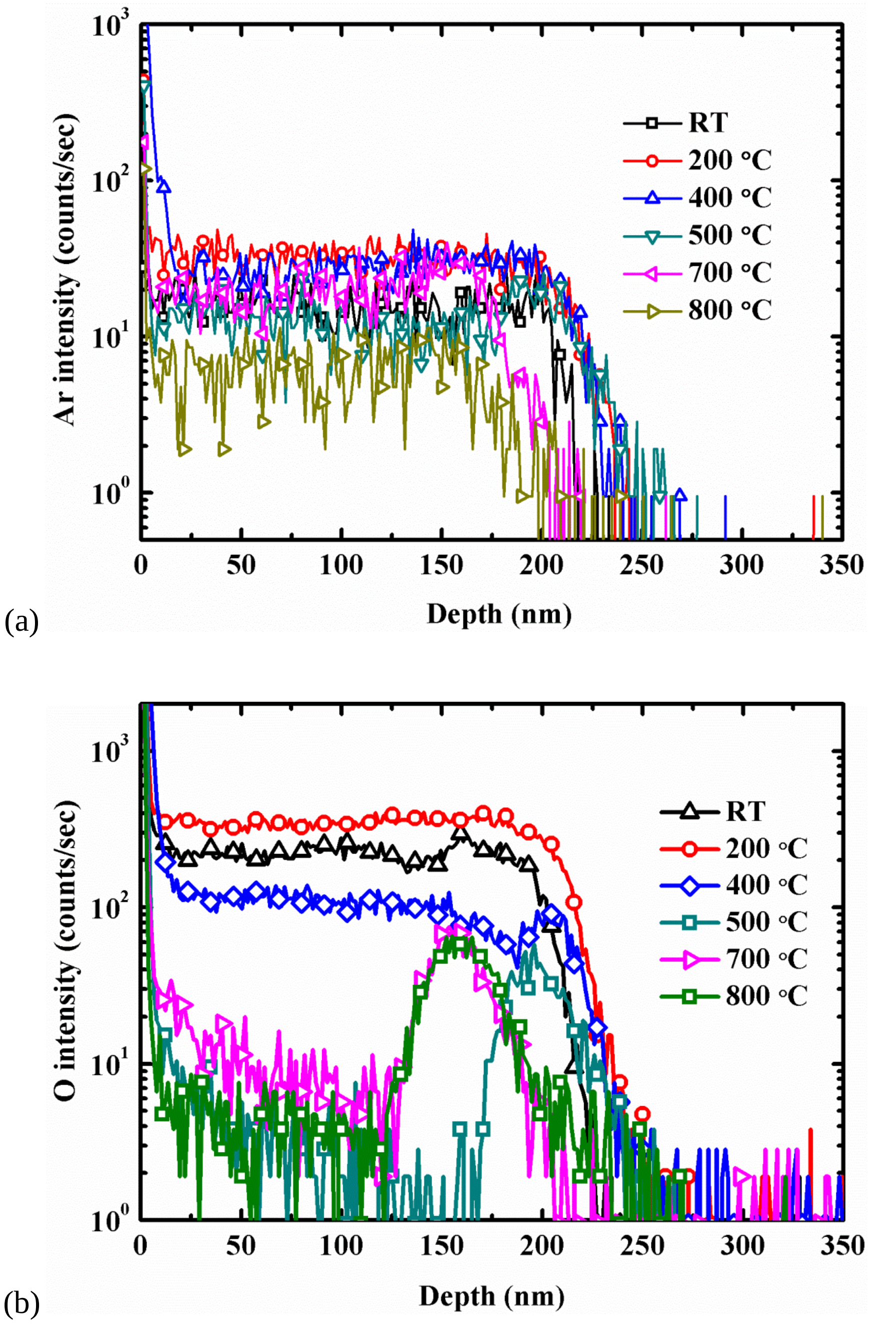

Fig. 4.11 *SIMS depth profiles of (a) Argon and (b) Oxygen, in Mo films deposited at various substrate temperatures.*

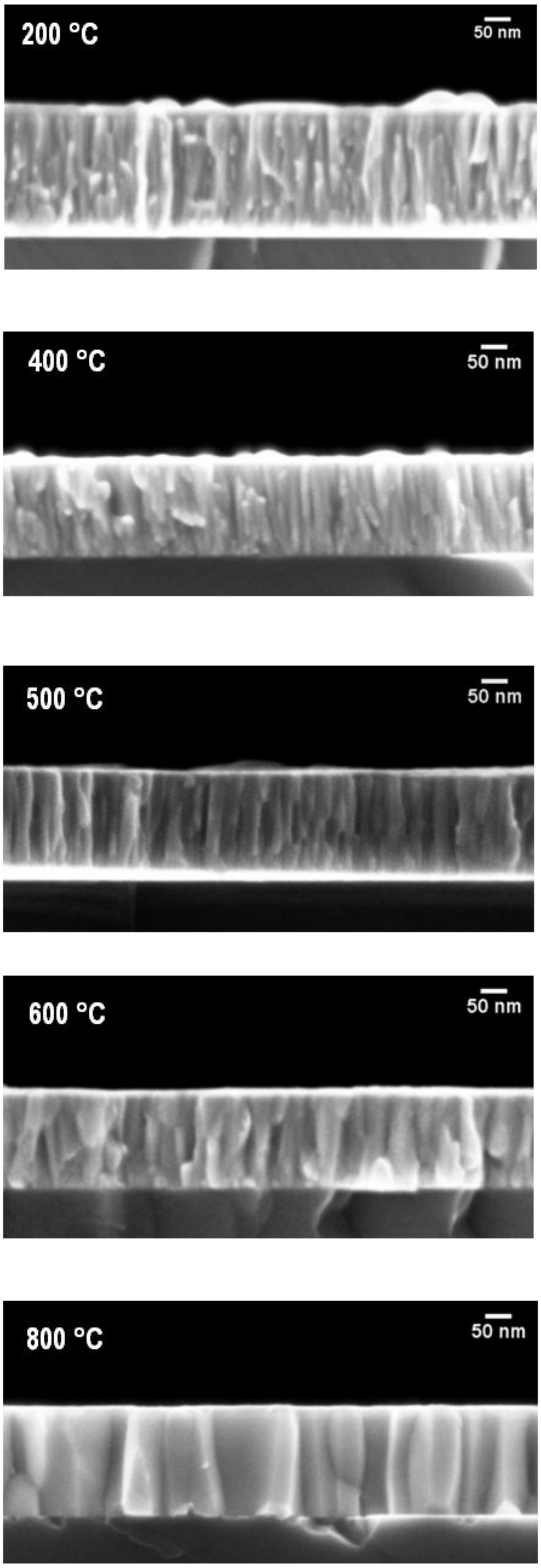

Zone I of SZM

Zone T

Zone II – re-crystallization

Fig. 4.12 *Cross sectional micrographs of Mo films deposited at various substrate temperatures.*

restructuring in terms of grain growth and finally leading to re-crystallization at higher temperature which aids the expulsion of O from the growing films. While facet poly-crystals with distinct columnar structure that are characteristics of inter grain diffusion of ad-atoms expected in the zone *T* of the SZM were observed for films deposited above 600 °C, re-crystallization were observed for higher T_s at 800 °C (Fig. 4.12). The subsequent attractive interaction along the boundaries of the compactly packed columnar grains at higher T_s along with the mismatch in thermal expansion co-efficient between the Mo films and Si substrate result in a tensile stress at high T_s.

Conclusion:

The effects of substrate temperature on the resulting residual stresses in sputtered deposited polycrystalline Mo thin films deposited on Si were investigated using X-ray diffraction studies employing both single *hkl* as well as multiple *hkl* methods. High compressive stress (as high as 2.5 GPa for RT deposited film) were observed at low deposition temperature while the stress was tensile at high deposition temperature. While the compressive stress results from the intrinsic component of stress introduced by O impurities during growth at low T_s, thermal stress due to mismatch in average thermal expansion co-efficient of the film and substrate reverses it to tensile stress at high T_s.

References

---

1. J. A. Thornton and D. W. Hoffman, Thin Solid Films, 171 (1989) 5-31.
2. L. B. Frreund and S. Suresh, *Thin Film Materials: Stress, Defect Formation and Surface Evolution*, Cambridge University Press, UK, 2003.
3. L. Fabrega, I. Fernandez-Martinez, M. Parra-Borderias, O. Gil, A. Camon, R. Gonzalez-Arrabal, J. Sese, J. Santiso, J.-L Costa-Kramer and F. Briones, *Applied Superconductivity*, 19, no.6 (2009) pp.3779 – 3785.
4. U. Wezel, J. Ligot, P. Lamparter, A.C. Vermeulen and E. J. Mittemeijer, J. Appl. Cryst. 38 (2005) 1-29.
5. G.C.A.M. Janssen, M.M. Abdalla , F. van Keulen, B.R. Pujada and B. Van Venrooy, *Thin Solid Films* 517 (2009) 1858–1867
6. C. Quaeyhaegens, G. Knuyt and L.M. Stals, Surf. Coat. Technol., 74-75 (1995), 104 -109.
7. C.-H. Ma, J.-H. Huang, H. Chen, Thin solid films 418 (2002) 73-78
8. M van Leeuwen, J. –D. Kamminga and E.J. Mittemeijer, *J. Appl. Phys*. 86 (1999) 1904.
9. K. V. Acker, L. De Buyser, J. P. Celis and P. V. Houtte, *J. Appl. Cryst.* 27 (1994) 56.
10. V. Valvoda, R. Kuzel, JR., R. Cerny, D. Rafaja, J. Musil, S. Kadlec and A.J. Perry, *Thin Solid Films* 193/194 (1990) 401.
11. A. C. Vermeulen, Mater. Sci. Forum, 404-407 (2002) 35-42
12. A. Baczmanski, C. Braham, W. Seiler and N. Shiraki, Surf. Coat. Technol. 182 (2004) 43-54

13. M. Birkholz, *Thin films analysis by X-ray scattering,* Wiley-VCH, Weinheim, 2006, pp - 243
14. B. D. Cullity, Elements of X-Ray Diffraction, Addison-Wesley, Massachusetts, 1956
15. A. J. Perry, *Surf. Coat. Technol*. 41 (1990) 231.
16. P. Waters and A. A. Volinsky, Exp. Mech., 47 (2007) 163-170
17. J-Y. Faou, G. Parry, S. Grachev and E. Barthel, Phys. Rev. Lett. 108 (2012) 116102.
18. G. Totten, M. Howes and T. Inoue, Handbook of Residual Stress and Deformation in Steel, ASM international, 2002 p-118-124.
19. Kai Wang and Robert R. Reeber, Materials Science and Engineering, R23 (1998) 101-137
20. Robert R. Reeber and Kai Wang, Materials Chemistry and Physics, 46 (1996) 259-264
21. J. A. Thornton and D. W. Hoffman, *J. Vac. Sci. & Technol,* A3 (1985) 576.
22. J. A. Thornton, J. Tabock and D. W. Hoffman, *Thin Solid Films*, 64 (1979) 111-119
23. D. W. Hoffman and J. A. Thornton, *Thin Solid Films*, 40 (1977) 355-363.
24. J. A. Thornton and D. W. Hoffman, *Thin Solid Films*, 171 (1989) 5-31.
25. J. W. Shin and E. Chason, *Phys. Rev. Lett.* 103 (2009) 056102
26. R. Koch, D. Hu, and A. K. Das, Phys. Rev. Lett. 94 (2005) 146101
27. J.A. Thornton, *Annu. Rev. Mater. Sci*. 7 (1977) 239.
28. S. Mahieu, P. Ghekiere, D. Depla, R. De Gryse, *Thin Solid Films*, 515 (2006) 1229–1249.

29. T. Yamaguchi and R. Miyagawa, Jap. J. of Appl. Phys., 30 (9A) (1991) 2069-2073.

CHAPTER 5

EFFECT OF MICROSTRUCTURE ON SECONDARY ION MASS SPECTROMETRY DEPTH PROFILING OF POLYCRYSTALLINE-Mo/Si INTERFACE

5.1 Introduction

There is an ever increasing use of materials in thin film devices for various technological applications. As such, interfacial characterization of thin film bilayers, multilayers or any other hetero-interface, both chemically and structurally, and understanding the basic interface phenomena therein are crucial for device related applications. Hence, understanding and progress in interface science plays a major role in the future development of advanced materials technology [1]. Surface and interface analytical techniques that employ combination of ion sputtering and spectrometry, although destructive in nature, have found widespread application for the chemical analysis of thin films and interfaces. It is because of their superior ability to perform elemental depth profiling with optimal resolution close to atomic monolayer. Among them, Secondary Ion Mass Spectrometry (SIMS) is the most commonly used technique of choice for elemental depth profiling and compositional analysis, mainly because of its high sensitivity and dynamic range [2]. However, SIMS depth profile analysis is always accompanied with its inherent artifacts. There are fundamental and instrumental aspects that limit the depth resolution [3]. There are several factors that can cause distortion in the profile shape like sputter induced change in surface composition and surface topography, surface roughness, matrix effect and radiation induced effects [4-8] that may lead to wrong interpretation. Hence, a careful data analysis acquires utmost importance before interpreting a measured depth profile. Especially, depth profile analysis of polycrystalline or grained materials, in particular metal films, becomes fairly complex due to the presence of sometime ambiguous interface profile broadening. This ambiguity arises because both a real diffusive phenomenon as well as characteristics of samples and the experimental process can give rise to interface profile broadening. Non uniform sputtering of the differently oriented crystalline grains can also degrade the depth resolution and broaden the interface making it look apparently diffused. In addition, whenever sufficient amount of thermal energy is supplied to a metallic thin film bilayer, either by post annealing or raising the temperature during deposition, a thermally activated inter-diffusive phenomenon can occur across the interface leading to broadening of the profile shape at the interface.

In this chapter, systematic investigation on the effect of micro-structures and morphological characteristics of Mo films in the interfacial characterization of polycrystalline Mo/Si system is discussed. The diffusion aspects across the interface were also investigated by depositing the films at 800 ºC which was supposed to be high enough to induce a thermally activated inter-diffusive process [9]. The ensuing results are discussed with experimental results using several surface analytical techniques. Additionally, the effect of surface roughness on the resulting interfacial profile broadening in the SIMS depth profile is also discussed.

5.2 Sample preparation and experiments

5.2.1 Thin film deposition

For the present study, polycrystalline Mo thin films were sputter deposited onto clean *p*-Si (111) substrates from a pure 2” Mo target using a radio frequency magnetron sputtering unit. The substrate temperature T_s was systematically varied from room temperature (RT) to 800 °C in steps of 100 °C. The base pressure and the argon partial pressure in the chamber during deposition were ~ 10^{-6} mbar and 4×10^{-3} mbar respectively. The sputter power and deposition times were maintained at constant values of 130 watt and 7 minutes respectively for all the depositions. In addition, a pre-deposition sputtering for about 5-10 min was maintained to achieve both sputtering equilibrium as well as to remove any surface oxide on the Mo target. The thickness of the films thus deposited ranges from 170 – 200 nm as measured by Dektak stylus profiler and a field emission-scanning electron microscope giving deposition rates in the range 0.4 – 0.47 nm/sec.

5.2.2 Crystallinity, phase and microstructure

The phase characteristics of the as-deposited films were investigated in a Bruker D8 diffractometer in parallel beam geometry with Cu kα radiation (λ = 1.5406 Å) at 0.7º. The diffractometer is equipped with a rotating anode (Cu) generator and it is operated at 4.5 kV and 100 mA current. The topographical and micro-structural characteristics of the films were investigated using a NT-MDT Atomic Force Microscope (AFM) and Field Emission Scanning Electron Microscope (FE-SEM) respectively.

5.2.3 Elemental depth profiling

A CAMECA IMS-7f SIMS was used for the compositional and interfacial characterization of the as-deposited films. The parameters used for the SIMS depth profiling were 10 nA Cs^+ primary ion beam current, 45 ° incident angle, 5 keV impact energy, 250 µm x 250 µm raster size and an analyzed area of 33 µm diameter. The species of interest were sampled either as elemental or quasi-molecular Cs-complex ions viz., $(CsM)^+$ *where M is a metal*, based upon enhanced secondary ion yield and less matrix effect considerations. Accordingly, quasi-molecular Cs-complex ions viz., $(CsMo)^+$, $(CsO)^+$, $(CsAr)^+$ and $(CsC)^+$ were sampled for Mo, O, Ar and C respectively, whereas elemental Si^+ was sampled for Si. The SIMS crater depths were determined using a Dektak 6M stylus profiler. Rutherford Backscattering Spectrometry (RBS) measurements were also performed using a 2 MeV He^+ ion beam. The energies of the backscattered particles were measured with a surface barrier detector kept at 165 º to the incident beam.

5.3 Experimental results

5.3.1 X-ray diffraction

The GIXRD patterns for the as-deposited films shown in Fig. 5.1 were found to be polycrystalline in nature as expected. The degree of crystallinity increases with an increase in T_s. The XRD peak patterns were indexed [10] to cubic - bcc structured Mo and these are in good agreement with JCPDS card no: 421120. There is no signature of any silicide phase formation in all the samples, including the one deposited at T_s = 800 ºC. The average crystallite sizes for these various samples deposited at different T_s were determined using Scherrer's formula;

$$t = \frac{0.94\lambda}{\beta \cos\theta} \tag{5.1}$$

where λ = 0.15406 nm, β is the full width at half maximum in radian and θ is the Bragg angle. The values are given in Table 1. It varies from a minimum of ~ 6 - 8 nm at low deposition temperature to a maximum of ~ 41 nm at 800 °C. Significant growth of the crystallites does not occur until a deposition temperature of 400 °C. At T_s above 400 ºC, the surface ad-atom mobility increases providing sufficient energy for the ad-atom to diffuse along the surface and agglomerate into bigger grains or crystallites.

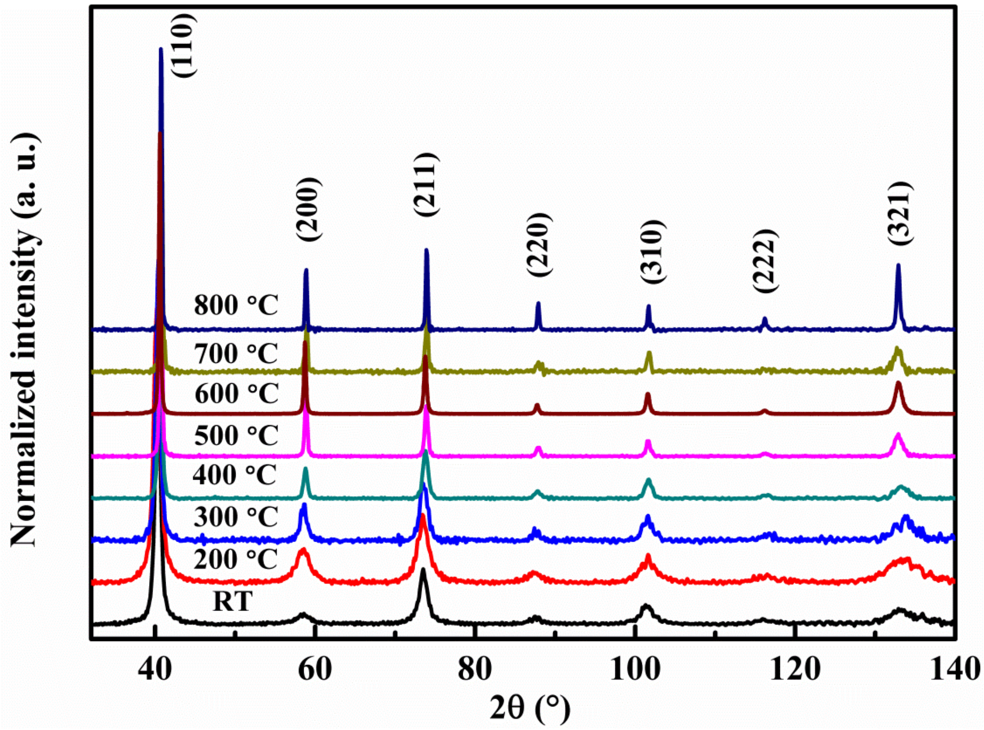

Fig. 5.1: GIXRD patterns of the room temperature and various other elevated substrate temperatures as-deposited Mo films.

Table 5.1

Average crystallite size estimated for the as-deposited Mo films using Scherrer's formula.

Substrate temperature (°C)	*Crystallite sizes (nm)*
RT	*8.17*
200	*6.00*
300	*9.68*
400	*13.86*
500	*21.53*
700	*27.78*
800	*41.31*

5.3.2 Microstructure: SEM

The evolution in the micro-structural characteristics of the as-deposited films as a function of T_s is probed by a FE-SEM. The cross sectional SEM micrographs of Fig. 5.2 illustrate the film growth structure and morphological features along the growth direction. The as-deposited films were observed to exhibit a columnar like micro-structural growth, similar to earlier studies reported by Drüsedau et al., [11] but with varying degrees of grain growth and microstructure. The observed micro-structural evolution was mainly influenced by surface mobility of the ad-atoms since T_s was the only control parameter being varied. This micro-structural evolution is best described by the structure zone model (SZM) originally proposed by Movchan and Demchisin [12], and Thornton [13] and extended by others [14-15] in terms of homologous temperature T, defined as the ratio of T_s to the melting temperature of the deposited material T_m. The as-deposited films in the low temperature regime have very low surface mobility and correspondingly limited surface diffusion leading to features ranging from weak wavy crystalline features to fibrous grains. This range from RT to T_s = 400 °C ($0.1 < T < 0.23$) roughly falls into the zone I category of SZM according to descriptions given in *Ref. 14*. And in the extended SZM scheme of *Ref. 15*, the range $0.1 < T < 0.19$ (below $T_s \approx 300$ °C) fits into the zone Ia and Ib, whereas the range $0.19 < T < 0.26$ ($T_s \approx 400$ °C) into the zone Ic which contains faceted polycrystalline grain. In the intermediate temperature range i.e. $0.26 < T < 0.33$ (T_s ~ from 500 °C to 700 °C), the thermal energy provides sufficient surface mobility for inter-grain diffusion to the ad-atoms. The growth in this temperature range fits into into the Zone T of the SZM scheme. This transition zone is characterized by closely packed faceted columnar grain. At still higher temperature, $T \approx 0.37$ (T_s = 800 °C) the film's microstructure evolves into a recrystallized and restructured dense columnar grains spanning across the whole thickness of the film which is a characteristics feature of Zone II. The transition from zone T to zone II in the present set of samples takes place in the interval of T values between 0.33 and 0.37. Systematic investigation of the interfacial characteristics of these Mo films with varied micro-structural features is performed with the objective to gain better understanding of the interface phenomenon and artifacts that normally arises in SIMS depth profiling of a polycrystalline metal. This will unravel the cause behind the broadening with regard to either diffusion or the influence of micro-structure.

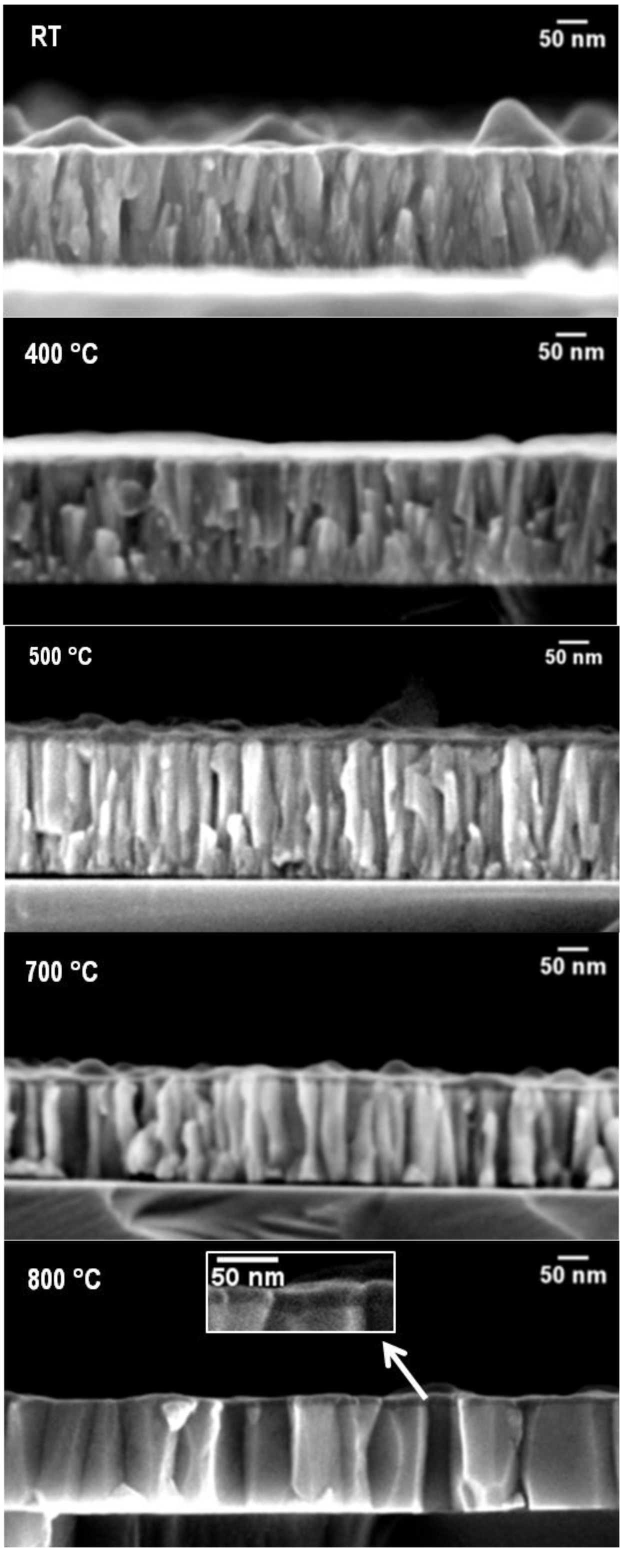

Fig. 5.2 *Cross sectional FESEM micrographs of the Mo films deposited at various substrate temperatures showing the micro-structural evolution.*

5.3.3 Secondary ion mass spectrometry

SIMS depth profiles of the various as-deposited samples are shown in Fig. 5.3. The sputtering times in these profiles were converted into depth scale assuming a linear dependence of the instantaneous sputtering rate on composition [16]. The Mo and Si profiles for the RT as-deposited film show a finite broadening at the interface (Fig. 5.3). This broadening is observed to increase systematically as a function of T_s, akin of a T_s dependent real-diffusive phenomenon that could have resulted upon annealing. However, sample characteristics like surface roughness, poly-crystallinity and processes operative during sputtering like ion beam mixing and sputter induced roughening may also give rise to such a broadening. In a similar work, Kiyohisa et al., [17] have reported the correlation between the sputter induced roughening and the grain size in Mo thin films. However, they employed high primary ion energy (14.5 keV) and beam current (100 nA) which could result in large collision cascade that severely limit the depth resolution. They have used oxygen profiles to study the subsequent degradation in depth resolution resulting from sputter induced roughness (SIR). Hence, a better depth resolved analysis with low primary ion energy and ion beam current becomes an important prerequisite for understanding of the broadening. The influence of microstructure of the Mo thin films upon the interface width (IW) in the SIMS depth profiles is the subject matter of this investigation.

In addition to Mo and Si, compositional distribution of probable impurities viz., oxygen, carbon and argon were also sampled. The contaminations from argon and carbon were found to be negligibly low. However, oxygen was found to be a major source of impurity for films deposited at low T_s, in the range from RT to 400 ºC and they are shown in Fig. 5.3. The small peaks seen at the interface of Mo film and Si substrate is due to the inherent native oxide layer of Si. However, as T_s increase

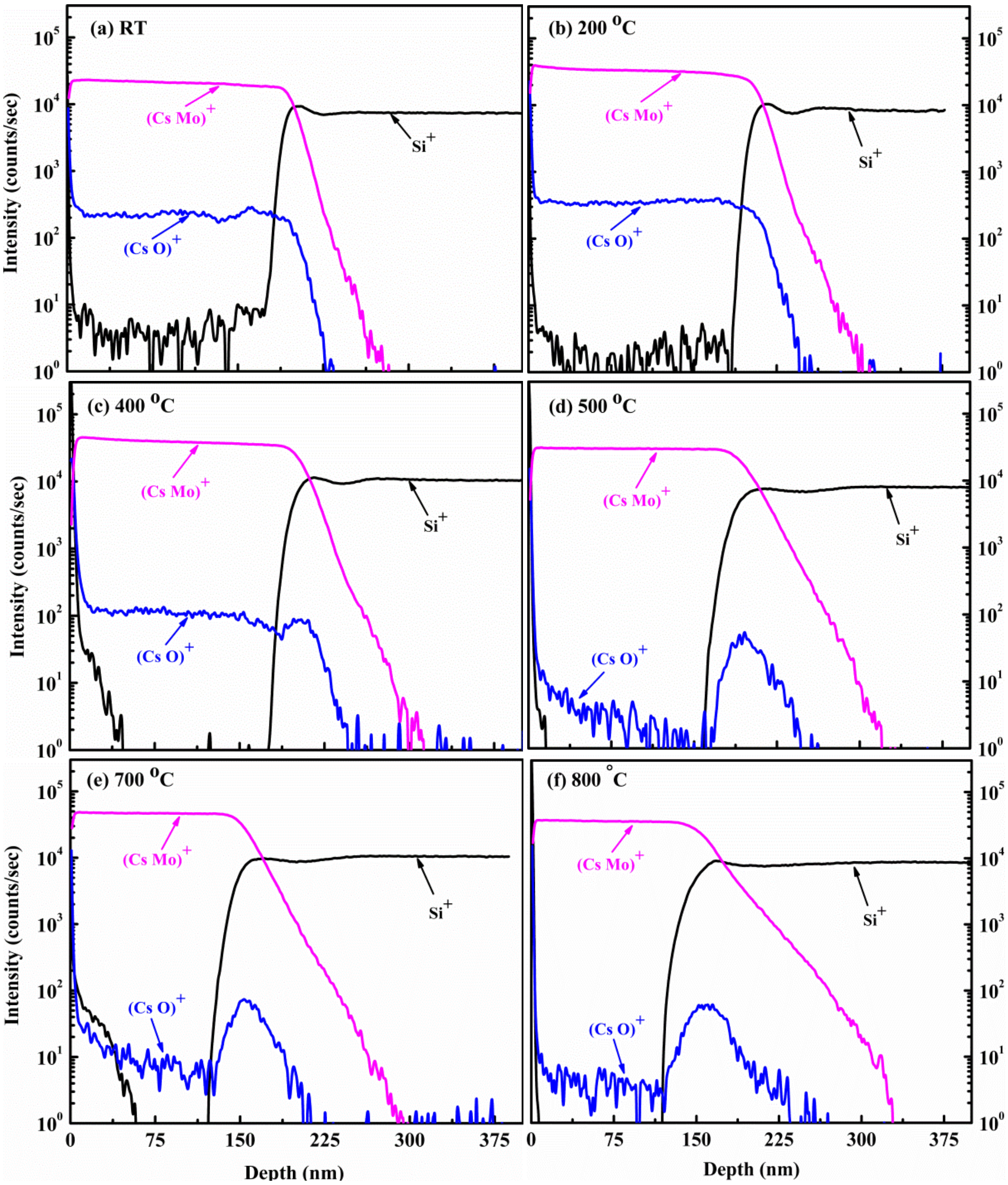

***Fig. 5.3** SIMS depth profiles of Mo, Si and O for as-deposited at (a) RT, (b) 200 °C, (c) 400 °C, (d) 500 °C (e) 700 °C and (f) 800 °C.*

above 500 ºC, the oxygen intensity falls to the background level suggesting deposition of Mo films free of oxygen impurities. This observation can be accounted in terms of the temperature (T_S) dependent sorption-desorption process operative during deposition. Oxygen from the residual background can be readily physisorbed onto the substrate i.e., the growing film’s surface. Unlike chemisorptions, physisorption does not involve any activation energy, it proceeds till the gas and the adsorbate attain equilibrium at the sample surface [18]. The adsorptions of oxygen on freshly deposited films are most likely to account for the high oxygen content in the film at low temperature (T_s). But as T_s increases, thermal desorption become increasingly important and above 500 °C, complete thermal desorption of the adsorbed oxygen takes place resulting in oxygen free Mo film.

5.3.4 Topography: AFM

The topography of the as-deposited surface and the craters subsequently formed after sputter depth profiling by SIMS were measured by AFM in tapping mode. The same tip was used for acquiring all the images to remove any ambiguity that may arise due to tip size effects. The measurements show that all the as-deposited films have smooth surface topography. However, the values of the surface roughness of the craters formed after sputtering away Mo films was found to increase with T_s. The *rms* roughnesses on the surfaces of the samples measured over an area of 5 x 5 μm^2 were *0.31, 1.02, 1.15, 1.21 and 1.56 nm* for films as-deposited at *RT, 300 °C, 400 °C, 500 °C and 800 °C,* respectively. For comparison, the *rms* roughness of the Si substrate was 0.3 nm for a 5 x 5 μm^2 scan area. Similarly, the crater roughness obtained for samples in the above sequence were *3.5, 5.3, 6.7, 7.33 and 13.7 nm,* respectively. This phenomenon of increase in roughness results from the preferential sputtering of the underlying polycrystalline grains with different crystalline orientation to the primary ion beam, leading to the formation sputtering angle dependent topographic features (i.e., hills and valleys). This effect of varied microstructure on the roughness of the crater surface that results on subsequent sputter

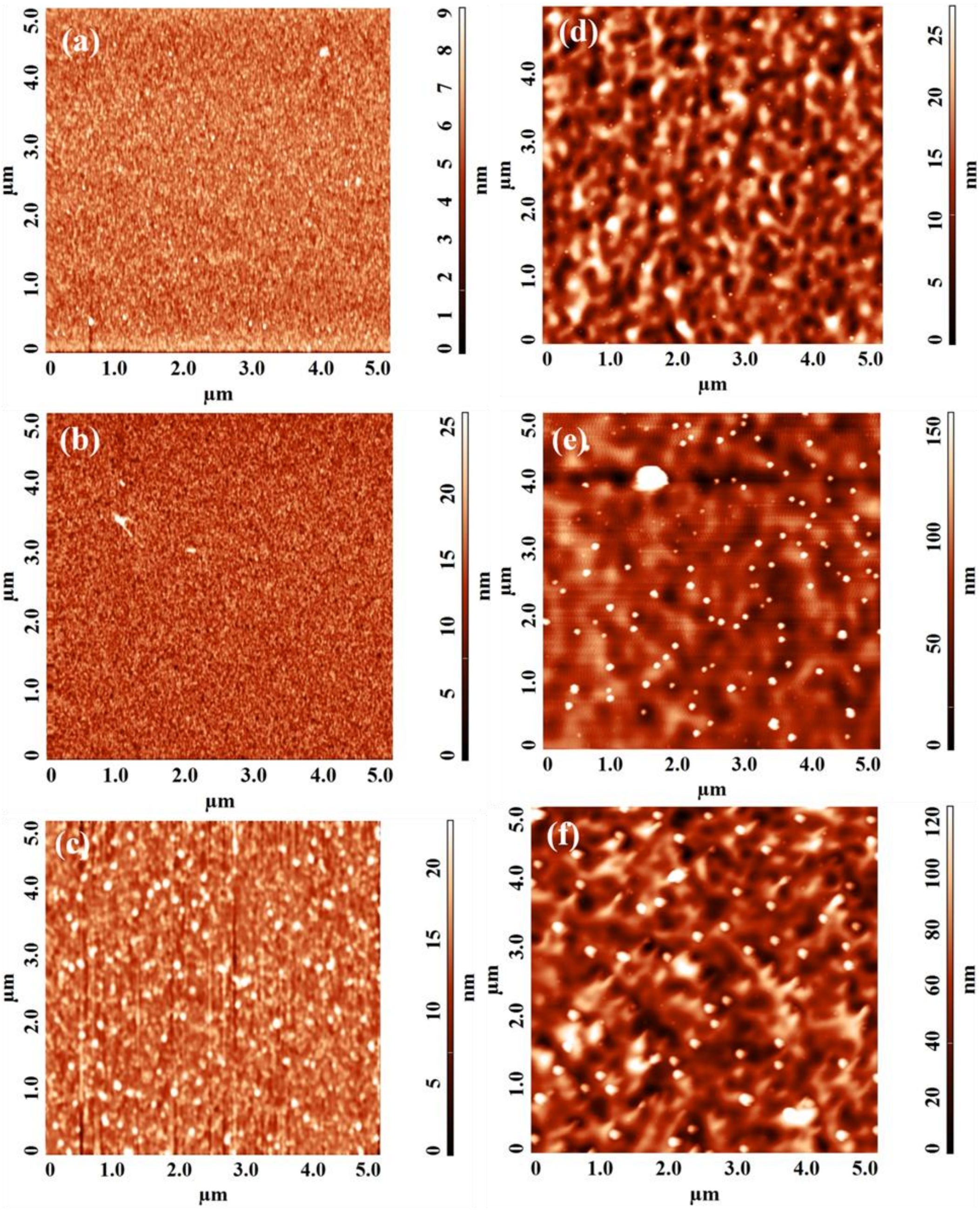

Fig. 5.4 *AFM micrographs of the as-deposited surfaces for (a) RT, (b) 500 ºC, (c) 800 ºC; and SIMS crater for (d) RT, (e) 500 ºC, (f) 800 ºC.*

depth profiling are illustrated by the topographical AFM micrographs of representative as-deposited surfaces and their corresponding SIMS crater in Fig. 5.4.

5.3.5 Rutherford backscattering spectrometry

The composition and interfacial broadening characteristics of the samples were also studied by RBS analysis, as SIMS and RBS are often used as complementary techniques [19]. The RBS spectra for all the as-deposited samples exhibited fairly sharp interfaces. A representative RBS spectrum for sample deposited at 700 °C is shown in Fig. 5.5. The computer simulations of the experimentally observed backscattering spectra were performed using SIMNRA program code [20]. The RBS spectra for all the as-deposited films were fitted to a bilayer of Mo/Si with a very thin interfacial oxide layer of about ~ 1-2 nm. The sharp rise in the Si edge and steep fall in the trailing edge of Mo clearly indicates the absence of any significant diffusion across the interface.

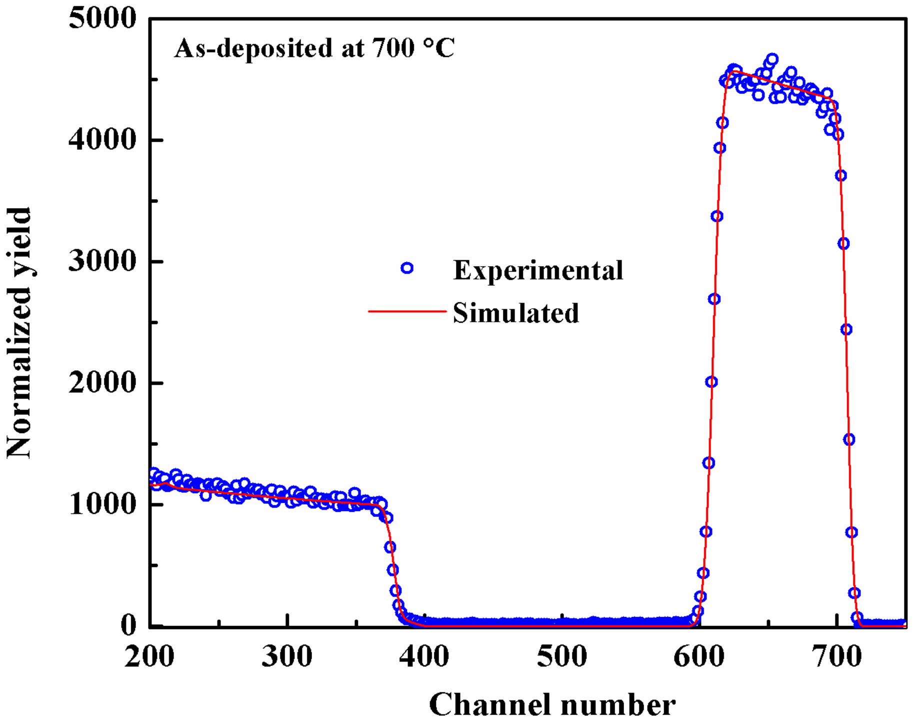

Fig. 5.5 *RBS spectrum for the Mo thin film as-deposited at 700 °C.*

5.4 Discussion

The interfacial broadening seen in the SIMS profiles of Fig. 5.3 resembles features which typically arises due to solid state inter-diffusion of Mo and Si across the interface. A T_s of 800 ºC is sufficiently high enough to initiate inter-diffusion of Mo and Si leading eventually to a solid state reaction which generally results in formation of silicides as reported in studies elsewhere [9]. However, the GIXRD patterns of the as-deposited films shown in Fig. 5.1 rules out the formation of any phase other than bcc - Mo. It is worth noting that a thermally activated diffusive phenomenon depends both on time as well as temperature. The fact that it didn’t occur even at a T_s as high as 800 ºC shows that, the diffusion process was either hindered by the short deposition time (which is also the equivalent annealing time in the present case) or by the existence of an underlying layer or impurity which acts as a diffusion barrier across the interface. The SIMS results in corroboration with the RBS results rules out the possibility of diffusion and supports the latter, that the interfacial oxide layer seen across the interface in the depth profile could possibly acts as a diffusion barrier [21]. In such cases, fitting the interface broadening in the profile to diffusion like equation would be erroneous. In addition, one can also notice that there is an asymmetry in the intensity profiles of Mo and Si shown in Fig. 5.3. In the absence of diffusion across the interface, the asymmetry is attributed to the difference in microstructure and sputtering characteristics between the polycrystalline Mo films and Si single crystal substrate. This is further substantiated by the fact that the asymmetry is observed even for samples prepared at RT.

The apparent broadenings upon SIMS depth profiling were then analyzed in the light of sample characteristics and the related processes operative during depth profiling. The broadenings in the profiles were quantified in terms of interface width

(IW) which is defined as the depth over which intensity of a particular species drops from 84% to 16% of its plateau value. The corresponding IWs for the observed interfacial broadening in the Mo depth profiles of Fig. 5.3 were estimated and are given in Table 2. Since depth profiling involves physical sputtering of the sample with energetic ions, SIMS depth profile analysis is inherently subjected to ion beam mixing of the samples by the impinging Cs^+ primary ions. The depth of this mixing is related to the penetration depth or the projected range R_p of the primary ions. The R_p of Cs^+ ions near and beyond the Mo/Si interface ranges from ~ 3 nm to 6 nm as calculated using TRIM code [22]. In SIMS depth profiles, the extent of ion beam mixing due to primary ion is described in terms of decay length, defined as the depth over which the

Table 5.2

Interface widths of the as-deposited and aged Mo films from SIMS depth profiles.

Substrate temperature (°C)	*Interface width of as-deposited films from Mo profiles (nm)*	*Interface width of aged films from Mo profiles (nm)*
RT	*16.92*	*18.29*
200	*20.5*	*23.17*
300	--	*23.75*
400	*23.5*	*24.43*
500	*32.31*	*33.5*
700	*27.68*	*29.98*
800	*37.10*	*37.1*

signal intensity drops by a decade (i.e., a factor of 10) [23]. The decay length of Mo into Si calculated from the depth profile of the RT as-deposited film was about ~ 7.3 nm/215 nm per decade, representing a fairly sharp interface. Herein, change in topography due to sputtering i.e., SIR normally degrades the depth resolution. The degradation results from two contributions, a small fundamental part and a larger contribution attributed to sample characteristics. The fundamental broadening (about ~ 1 nm) stems from the statistical nature of the sputtering process. This broadening follows a Poisson distribution [24] which further gets complicated if the initial surface is rough due to subsequent shadowing and re-deposition process. Note that the original surfaces of the as-deposited films in the present study were fairly smooth as measured by AFM. The RT as-deposited film has an *rms* roughness value of ~ 0.3 nm and an observed decay length which is roughly a factor 1.5 of the R_p. Hence, the finite broadening in the Mo profile across the interface for RT as-deposited film can be primarily attributed to the Cs^+ primary ion beam mixing [24] with some small contribution arising from SIR and sample characteristics. The contribution due to ion beam mixing largely remains constant while the broadening observed in samples deposited at higher substrate temperatures are accounted by the change in sample characteristics.

Further to delineate the subsequent effect of initial surface roughness on the resulting SIR, the surface topography of the same batch of samples were modified by oxidizing the top surface though prolonged exposure to ambient atmosphere. The inset in the SEM micrograph of film deposited at 800 °C shown in Fig. 5.2 illustrates the growth of this layer. The contrast visible near the top surface of the Mo film indicates the thickness of this amorphous oxide to be around 10 – 15 nm. SIMS depth profiles measurements were performed on all the exposed samples. A Representative

SIMS profile for the exposed 800 °C deposited Mo films superimposed on the SEM micrograph of the same film is shown in Fig. 5.6. The oxygen profile in the exposed film further substantiates the formation of the amorphous oxide layer. The growth of these amorphous oxides introduce considerable amount of surface roughness on the exposed films. The corresponding IWs estimated from the SIMS profiles for various exposed films are also tabulated in Table 5.2. The plot of the IWs before and after the oxidation upon subsequent SIMS depth profile measurements versus the corresponding T_s are shown in Fig. 5.7. A small increase in IW in the range ~ 2 to 2.5 nm is observed for the *RT, 200 ºC and 700 ºC* exposed films compared to the as-deposited ones. The rest of the exposed films result in IW values comparable to that of the as-deposited samples within values less than or close to 1 nm showing that the values of the IWs before and after the exposure are almost comparable. Moreover, there was no systematic correlation between the change and increase in IW with the amount of roughness introduced through surface oxidations. For some films, the introduced roughnesses were found to be quite large to be meaningfully measured by AFM. Probably, the depth resolution doesn’t deteriorate because the primary ion beam sputters the amorphous surface oxide uniformly which is further aided by the smoothing effect of surface diffusion [25]. However, the subsequent degradation in the depth resolution after the oxide layer has been sputtered away is decided by the microstructure of the metal film which constitutes the larger part of contribution to the SIR discussed above. From these observations, we infer that initial surface roughness due to an amorphous oxide layer on Mo doesn’t have a significant influence on the resulting IW. Also included in Fig. 5.7 are the plot of the average crystallite size estimated from XRD and the *rms* roughness of SIMS crater determined from AFM for comparison. The IWs estimated from SIMS depth profile analysis shows weak correlation with the crystallite sizes estimated from the XRD analysis.

The evolution of SIR can be studied by a systematic sputter depth profiling with SIMS and subsequent topographical mapping of the SIMS crater at different depth by AFM. This was performed for selected representative samples. Various topographic images of the SIMS carter acquired on RT and 400 °C deposited films at different depth are shown in Fig. 5.8 and Fig. 5.9, respectively. The evolving trend reveals that on sputtering first few layers of the amorphous oxide, the original surface roughness (*rms* value ~ 4.7 nm for specimen deposited at 400 °C) introduced due to aging shows some smoothening. Subsequently, the SIR and the resulting degradation in depth resolution are determined by the micro-structural characteristics of the poly-

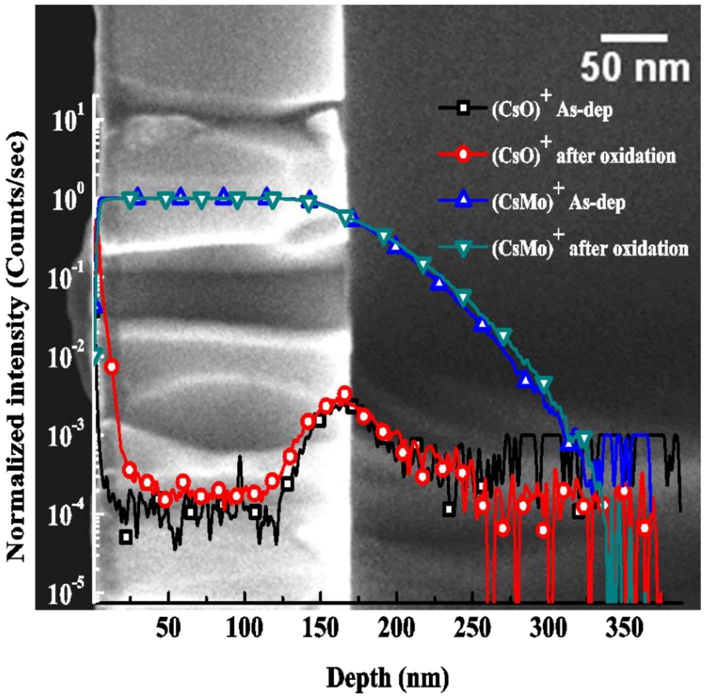

Fig. 5.6 *SIMS depth profiles of O and Mo in Mo films deposited at 800 °C before and after oxidizing exposure to ambient, superimposed on the cross sectional SEM micrograph.*

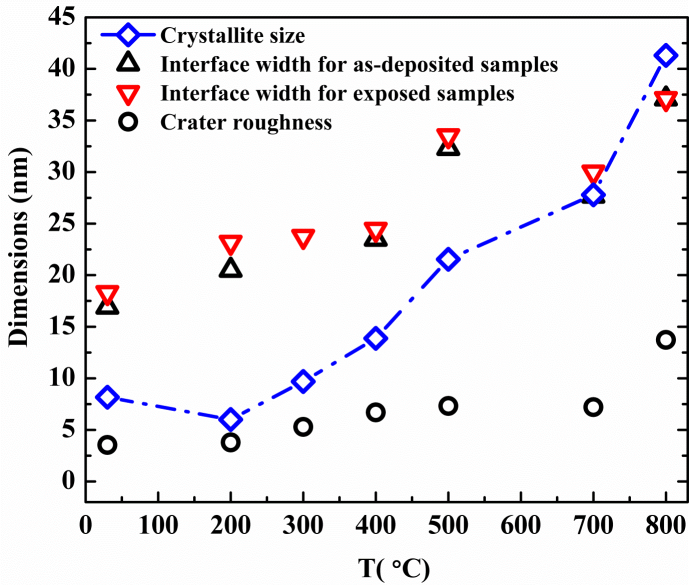

Fig. 5.7 *Crystallite size determined from XRD, interface width determined from SIMS and rms roughness of SIMS crater determined from AFM versus growth temperature* T_s.

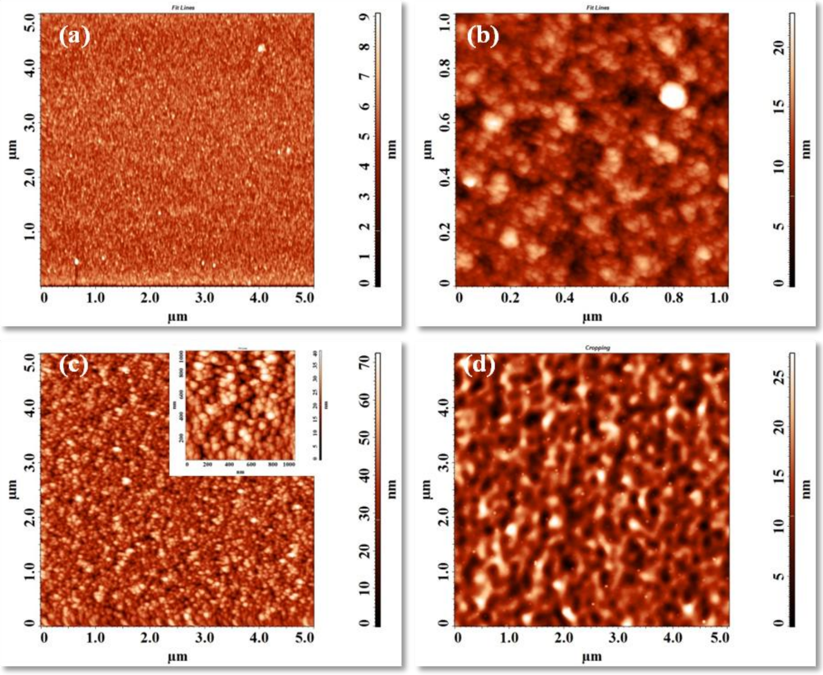

Fig. 5.8 *AFM micrographs for RT deposited film: (a) As-deposited surface (b) oxidized surface (c) SIMS crater near interface (inset shows 1x1* μm^2 *scan) and (d) SIMS crater in the Si substrate beyond the interface.*

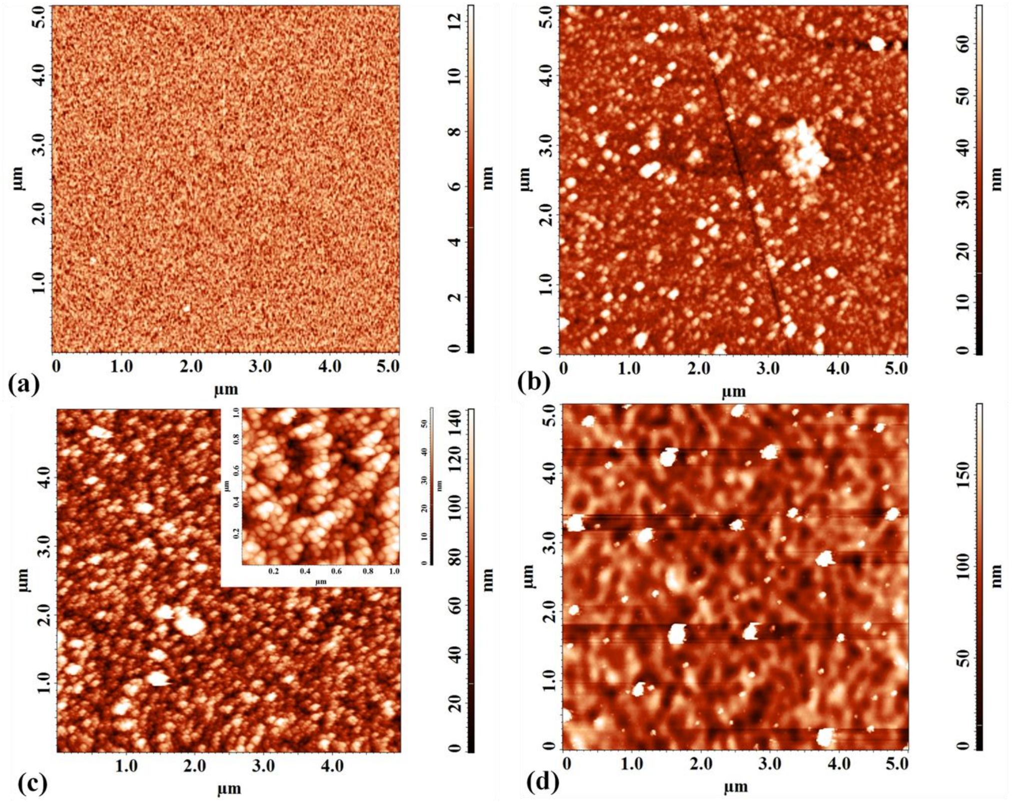

Fig. 5.9 *AFM micrographs for 400 °C deposited film: (a) As-deposited surface (b) oxidized surface (c) SIMS crater near interface (inset shows 1x1 µm^2 scan) and (d) SIMS crater in the Si substrate beyond the interface.*

-crystalline samples once the oxide layer is sputtered away. The SIR increases with depth and attains a maximum near the interface (*rms* value ~ 10.4 nm for specimen deposited at 400 °C). After the interface, a slight smoothening effect takes place due to uniform sputtering of Si (111) single crystal bringing the *rms* roughness value to ~ 6.7 nm.

The plot of *rms* roughnesses of the craters versus T_s is also shown in Fig. 5.7 and it correlates well with the observed IWs. As mentioned earlier, roughness on the SIMS crater or SIR results from topographic features introduced by preferential sputtering of differently oriented crystalline grains. Herein, it is important to notice that the *rms* roughnesses of the SIMS crater bottoms are obtained by direct measurement with AFM. The IWs on the other hand are estimated from the broadening in the falling edge of the elemental depth profiles, and also contain some inherent contribution from primary ion beam mixing. Hence one can notice the qualitative correlation in these two parameters but for some variation in their quantitative values.

While the interface broadening or the degradation in the depth resolution is characterized in terms of interface widths, XRD analysis provides a global estimate of the crystallite size of various as-deposited films. The weak correlation between the crystallite size and the interface broadenings hints that rather than the crystallite size, microstructure plays an important role in the resulting interface width. On the contrary, reasonable correlations can be seen between the observed interface width of the SIMS profile and the columnar micro-structural evolution seen in the SEM micrographs of Fig 5.2. Hence, it is established that SIR results from non uniform sputtering of different crystallographic orientations in a polycrystalline materials. This observation is true in case of polycrystalline metals which always tend to degrade the depth resolution. The morphological and micro-structural aspect of a metal film contributes significantly to interfacial broadening

5.5 Conclusion

Mo thin films with different micro-structural attributes were synthesized by controlling the substrate temperatures during RF sputter deposition. The effects of different micro-structures on the interfacial characterization of Mo/Si (metal/silicon) bilayers using SIMS and the related artifacts were evaluated with improved depth resolution. The diffusion-like signatures at the interfaces were attributed to the microstructures of the polycrystalline Mo films and the non uniform sputtering therein, as confirmed by AFM. Complementary techniques like RBS and XRD were effectively utilized to rule out the effect of diffusion. In addition, it is established that the original surface roughness of amorphous oxide layer on Mo films does not have significant influence on interface broadening.

References

---

1. S. Hofmann, *Rep. Prog. Phys.* 1998 ; *61,* 827.
2. A. Benninghoven, F. G. Rüdenauer, H. W. Werner, *Secondary Ion Mass Spectrometry: Basic Concepts, Instrumental Aspects, Applications and Trends*, John Wiley, New York, 1987.
3. H. W. Werner, R. P. H. Garten, *Rep. Prog. Phys.* 1984; *47,* 221-344.
4. A. Zalar, S. Hofmann, *Nucl. Instrum. Methods Phys. Res. B* 1987b; *18,* 655-658.
5. A. Zalar, S. Hofmann, *Vacuum* 1987; *37,* 169-173.
6. Z. L. Liau, B. Y. Tsaur, J. W. Mayer, *J. Vac. Sci. Technol.* 1979; *16*, 121.
7. Y. Gao, Y. Marie, F. Saldi, H. N. Migeon, *International Journal of mass Spectrometry and ion Process* 1995; *143,* 11 – 18.
8. N. Q. Lam, *Surf. Interface Anal.* 1988; *12,* 65.
9. F. Nava, G. Majni, P. Cantoni, G. Pignatel, G. Ferla, P. Cappelletti, F. Mori, *Thin Solid Films* 1982*; 94,* 59-65.
10. B. D. Cullity, *Elements of X-Ray Diffraction*, Addison-Wesley, Massachusetts, 1956.
11. T. P. Drüsedau, F. Klabunde, P. Veit, Th. Hempel, *phys. stat. sol. (a)* 1997; *161,* 167.
12. B. A. Movchan and A.V. Demchishin, Phys. Met. Metallogr. 28 (1969) 83.
13. J.A. Thornton, *Annu. Rev. Mater. Sci*. 1977; *7,* 239.
14. P.B. Barna, M. Adamik, *Thin Solid Films* 1998; *317,* 27–33.
15. S. Mahieu, P. Ghekiere, D. Depla, R. De Gryse, *Thin Solid Films* 2006; *515,* 1229 –1249.
16. S. Hofmann, A. Zalar, *Thin Solid Films* 1979; *60*, 201-211
17. Kiyohisa Fujinaga, Izumi Kawashima, *J. Vac. Sci. Technol. A* 1988; *6,* 213.

18. H.Yildirim Erbil, *Surface Chemistry of Solid and Liquid Interfaces*, John Wiley & Sons, UK, 2006.
19. D. J. O’Connor, B. A. Sexton and R. St. C. Smart, *Surface Analyis Methods in Materials Science*, Springer, Germany, 2003
20. M. Mayer, SIMNRA user's guide. Tech. Rep. IPP 9/113, Max-Planck-Institut für Plasmaphysik, Garching, 1997.
21. A.H. van Ommen, R.A.M. Wolters, *J. Appl. Phys.* 1985; *58,* 4043.
22. TRIM calculation, http://www.srim.org/
23. R.G. Wilson, F.A. Stevie, C.W. Magee, *Secondary Ion Mass Spectrometry: A Practical Handbook for Depth Profiling and Bulk Impurity Analysis*, Wiley, New York, 1989.
24. M.P. Seah, C. Lea, *Thin Solid Films* 1981; *81,* 257- 270
25. J. Erlewein, S. Hofmann, *Thin Solid Films* 1980; *69,* L39.

CHAPTER 6

SUMMARY AND SCOPE FOR FUTURE WORK

6.1 SUMMARY

Advances in surface and interface science have played an important role in the development of advanced materials technology including that of thin films. Polycrystalline Mo/Si thin film system has wide ranging technological applications wherein diverse interfacial characteristics and their underlying chemistries needs to be established carefully. This thesis presents result of investigations performed on various aspects of poly-Mo/Si thin film with an aim to gain some insight on its structural, phase and interfacial characteristics. Ion beam mixing, particularly with inert ions like Ar^+, has been successfully exploited for silicidation in several metal/Si systems as an alternative to the conventional solid state reaction that often faces reproducibility issues. The interface mixing and phase formation characteristics in Mo/Si system by Ar^+ ion beam irradiation and flash annealing were explored as this issue is neither clearly investigated nor fully understood. Further, as thin films inevitably endure various operating environment, stored residual stress can sometime cause deleterious de-lamination of the thin film system. Understanding the origin and control of the amount of residual stress in deposited thin films is crucial for any technical application. Hence, the evolution of residual stress in poly-Mo/Si thin film deposited at different temperatures was explored by X-ray diffraction technique. Finally, issues pertaining to the analysis of chemical composition of polycrystalline thin film structures and interfaces with SIMS are investigated. The associated distortion and artifacts in the SIMS depth profiles were demonstrated using controlled Mo/Si specimens. The investigations presented in this thesis use corroboration of results obtained from several surface and interface analytical techniques which include SIMS, GIXRD, RBS, AFM, FESEM and Raman spectroscopy. A brief summary that sums up the essence and findings of each topic is outlined below.

The phase formation of $MoSi_2$ upon interface mixing across Mo/Si bilayer thin films by Ar^+ ion beam irradiation and subsequent flash annealing was investigated. The Ar^+ ion energy and thickness of Mo films used in the study were predetermined for efficient mixing across the interface based on TRIM calculation. Irradiations were carried out at doses ranging from 7×10^{15} cm^{-2} to 2×10^{17} cm^{-2}. Investigation of mixing and phase characteristics with SIMS and GIXRD shows that only substantial mixing and inter-diffusion result upon irradiation. Formation of disilicide phase occurs only upon flash annealing of the irradiated specimen at 800 °C for a duration of 60 seconds. However, results from GIXRD and Raman show that the nucleated phases consist of a dose dependent polymorphic disilicide phases. Only meta-stable *h*-$MoSi_2$ was found to nucleate for specimens irradiated to low doses. Whereas both *h*-$MoSi_2$ and thermodynamically stable *h*-$MoSi_2$ nucleate for specimens irradiated to high doses. The phase retardation indicated by the persistence of the meta-stable *h*-$MoSi_2$ phase even after high temperature annealing was attributed to Ar impurities entrained in the films. Post annealing composition from SIMS and RBS reveal formation a graded disilicide phase.

Further a brief investigation on the local homogeneity of Ar^+ ion beam mixed Mo/Si thin film performed using secondary ion imaging technique with SIMS is outlined. The investigation was performed on the specimen irradiated to an ion dose of 2 x 10^{17} ions/cm^2. Series of image planes were acquired and different regions of interest were selected. Offline depth profiles for these regions were constructed and decay length calculated for each region. Significant local variation in decay lengths were observed for different local region of interest suggesting in-homogeneity in the ion beam mixed zone.

The evolution of residual stress in Mo thin films deposited on Si substrate as a function of substrate temperature was investigated. The analysis was primarily based on use of X-ray diffraction to find the stress. In doing so, two approaches were employed, both using the asymmetric grazing incidence parallel beam geometry. While one method involved the peak shifts analysis of a single *hkl* reflection, the other one combined peak shifts analysis from multiple *hkl* reflections. These two approaches resulted in almost comparable values, but the multi *hkl* approach is advantageous in cases where anisotropy is introduced either by grain interaction or texturing. Films deposited at lower substrate temperature exhibited high compressive stress to the extent that films deposited at room temperature shows blister buckling delamination through formation of telephone cord like structures. The compressive stress relaxes slowly as the substrate temperature is increased and it finally reverses to comparatively low tensile stress. This evolution was explained as a consequence of competition between intrinsic and thermal components of stress. The values of the thermal stress expected to be generated in Mo films deposited on Si at various substrate temperature were calculated and compared with the experimental findings. A good agreement over high temperature range suggested that the high tensile stress is primarily an outcome of the thermal mismatch between Mo and Si, and expected in general as Mo has a higher average thermal expansion co-efficient than Si at any given temperature. However, the dominance of intrinsic stress led to deviation of the observed stress from the calculated values at low substrate temperature. While compressive stresses in sputtered films are generally attributed to atomic peening from reflected neutral Ar atoms, insight that suggests oxygen impurities as the cause of compressive stress were obtained from the analysis of SIMS data. SIMS depth profiles show negligible Ar content in the film but significant oxygen impurities in films deposited at low temperature. Crystalline fibrous features that result from reduction in grain mobility due to oxygen impurities were seen in the morphology of the films deposited at lower substrate temperature.

Finally, the effect of microstructures of Mo thin films on the interfacial characterization of Mo/Si system with SIMS depth profiling was investigated. While Mo/Si was presented as a case study, the study gains importance because of the ambiguous artifacts that is often associated with SIMS depth profile analysis of polycrystalline material interfaces. Mo/Si thin films with varying Mo microstructures were deposited on Si and characterized. Compositional analysis with SIMS depth profiling of these films shows a systematic broadening in the interface profiles of Mo as a function of deposition temperature. These broadenings in the Mo profiles at the interfaces were investigated. The aspects of interfacial phase formation and diffusion were investigated with GIXRD and RBS and eventually ruled out. The broadening was then characterized in the light of sample characteristics and the process operative therein during sputter depth profiling. The estimated interface width in the profile was correlated to the sputter induced roughness (SIR) resulting from non uniform sputtering of differently oriented polycrystalline grains. The roughness of the surfaces and SIMS craters were characterized by the *rms* roughness values of the respective topographies obtained by AFM. The evolution of SIR was studied by depth resolved

SIMS depth profiling and subsequent topographic mapping by AFM. The result shows that inside Mo films, SIR increase with depth and reaches a maximum near interface, after which it decrease due to uniform sputtering of single crystal Si. Additionally it was found that the introduction of original surface roughness on the Mo by the formation of amorphous oxide does not affect the interface broadening significantly.

6.2 SCOPE FOR FUTURE WORK

The RF magnetron sputtered Mo thin films deposited at low substrate temperature were found to have oxygen impurities as evident from the SIMS depth profiles. These oxygen impurities were correlated to the compressive stress observed in such films in chapter 4. Hence, it is worthwhile to deposit Mo thin films in ultra high vacuum (UHV) conditions like the one that prevails in UHV compatible electron beam evaporation system to minimize the oxygen impurities. Residual stresses in these films can be evaluated using X-ray diffraction. These values can be compared with the present values obtained for magnetron sputtered films. This investigation will discern the role of oxygen in the building up of compressive stress as observed in the present magnetron sputtered Mo thin films.

In the absence of diffusion, microstructures of the Mo films were found to influence the interfacial broadening in SIMS depth profiling of Mo/Si system. It is worthwhile to further study the effect of (grain boundary) diffusion characteristics across the interface using SIMS. This can be performed by forming a diffusion couple of a-Si/poly-Mo with varying Mo’s microstructure using UHV compatible electron beam evaporation system, followed by diffusion annealing and SIMS depth profiling.

APPENDIX: A

Study of local homogeneity in ion beam mixed zone using secondary ion imaging

Secondary ion imagining with SIMS can provide accurate elemental mapping of a specimen surface. Herein, the local homogeneity in the Ar^+ ion beam mixed zone of the Mo/Si bilayer thin film specimen irradiated to a fluence of 2 x 10^{17} cm^{-2} was investigated using secondary ion imaging. Series of direct ion images were acquired on the resistive anode encoder image detector of a CAMECA IMS 7f SIMS for the study. The energy, primary ion current, angle of incidence and impact energy of the primary beam (Cs^+) were 110 keV, 10 nA, 45 ° and 5 keV, respectively.

The image planes reveal heterogeneous concentration of Mo and Si. However, preferential accumulation of Mo could be observed in local regions of the image planes originating from Si layer as shown in Fig. A (i). Streaks of Mo species into the Si layer could be seen in the 3D composite view of the RAE image for Mo species shown in Fig. A (ii). In the present study, the range of the Ar^+ ion used for mixing far exceeds the range of inherent primary Cs^+ ion beam mixing artifacts and hence the latter can be ignored. Under such assumption, the decay length λ in essence indicates the extent of ion beam mixing and the homogeneity of the ion beam mixed zone can be investigated by calculating λs of Mo for different local Region of Interest (RoI) in the image plane. The decay length is defined as the depth over which the secondary ion intensity drops by a factor of 10 and is expressed as [1-2].

$$\lambda = \frac{x_1 - x_2}{\ln{(I_2/I_1)}}$$

where x_1 and x_2 are the depth at which the ion intensities are I_1 and I_2 respectively.

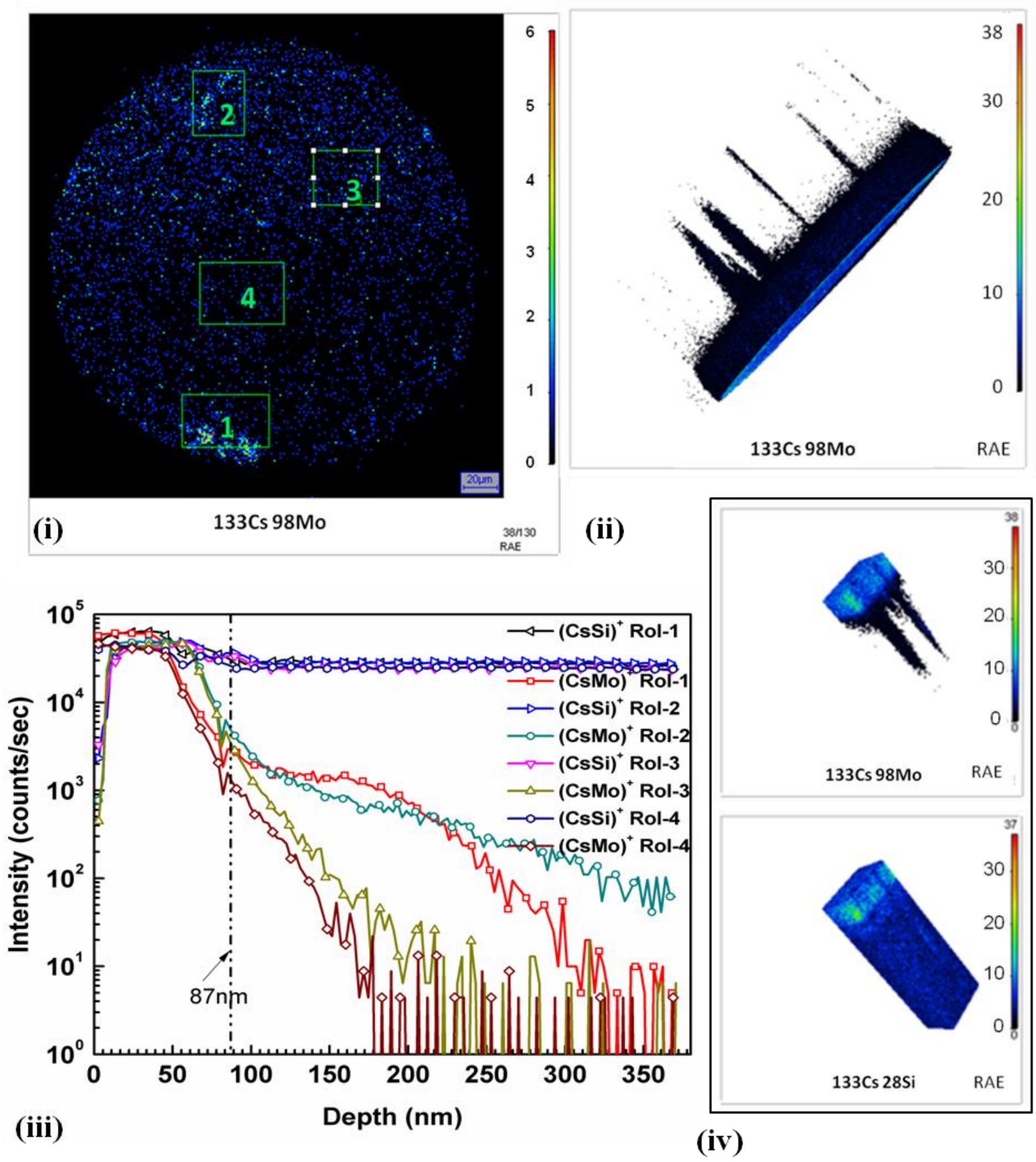

***Fig. A:* *(i)* RAE image frame showing different Region of Interest (RoI) in Si substrate at a depth of 87 nm *(ii)* 3D composite view of the RAE image for Mo species sample as $(CsMo)^+$ complex *(iii)* SIMS depth profiles constructed from the different Region of Interests *(iv)* Cropped 3D composite view of Mo and Si species for the region of interest- 1 (RoI-1).*

Fig. A (iii) shows the offline depth profiles constructed for each RoIs defined in Fig. A (i) from the segmented image planes using the application software WinImage from CAMECA [3]. The corresponding λs calculated for each RoI are given in Table A.

Table A: Decay length for different Region of Interests (RoIs)

Region of Interest (RoI)	Decay length (nm)
RoI-2	*82.12*
RoI-3	*21.3*
RoI-4	*19.25*

The result shows a significant local variation in the decay length (λ). RoI-1does not exhibit a proper exponential decay; hence decay length for RoI-1 is not calculated. The significant diffusion observed in RoI-1 can owe its attribute to radiation enhanced diffusion. The cropped 3D composite view for Mo and Si species in the RoI-1 is shown in Fig. A (iv) for clarity. The variation in the decay lengths shows that the ion beam mixed zone is not homogenous but preferential accumulation takes place over certain regions. The local in-homogeneity in the ion beam mixed zone is demonstrated using SIMS image analysis.

References

---

1. E. Lidzbarski and J.D. Brown, *Secondary Ion Mass Spectrometry, SIMS V*, Springer, Berlin (1985) 306.

2. R.G. Wilson, F.A. Stevie and C. W. Magee, *Secondary Ion Mass Spectrometry: A Practical Handbook for Depth Profiling and Bulk Imputiry Analysis*, Wiley, New York, 1989.

3. WinImage CAMECA SIMS Image Processing Software.